School of Civil and Mechanical Engineering

Investigation of the Evaporation Process of a Freely Falling Droplet in Turbulent Channel Flow

Elham Mohammadi

This thesis is presented for the Degree of

Doctor of Philosophy

of

Curtin University

January 2020

Declaration

To the best of my knowledge and belief this thesis contains no material previously published by any other person except where due acknowledgment has been made. This thesis contains no material which has been accepted for the award of any other degree or diploma in any university.

Signature: .....

Date: .....

Acknowledgement

The work presented in this thesis has been carried out at Department of Mechanical Engineering at Curtin University. I gratefully acknowledge the Australian Postgraduate Awards (APA) and Curtin University Postgraduate Scholarship (CUPS) provided by Curtin University for making this Ph.D. possible.

First and foremost, I would like to express my sincerest gratitude to my supervisors Dr. Ramesh Narayanaswamy and Dr. Andrew King for their continuous support, guidance, and encouragement through this work. Their valuable input are gratefully acknowledged.

I would like to thank the technical staff in the laboratory of Mechanical Engineering department, in particular, David Collier and Graeme Watson who have been very helpful whenever I had any difficulty. I sincerely acknowledge their support.

Special thanks to Technical Support Manager at Photron USA, Inc., Karl Wiencek, for his support and co-operation.

I would like to thank my strong woman who always lifts me up and continues to make me proud, Dr. Ferial Hakami.

I would like to dedicate this thesis to folks who raised me, Ensiyeh and Ahmad, the love of my life, Alireza, and my most precious peas, Sepehr and Kian who are my reasons for being.

ABSTRACT

Evaporation of sprays happen in natural and industrial applications such as rain drops, power generation and process engineering. Efficient evaporation process is a key in spray combustion and cooling applications. The present work serves to understand complicated mechanisms associated with the dilute region of spray by considering evaporation of a single droplet freely falling in a channel. As in most of industrial applications the spray takes place in turbulent flow field, the effect of turbulent structure on the evaporation is investigated. This study attempts to increase the understanding about the effect of turbulence on the evaporation of a droplet and seek to answer if the higher turbulent flow brings more evaporation, better mixing and more efficient spray process.

To this end, an open source CFD code has been developed in OpenFOAM, capable of simulating three phases of liquid, vapour and gas media, separately as well as heat and mass transfer. Considering vapour as a separate phase instead of assuming the media around the droplet is a mixture of the gas and the vapour, enables studying the interaction between the vapour and turbulent structure and the mixing of vapour with gas. It is also possible to find any turbulence modulation by vapour. The code is based on the Volume of Fluid (VOF) method that is a mass conservative method. But it is not generally volume conservative. Due to the phase change process during the evaporation, an extra volume is created that must be accommodated otherwise the simulation will not represent the process

correctly. Therefore, an innovative method is applied in the code for this purpose to provide correct interface jump condition by considering different velocities for each phase at the interface.

A channel geometry is used for the numerical simulation. Fully turbulent flow field is achieved by using cyclic boundary conditions in lateral walls as well as inlet and outlet of the channel. In addition, correct pressure gradient is set as an external force in the momentum equation to provide the desired bulk mean velocity inside the channel. Large Eddy Simulation (LES) is used for turbulent simulation. Appropriate time step is considered to avoid spurious currents on liquid-vapour interface.

To validate results of the numerical study, detailed set of experiments are carried out in a laboratory. A channel is designed to be long enough to maintain fully turbulent flow. The developed region of the channel is made of polycarbonate to facilitate image capturing. Droplets are released in the test section falling freely in turbulent flow and images are captured by a high speed camera. The numerical results for a water droplet in a fully developed channel flow represented by dimensionless droplet diameter history are in good agreement with the experimental data. Another validation that is performed using empirical correlations in terms of Sherwood number, suggests that the numerical model has reasonable accuracy and is capable of simulating the evaporation of the droplet in turbulent channel flow.

Then the study attempts to investigate the effect of turbulent Reynolds number on the evaporation of a single droplet in channel flow by means of the developed code. The approach involves considering two different turbulent Reynolds numbers as well a simulation in laminar flow and a simulation in stand still air. The results show that turbulent flow has significant effect on the evaporation by increasing the evaporation rate comparing to the laminar flow and stand still air. But the

higher turbulent Reynolds number does not necessary provide higher evaporation rate.

To seek the reason for this discrepancy, the unsteady flow around the droplet by considering Q-criterion as well as the vorticity field are studied. Besides, turbulent energy dissipation rate of turbulent cases are compared to have better understanding about the vortical structure around the droplet. It is shown that the dissipation rate has strong effect on the evaporation and does not depend on the turbulent Reynolds number in channel flow. Comparing two turbulent cases, in higher turbulent Reynolds number, due to higher conventional flow, vortex stretching is stronger that makes the vapour boundary layer thinner. As a result, less mixing of vapour with ambient flow takes place in higher turbulent Reynolds number. The effect of vapour on turbulence modulation is also studied and shown that the droplet is able to mix with vortical structure and reform turbulence. For more investigation, temperature field is considered in different flow fields and shown that laminar flow and stand still air provide smaller cooling area. In non turbulent flows, the generated vapour layer around the droplet acts like a blanket, due to the lack of strong conventional flow, and resists heat transfer to the ambient. So the temperature inside the droplet increases but there is not significant heat transfer to the ambient. On the other side, strong heat transfer between the droplet and ambient happens in turbulent flow makes larger cooling affected area in a short time.

Publications arising from this work

Peer reviewed conference proceedings

E. Mohammadi, A. King and R. Narayanaswamy, “A Study on the Flow Field and Internal Circulation of a Single Moving Droplet", 20th Australasian Fluid Mechanics Conference, Perth, Australia, 5-8 December 2016.

E. Mohammadi, R. Narayanaswamy and A. King, “A Study of the Phase Change in Three Phase Environment", 21st Australasian Fluid Mechanics Conference, Adelaide, Australia, 10-13 December 2018.

Journal paper

E. Mohammadi, R. Narayanaswamy and A. King, journal paper “Three Phase Modelling of Evaporation and Heat Transfer of Droplet in Turbulent Channel Flow", is currently being prepared.

Awards

Australian Postgraduate Award (APA) and Curtin University Postgraduate Scholarship (CUPS) 2015.

Thesis Completion Scholarship, 2019.

Table of Contents

List of Tables

List of Figures

Nomenclature

Acronyms

CD Central Differencing

CFD Computational Fluid Dynamics

CFL Courant-Friedrich-Lewy condition

CSF Continuum Surface Force

DNS Direct Numerical Simulation

FDM Finite Difference Method

FEM Finite Element Method

FVM Finite Volume Method

LES Large Eddy Simulation

MDF Medium-Density Fibreboard

PIMPLE combination of PISO and SIMPLE

PISO Pressure-Implicit Method for Splitting of Operators

r.m.s root-mean-square

RANS Reynolds Averaged Navier-Stokes

SIMPLE Semi-Implicit Method for Pressure-Linked Equations

TVD Total Variation Diminishing

UD Upwind Differencing

VOF Volume Of Fluid

Greek Symbols

Δ	grid spacing	m
η	the smallest turbulent eddy size	m
κ	mean interface curvature	$1/\mathrm{m}$
μ	dynamic viscosity	$\mathrm{kg}/[\mathrm{ms}]$
Ω	skew-symmetric rate-of-rotation-tensor	$1/\mathrm{s}$
σ	surface tension coefficient	N/m

Roman Symbols

$\dot{m}''$	mass transfer flux	$\mathrm{kg}/[\mathrm{m}^2\mathrm{s}]$
$\dot{q}_s$	energy rate transfer across the surface of the control volume per unit mass	$\mathrm{J}/[\mathrm{m}^3\mathrm{s}]$
$\dot{q}_v$	rate of heat source or sink across the surface area of the control volume per unit mass	$\mathrm{J}/[\mathrm{m}^2\mathrm{s}]$
$\hat{h}$	enthalpy	$\mathrm{m}^2/\mathrm{s}^2$

$\hat{M}$	molar weight	kg/mol
$\hat{u}$	internal energy	m^2/s^2
B_M	Spalding mass transfer number	dimensionless
$C_{\Delta x}$	capillary flow velocity	m/s
$C_{\text{Frö}}$	Frössling coefficient	dimensionless
c_j	concentration of component j	$1/m^3$
C_p	specific heat in constant pressure	$J/[kgK]$
C_T	turbulent coefficient	dimensionless
Co	Courant number	dimensionless
d	droplet diameter	m
Da	Damköhler number	dimensionless
e	total energy per unit mass	J/kg
F	force	N
f_b	body force	N/m^3
h	convective heat transfer coefficient	$W/[m^2K]$
h	height	m
h_m	convective mass transfer coefficient	m/s
I	turbulent intensity	dimensionless
K	evaporation rate	m^2/s

k	thermal conductivity	$W/[mK]$
L	development length of the channel	m
l	largest turbulent length scale	m
N	length of the diffuser	m
n_Σ	interface normal vector	dimensionless
N_j	molar flux of component j	$1/[m^2 s]$
Nu	Nusselt number	dimensionless
Oh	Ohnesorge number	dimensionless
Pr	Prandtl number	dimensionless
Q	Q-criterion	$1/s^2$
q	turbulent kinetic energy	m^2/s^2
R_0	vapour thickness in film theory	m
Re	Reynolds number	dimensionless
Re_{mean}	Re based on mean velocity	dimensionless
S	symmetric rate-of-strain-tensor	$1/s$
Sc	Schmidt number	dimensionless
Sh	Sherwood number	dimensionless
T	temperature	K
t_η	time scale of the smallest turbulent eddy size	s

U	mean velocity	m/s
u	volume averaged velocity or velocity in x direction	m/s
u'	fluctuating velocity	m/s
u_τ	friction velocity	m/s
V	volume	m^3
v_{diff}	atomic diffusion volume	m^3/mol
V_r	blowing velocity in film theory	m/s
W	width	m
w	vorticity	1/s
We	Weber number	dimensionless
x	position	m
Y_v	vapour species mass fraction	dimensionless

Subscripts

$(.)_0$	initial value
$(.)_\sigma$	related to surface tension
$(.)_{\text{Frö}}$	Frössling
$(.)_{amb}$	ambient
$(.)_a$	air
$(.)_c$	continuous phase

$(.)_{di}$ diameter

$(.)_{d}$ disperse phase

$(.)_{evap}$ evaporation

$(.)_{f}$ face

$(.)_{hyd}$ hydraulic

$(.)_{h}$ minor axis length

$(.)_{int}$ interface

$(.)_{rel}$ relative

$(.)_{rgh}$ mean interface curvature

$(.)_{turb}$ turbulent

$(.)_{UD}$ upwind differencing

$(.)_{vct}$ turbulent convective vaporization

$(.)_{vs}$ quiescent environment

$(.)_{w}$ wall

Superscripts

$(.)^{+}$ wall unit

$(.)^{0}$ value at the previous time step

$(.)'$ fluctuating quantities

$(.)^{n}$ value at the current time step

$(.)^{t}$ value at time t

Chapter 1

INTRODUCTION

1.1 Introduction

In this chapter a brief review of the important phenomena related to droplets in a spray or as a single droplet in a dilute spray is discussed. Different regions of a spray are outlined and non-dimensionalized numbers used in this thesis are explained.

1.2 Physical Phenomena

Evaporation happens in many phenomena from micro-droplets of fuel in engines to water evaporation on the surface of oceans. The paramount importance of this phenomena is more pronounced with the inclusion of spray evaporation. In many industrial applications, liquid spray is used to increase heat transfer. These applications include fuel spray in liquid rocket engines and diesel engines, cooling spray in gas turbine blades, inlet air fogging system for gas power plants, and drying in food industry. Although, in many of these applications the spray encounters turbulent flow, there are still gaps in fully understanding the spray behaviour in turbulent

flow. Experimental method of research though provides accurate measurement of the flow, the precise measurement of all variables at every point in the three dimensional domain is not possible due to inherent limitations in experiments. However, owing to the complex structure of the turbulent flow alongside with the evaporation process, the recognition of the detailed phenomena and physics with a single point evaluation is not adequate. Therefore, numerical study is a helpful tool for interpretation of the processes involved in this intricate problem. To have a better insight into the spray evaporation problem, a detailed description of this phenomena is given in the following paragraphs.

A spray is a two-phase flow. In fact, the liquid of the spray and the ambient gas are the first and the second phases of the flow. The liquid phase is also referred as the dispersed phase and the ambient gas as the continuous phase. When evaporation takes place, the presence of the third phase, vapour, makes it a three-phase flow.

One of the significant fluid dynamic phenomena occurring with sprays is the wake and boundary layer development due to the relative velocity between the drop centre and the ambient gas. The wake recirculation region behind the droplet appears as soon as the Reynolds number reaches a specified value where the streamline leaves the liquid surface. The dimensions of the wake area increases with Reynolds number. The boundary layer formed around the droplet augments the heat and mass transfer. Figure 1.1 shows streamlines and vorticity field around a droplet for different Reynolds numbers. The formation of the external boundary layer at the upstream region in all three cases can be seen from the vorticity filed contours.

Shear-driven internal circulation of the liquid inside the droplet is one of the features involving sprays. The shear forces steer the droplet to deform and move toward the flow direction, while the surface tension force resists the deformation

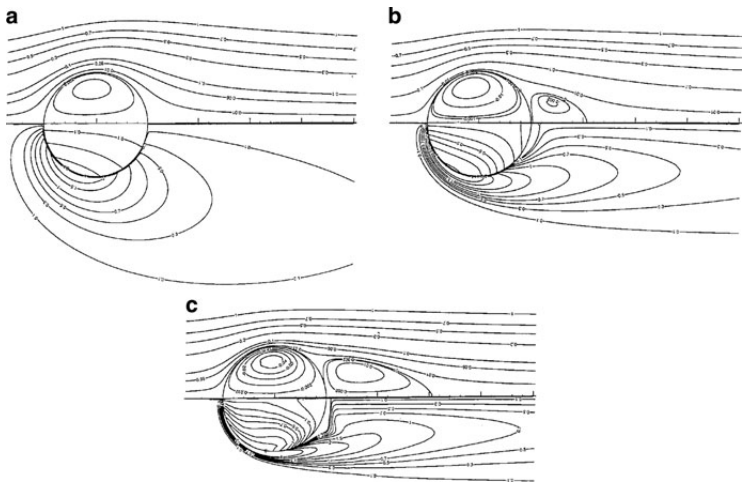

Figure 1.1: Streamlines (on the top half) and vorticity field (on the bottom half) of a droplet in different flow Reynolds numbers, (a) $Re = 10$, (b) $Re = 100$, (c) $Re = 500$ [1]

to retain the spherical shape of the droplet. As far as the Weber number is of the order of 1, the droplet remains spherical. Figure 1.2 shows streamlines and vortices inside a droplet. Viscous shear force at the interface is responsible for the internal circulation of liquid. The inner region of the drop contains the toroidal core which is identical to Hill's vortex and nearly shear free. The Reynolds number of Hill's vortex inside the droplet can be as high as or more than the Reynolds number of the gas phase around the drop due to the higher density of the liquid [2]. There are two boundary layers around the interface; the liquid boundary layer in the liquid side of the interface and the gas boundary layer on the outer side. Thinner boundary layer is expected for the liquid side due to the higher Reynolds number in liquid region. The internal wake region accommodates liquid viscous layer. The liquid circulates in this area out of liquid boundary layer.

A phenomenon of interest in droplet evaporation is the Stefan flow. During the evaporation process, the produced vapour from the surface of the liquid is moved away to the ambient gas as it is dispersed by additional produced vapour that is

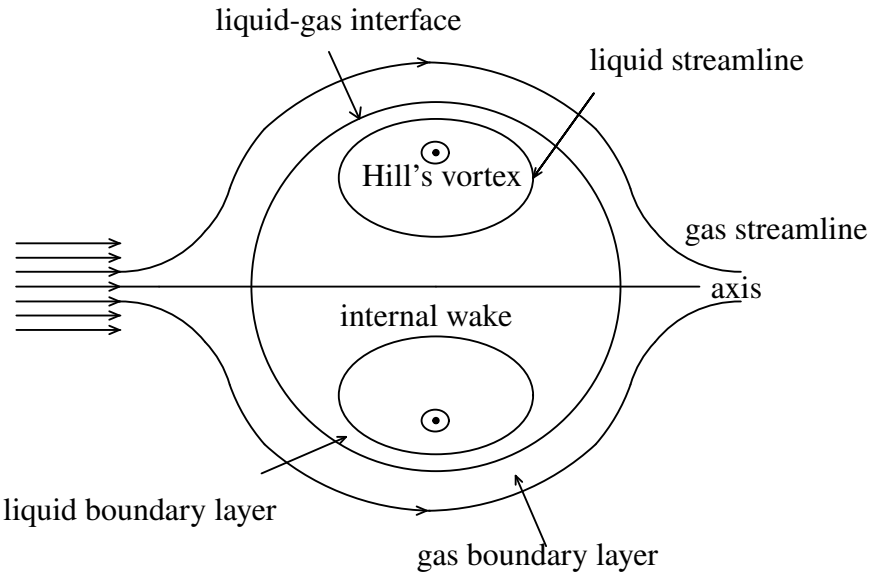

Figure 1.2: Streamlines and vortices inside a droplet [2]

called Stefan flow. Due to the higher vapour concentration near the interface, diffusion mechanism transports the generated vapour from the interface into the ambient. Due to the low concentration of ambient gas near the interface, it brings gas toward the drop which is called Fickian diffusion. The Fickian diffusion and Stefan flow works in the same direction near the interface and acts in opposite direction far from the droplet. The figure 1.3 shows these transport mechanisms near the droplet interface.

Surface tension is a force that tends to keep droplets in the most resistant form, i.e., spherical form. Any external force acting on the drop except surface tension tends to deform it. The force interactions work like a perturbation that leads to droplet oscillation. During atomisation process, wherever a droplet is detached from a bigger drop or when two drops collide, this phenomenon is observed.

Breakup is another phenomena that happens to droplets as they are released from jet flow. The primary breakup of spray happens when the first droplets detach from the main stream of spray. The secondary atomisation is the breakup of the

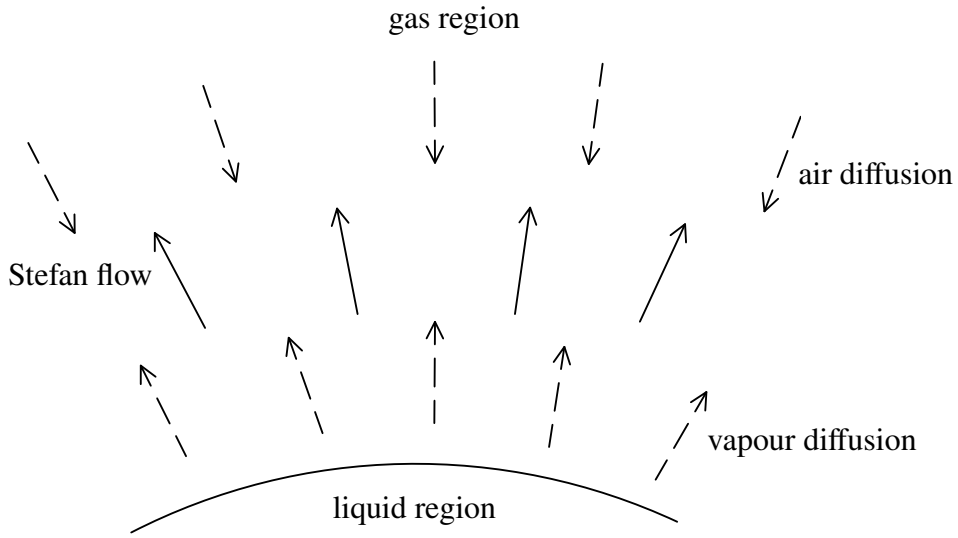

Figure 1.3: Stefan flow and diffusion near gas-liquid interface during evaporation [3]

first droplet into smaller ligaments which is referred to secondary atomisation. The phenomena of secondary breakup in real condition occurs in a turbulent flow field.

When aerodynamic forces are strong, droplets may experience breakup. The process of splitting up of a droplet into smaller fragments due to disruptive aerodynamic forces is called secondary atomisation [4]. This phenomena has an important role in the enhancement of mixing and heat and mass transfer due to sprays.

Breakup of a droplet is dependent on the disruptive aerodynamic force and the restorative surface tension force acting on the droplet. The ratio of these two forces is called Weber number.

The effect of droplet viscosity which is expressed as Ohnesorge number hinders deformation. Moreover, viscosity dissipates energy of the aerodynamic forces. However, it is found that for the cases with $Oh < 0.1$ the viscous forces are small enough that breakup is not affected by Oh number. Hence, the breakup is only dependent on Weber number [5].

As in most of the applications of secondary atomisation, the ambient fluid is air or small viscosity gases, the assumption of inviscid flow is mostly applied in this field.

Based on different values of Weber number different regimes of breakup for Newtonian droplets have been considered by Guildenbecher [5].

1.3 Spray Regions

In order to determine which part of the spray is considered in the work presented in this thesis, the following section categorises different parts of a spray. Figure 1.4 shows different zones of a spray.

The spray formation happens at the exit of the nozzle. The liquid coming out of the nozzle, called liquid core, extruding into the gas medium quickly makes turbulence, and breakup into droplets as it flows away from the nozzle. The droplets are rather big in the primary breakup compared to the secondary breakup. Inter-droplet collision is the principle mechanism for the droplet motion. The droplet-droplet collision can lead to coalesce resulting in a bigger droplet. This region is called the dense regime of the spray or near field region.

The primary droplets, then, undergo deformation and secondary breakup due to the aerodynamic forces acted upon them. This happens in the intermediate regime of the spray where inter-droplet collision is important but the effect of the ambient is the main factor for drop behaviour. The wake of one droplet will impact the drag and lift coefficient of the neighbour droplet. The number of droplets in the region is as much, to be able to modify the flow around them.

Further downstream, the droplets are far from each other that the inter-droplet collision does not take place. So, the droplet can be considered as a single droplet in the flow field. Depending on the We, droplets may go for secondary breakup.

The flow filed has a strong affect on the droplet evaporation. This area is called the far-field spray or dilute regime.

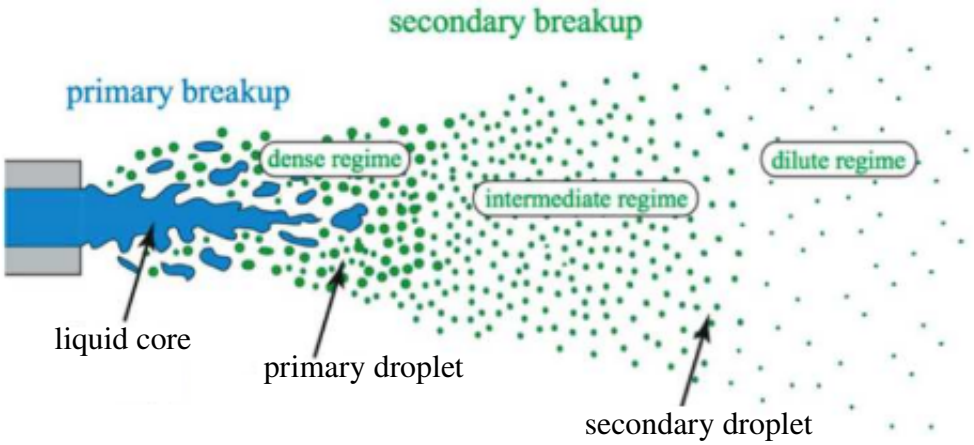

Figure 1.4: Different zones of a spray [6]

1.4 Non-Dimensionalized Numbers

The non-dimensionalized numbers that are presented in Chapters 2 and 3, are defined in this section.

Nusselt number is used to describe the heat transfer rate and Sherwood number to show mass transfer rate.

$$Nu = \frac{hd}{k} \tag{1.1}$$

$$Sh = \frac{h_m}{D/d} \tag{1.2}$$

Here, d is the droplet diameter, h is the convective heat transfer coefficient, k is the thermal conductivity of the droplet, h_m is the convection mass transfer coefficient and D is the mass diffusivity of the droplet.

Vaporisation Damköhler number is the dimensionless number relating the droplet size and turbulence to evaporation rate and, is expressed as

$$Da_v = \frac{t_{flow}}{t_{evap}} \tag{1.3}$$

Here,

$$t_{flow} = \frac{d_0}{q^{0.5}} \tag{1.4}$$

and

$$t_{evap} = \frac{R_0}{V_r} \tag{1.5}$$

Here, t_{evap} characterises the thermodynamics of vaporization of drops and t_{flow} is the relevant turbulent time scale that contributes to the evaporation. In the equation 1.4, $q = 3(u')^2/2$ represents the turbulent kinetic energy. V_r and R_0 are blowing velocity and the vapour film thickness given from the film theory of Abramzon and Sirignano [7], respectively. d_0 is the initial diameter of the droplet.

Weber number shows the ratio of the aerodynamic force and surface tension force. It is used for the determination of breakup mode, and defined as

$$We = \frac{\rho_a u_{rel}^2 d_0}{\sigma} \tag{1.6}$$

Here, ρ_a is the density of the surrounding fluid, u_{rel} is the relative velocity between the surrounding fluid and the droplet, d_0 is the characteristic length of the droplet, (mostly the droplet diameter), and σ is the surface tension coefficient.

Ohnesorge number includes the effect of viscosity that prevents deformation of the droplet. It is expressed as

$$Oh = \frac{\mu_d}{\rho_d d_0 \sigma} \tag{1.7}$$

where, ρ_d and μ_d are the density and viscosity of the droplet, respectively.

Table 1.1: Non dimensional numbers

Non dimensionalized Number	symbol	Formula
Reynolds	Re	$\frac{\rho V d}{\mu}$
Prandtl	Pr	$\frac{\mu C_p}{k}$
Weber	We	$\frac{\rho_a U_0^2 d_0}{\sigma}$
Ohnesorge	Oh	$\frac{\mu_d}{\rho_d d_0 \sigma}$
Nusselt	Nu	$\frac{hd}{k}$
Sherwood	Sh	$\frac{h}{D/d}$
Schmidt	Sc	$\frac{\mu_{vapor}}{\rho_{vapor} D_{AB}}$
Vaporisation Damköhler	Da_v	$\frac{t_{flow}}{t_{evap}}$ or $\frac{L D_m}{\eta D_t}$

Chapter 2

LITERATURE REVIEW

2.1 Introduction

This chapter is devoted to the early and current studies about droplets in motion and evaporation of those droplets. As the key focus in this research is the evaporation of single drop in turbulent flow, this chapter is divided into two main sections; One section that reviews heat and mass transfer studies of droplets, and the other section that explores the fluid dynamics and heat transfer of a single droplet or spray in turbulent flow.

2.2 Heat and Mass Transfer

As the knowledge of complex spray flow has great importance in industrial applications, many researches have focused on the understanding of the processes occurring during a spray formation, breakup and evaporation. One approach followed is studying a single droplet isolated from other drops of a spray. In this way, very precise study of the behaviour and evaporation of a droplet is possible that is applicable in the modelling and simulation of spray evaporation and prediction.

Moreover, isolated droplet modelling provides a good simplification model for the dilute region of spray flow. Therefore, in the first part, some studies are discussed that contain evaporation modelling of drops. The second part considers the effect of turbulence on evaporation of droplets.

2.2.1 Heat and Mass Transfer Modelling

The study of evaporation of a droplet in still air commenced in 1870s [8]. A simple assumption of zero temperature gradient was used to find out the relationship between the first power of the drop diameter with the evaporation rate.

In early 1930s, the study of a single droplet in laminar flow was introduced with focus on vaporization and combustion. The laminar assumption for the flow field made the study easier. Frössling [9] proposed a correlation between the evaporation rate flow field parameters. Frössling correlation was extensively used.

$$\frac{K_l}{K_0} = 1 + C_{\text{Frö}} Re_{di}^{\frac{1}{2}} Sc^{\frac{1}{3}} \tag{2.1}$$

where, $\frac{K_l}{K_0}$ is the normalised evaporative rate, Re_{di} is the Reynolds number based on the droplet diameter, $C_{\text{Frö}}$ is Frössling coefficient, and Sc is the Schmidt number and defined as

$$Sc = \frac{\mu_v}{\rho_v D_{AB}} \tag{2.2}$$

$C_{\text{Frö}}$ is found to be nearly 0.18.

In this relation, D_{AB} is the diffusion coefficient of liquid into surrounding gas, μ_v and ρ_v are the dynamic viscosity and density of the vapour phase, respectively.

Godsave [10] continued this work to account for the temperature gradient between the droplet and the surrounding atmosphere, and the relationship with evaporation rate. The work investigated the factors influencing the temperature distribution inside the droplet. It was found that there is a d^2-law relationship between

the droplet diameter and the time of evaporation expressed as

$$d^2 = d_0^2 - Kt \tag{2.3}$$

where d, d_0 and t are the initial diameter, instantaneous diameter and time, respectively. K is the evaporation rate.

Sazhin [11] developed a hydrodynamic model for droplet evaporation. The model was a modified version of the classical hydrodynamic model of Maxwell [8] and Stefan-Fuchs model [12]. In the hydrodynamic model, the diffusion of vapour from the surface of the droplet is considered assuming that it is equal to the rate of molecular detachment from the droplet surface. This method is a good simplifying practice in single droplet modelling although the inclusion of turbulence inherent in practical conditions of spray is not possible.

Refining the classical hydrodynamic model, Abramzon and Sirignano [7] developed a hydrodynamic model which is slightly different from Sazhin [11]. By considering the convective effect of droplet motion in gas field, they used film theory to develop a simple accurate algorithm for spray combustion modelling. The Stefan flow effect was considered in the film theory and the temporal variation of fluid properties were considered. The work also considered the effect of internal circulation in the evaporation. The effective thermal conductivity was used to account for the heat enhancement due to the internal circulation.

Yao et al. [13] proposed a model similar to Abramzon and Sirignano [7] and considered the effect of Stefan flow in the calculation of evaporation rate as well as the finite thickness of the thermal boundary layer around the droplet. Experimental values of *Sh* and *Nu* were used to find a relationship for the heat and mass transfer.

Yin [14] developed a 3D generic framework model for the evaporation of n-Heptane, n-Decane or n-Dodecane drops based on Abramzon and Sirignano [7] model considering internal circulation within a 2D droplet in an axisymmetric do-

main. In the model, the interaction between the droplet and the flow field has been considered. The model, then, was validated against simple analytical solutions.

Another approach in droplet evaporation modelling is the kinetic model. In this model, the separation of vapour molecules from the droplet surface in addition to the diffusion effect is taken into account. Hence, a more realistic modelling toward drop evaporation is accomplished [15, 16, 17]. Figure 2.1 shows the kinetic and hydrodynamic regions above a droplet observed in the kinetic model.

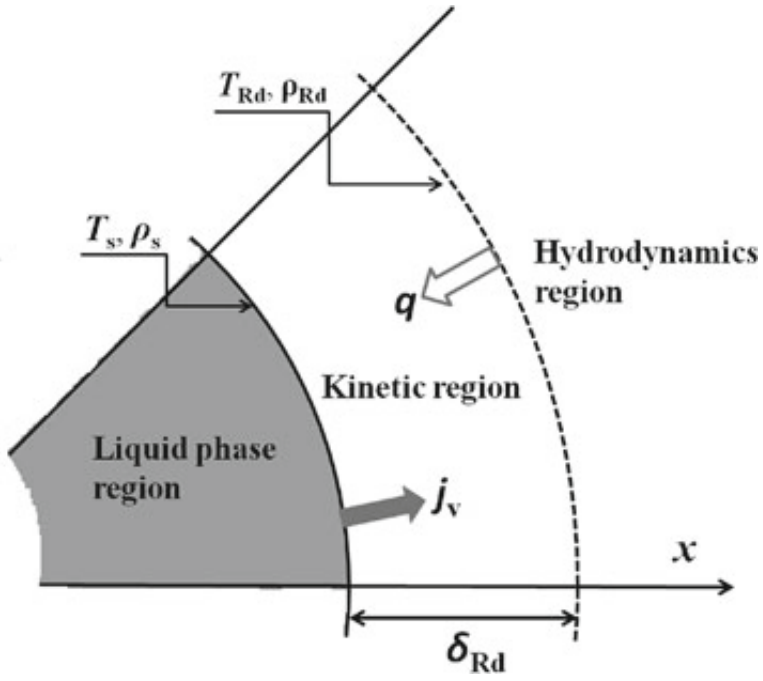

Figure 2.1: Schematic of Kinetic model showing the kinetic and hydrodynamic regions above a droplet[11]

Contrary to industrial applications, most of the research work on droplets are performed by assuming droplets as perfect spheres. Zubkov et al. [18] studied the effect of non-sphericity on the evaporation rate of a droplet, and showed that the drops are likely to be spherical at the end of the evaporation process.

2.2.2 Spray and Droplet Heat and Mass Transfer in Turbulent Flow

The investigation of turbulence effects on heat transfer of a solid sphere started in 1950s by Hsu and Sage [19] and continued by Brown and Sage [20], Galloway and Sage [21], Lavender and Pei [22], Torii et al. [23]. Turbulence has two major effects in evaporation. Firstly, it causes acceleration of convection around the droplet surface that increases the heat transfer. Secondly, it causes augmentation of vapour diffusion from the droplet that strengthens the mass transfer gradient at the surface of the drop [24].

Limited number of works considered the droplet as a droplet instead of sphere in turbulent flow. To correlate the effects of turbulence on evaporation, the turbulence intensity and Reynolds number are mostly used by modifying Frössling [9] and Ranz and Marshal [25] correlations.

$$Sh = A + BRe_d^{\frac{1}{2}} Sc^{\frac{1}{3}} (C_T)^n \tag{2.4}$$

$$Nu = A + BRe_d^{\frac{1}{2}} Pr^{\frac{1}{3}} (C_T)^n \tag{2.5}$$

Here, $C_T = Re_d I$, the turbulent intensity, where I is the flow mean-stream velocity defined as, $I = u'/U$. u' is the r.m.s value or fluctuating velocity and Re_d is based on drop initial diameter. Pr is the Prandtl number and is defined as

$$Pr = \frac{\mu C_p}{k} \tag{2.6}$$

where, μ the viscosity, C_p the specific heat at constant pressure and, k the thermal conductivity are the properties of the surrounding fluid. Variety of values for A, B, n and C_T have been found by different authors [22, 26, 27].

A review of findings showed that there is no unified correlation predicting the heat and mass transfer of a sphere or droplet in turbulent flow [28].

Masoudi and Sirignano [29] developed a three dimensional model for the vaporization of a droplet interacting with a single rotating vortex. The work concluded that the Stefan flux blocks the influence of vortex collision on the droplet. Temporal variation of Sh and Nu were investigated and it was shown that the Nusselt number of evaporating droplets is nearly the same as that of the non-evaporating droplet. Though, the Sherwood number of evaporating drops changes significantly.

Gökalp et al. [30] found a distinction between n-heptane and n-decane droplet evaporation rate dependence to turbulence intensity. The work concluded that as n-decane is less volatile, the evaporation normally takes place slower near the droplet. In turbulent flow, turbulent structure increases the evaporation of n-decane by removal of the vapour quickly and impact on the evaporation more than n-heptane. Introducing vaporisation Damköhler number as a dimensionless number for predicting the evaporation rate of different liquids, a relationship between droplet size, turbulence and evaporation rate is considered. It is observed that at low values of Damköhler number, turbulence affects mass transfer of droplet. The idea of using Damköhler number is given from the ambient laminar flow theory of the vapour thickness at the vicinity of the drop surface.

Later, Hiromitsu and Kawaguchi [31] found that Damköhler number application is limited to evaporation of low-temperature droplets and the influence of turbulence on less volatile liquids is more noticeable.

Wu et al. [32] verified outcomes of Gökalp et al. [30] and Hiromitsu et al. [31] and based on their experiments, proposed a relation for the droplet average vaporisation rate, K_{vct} and Damköhler number to relate the drop vaporization rate and turbulence. This equation illustrates the reduction of vaporisation with an

increase of Damköhler number. The findings expressed that the turbulent intensity increases the vaporization rate when compared to laminar flow.

$$\frac{K_{vct}}{K_{\text{Frö}}} = 0.74 Da_v^{-0.115} \tag{2.7}$$

In the above relation, $K_{\text{Frö}}$ is the droplet normalised vaporisation rate under laminar convective condition, and is expressed as a function of the vaporisation rate under stagnation condition and $C_{\text{Frö}} = 0.27$, as given below.

$$\frac{K_{\text{Frö}}}{K_{vs}} = 1 + C_{\text{Frö}} Re_d^{\frac{1}{2}} Sc^{\frac{1}{3}} \tag{2.8}$$

Later, Wu et al. [33] confirmed the correlation of Wu et al. [32] for a wider range of hydrocarbons with some modification.

Some authors have found the pure effect of turbulence on vaporisation by testing the droplet in a zero-mean-velocity flow condition [34, 35, 36]. Birouk et al. [36] studied a suspended droplet in isotropic homogeneous turbulent field by determining the average evaporation rate. The work found out different evaporation rate for different fuels. Though, all the fuels showed an increase of evaporation rate due to turbulence.

Another correlation for evaporation rate is introduced by Birouk and Gökalp [37] which is different from equation of Wu et al. [32] since the turbulent Reynolds number is used instead of the droplet Reynold number. The turbulent Reynolds number is defined as

$$Re_{turb} = q^{0.5} d_0 / \nu_a \tag{2.9}$$

where q is the turbulent kinetic energy and defined as $q = 3u'^2/2$. This correlation is derived from the experiments of five mono- and bi- component n-alkane single droplets and is in agreement with the results of Ohta et al. [34] and Whitaker

[38]. From these experiments it was found that the impact of turbulence on mono-component droplets follows the d^2-law. However, the increase of evaporation of bi-component drops is limited to lower turbulence level. At higher levels of turbulence, there is no more augmentation in evaporation rate.

To quantify how turbulence can be effective on evaporation rate, Birouk and Gökalp [28] redefined Damköhler number. Then, it was deduced that evaporation rate is affected by turbulence when Damköhler number is much less than unity. Therefore, turbulence does not seem to influence the vaporisation rate for bigger values of Damköhler number.

Wang and Rutland [39] studied evaporation process of droplet in turbulent flow field using DNS. The two-way coupling interaction between the droplets and turbulent flow was considered. The work showed that non-evaporating droplets suppress turbulence while evaporating drops increase it.

Schroll et al. [40] investigated the effect of evaporation on the autoignition process in turbulent flow. Lagrangian method was used to track the droplet and DNS was used for CFD modelling. It was concluded that the droplet size has an impact on the evaporation rate and, related the turbulent dissipation rate with the evaporation augmentation.

Using DNS method, Zoby et al. [41] studied evaporating burning droplet arrays. A model was used to couple a mass conservative Level Set approach with the Ghost Fluid method. It was concluded that the only effect of turbulence on the evaporation is due to scattering of vapour field away from the droplet.

Birouk and Fabbro [42] conducted a series of tests to examine the pressurised turbulence impact on evaporation. The research discovered that droplet temporal variation in high pressure condition under turbulent condition, follows d^2-law and is affected by turbulence. Although, higher turbulent intensities affect the evaporation less than lower ones due to the fact that the role of turbulence in evaporation

is convecting vapour away from the droplet. Hence, after disappearance of the vapour, turbulence has no more effect. Additionally, the higher pressure makes the evaporation less and this trend is not affected by turbulence, which is regarded to the high dependency of the heat transfer to ambient pressure rather than turbulence. Some more features of turbulence effects on vaporisation can be found in [24].

Shinjo et al. [43] considered the turbulence mixing and modulation in a dense spray with DNS. The study considered heat and mass transfer in their study. The investigation included the effects of droplet on vortex shedding, turbulence generation and mixing.

Méès et al. [44] used a 3 dimensional imaging system to capture droplet trajectory. The images showed vapour generated around the droplet. It was observed that there is non-constant evaporation rate in turbulent flow contrary to laminar case based on experimental analysis. The work concluded that the evaporation rate may vary with turbulence but needs more investigation.

The impact of droplet size on evaporation rate in ambient turbulence environment is studied by Verwey and Birouk [45]. The turbulence effectiveness is examined with the ratio of Kolmogorov length scale to drop diameter and molar concentration gradient at the surface of droplet. Both, droplet size and turbulence intensity showed an important role in evaporation rate. The linear temporal reduction of squared normalised diameter agreed with the d^2-law for all tests.

Marti et al. [46] found that the effect of turbulence on evaporation for large droplets is less than the effects of mean flow convection. This finding is in contrast with Verwey and Birouk [47]. The reason for this discrepancy may have originated from different mean flow conditions of the experiments. In the work of Marti et al. [46] non zero mean flow condition is considered while Verwey and Birouk [47] evaluates pure turbulence to highlight the effects of turbulence.

Verwey and Birouk [47] discovered that the evaporation of droplets bigger than the Kolmogorov length scale which is equal to the smallest eddies size are influenced by turbulence. But evaporation of droplets smaller than the Kolmogorov length scale show insignificant dependence on turbulence. It was also shown that larger droplets do not obey d^2-law contrary to the smaller one. Finally, a modified correlation for evaporation rate including temperature and pressure effects is proposed. The benefit of the equation is the inclusion of the effects of the droplet size as well as the ambient flow pressure and temperature in the turbulent vaporization rate.

2.3 Need For The Present Study

A brief review of existing studies about heat and mass transfer of droplet in different type of flows reveals the lack of study for evaporation phenomena of a moving droplet in turbulent flow. Despite many efforts for investigating the effect of turbulence on evaporation has been carried out, considerable researches have focused on suspended droplet but limited studies have considered freely falling droplet, (which happens in real conditions), in turbulent flow. On the other hand, the vapour phase is mostly not considered as a separate phase. Therefore, the vapour and flow structure interaction remains unexplored. So, there are still gaps in understanding of the combination of convection and diffusion effects simultaneously on the evaporation of a freely falling droplet in turbulent flow.

To this end, the first objective of the present work is to develop a CFD code, capable of modelling evaporation process and considering vapour, liquid and gas phases separately. This code will facilitate the investigation of vapour concentration and mixing during evaporation in turbulent flow. Besides, the turbulence modulation as the result of vapour mixing can be studied.

The second objective is studying the evaporation process of a single droplet freely falling in a turbulent channel flow considering the flow structure and droplet interaction by means of the developed code. Effect of different Reynolds number on the evaporation is studied and compared to the laminar flow and quiescent air results. The vapour phase is investigated to see how it will affect the turbulent flow structure and vice-versa.

In addition to improving the evaporation rate by turbulent structures, interesting characteristics emerge due to its effect on the vapour mixing which could lead to consequences on the associated evaporation rate and heat transfer.

A summary of studies reviewed in this chapter is presented in Table 2.1.

Table 2.1: Summary of literature review: Evaporation, Atomisation and Turbulence

Field of Study	Autor	Application	Remarks	Study Method
Evaporation of spray and droplets	Godsave [10]	evaporation of droplet under temperature gradient in laminar flow	found d^2law	experimental
	Sazhin [11]	laminar flow	considering vapour diffusion	hydrodynamic model
	Abramzon et al.[7]	study of lifetime of droplets in spray	considering the effect of internal circulation in the evaporation	numerical
	Yao et al. [13]	results depend on the experimental values of *Sh* and *Nu*	finite thickness of the thermal boundary layer around the droplet	numerical
	Yin [14]	laminar	the interaction between the droplet and the flow field has been considered	numerical

Table 2.1: Continued...

Field of Study	Autor	Application	Remarks	Study Method
Evaporation of spray and droplets	Zubkov et al. [18]	heat transfer and evaporation of droplet	effect of non-sphericity on the evaporation	numerical
Turbulence effects on evaporation	Masoudi et al.[29]	droplet/vortex interaction along with vaporisation	effect of a single vortex on evaporation	numerical
	Gökalp et al. [30]	evaporation rate as a function of turbulence with different volatility	turbulent length scale 5 times of drop diameter	experimental
	Hiromitsu et al.[31]	effect of turbulence on evaporation of drop in hot air	the results were contrary to Gökalp et al. [30]	experimental
	Wu et al. [32]	evaporation of single droplet in turbulent flow	study in ambient air temperature	experimental

Table 2.1: Continued...

Field of Study	Autor	Application	Remarks	Study Method
Turbulent effects on evaporation	Wu et al. [33]	evaporation of single droplet in different turbulent intensities	study in ambient air temperature	experimental
	Ohta et al. [34]	combustion and evaporation in zero mean velocity turbulent flow	suspended droplet	experimental
	Birouk et al. [36]	a model for the turbulence effects on droplet vaporization in terms of the ratio between a turbulence diffusivity and the molecular diffusivity	normal pressure and temperature	experimental
	Birouk et al.[37]	effect of turbulence on evaporation depends on droplet size	normal pressure and temperature and suspended droplet	experimental
	Wang et al.[39]	comparison of two-way coupling interaction between the droplets and turbulent flow in non-evaporating droplets with evaporating drops	isotropic turbulence in high temperature	numerical

Table 2.1: Continued...

Field of Study	Autor	Application	Remarks	Study Method
Turbulent effects on evaporation	Schroll et al. [40]	effect of evaporation on the autoignition process in turbulent flow	related the turbulent dissipation rate with the evaporation augmentation	numerical
	Zoby et al. [41]	couple of a mass conservative Level Set approach with the Ghost Fluid method	droplet combustion	numerical
	Birouk et al.[42]	effect of turbulence on elevated pressure	room temperature	experimental
	Birouk et al.[24]	effect of turbulence on elevated pressure and temperature	suspended droplet	experimental
	Shinjo et al. [43]	effects of droplet on vortex shedding, turbulence generation and mixing	finite-size droplets/ligaments in a dense fuel spray	numerical
	Méès et al. [44]	droplet trajectory along with evaporation changes due to turbulence	ambient pressure and temperature	experimental
	Verwey et al.[45]	effect of droplet size on vaporisation in turbulent atmosphere	ambient pressure and temperature	experimental

Table 2.1: Continued...

Field of Study	Autor	Application	Remarks	Study Method
Turbulence effects on evaporation	Marti et al. [46]	turbulence scale smaller than the droplet size	pinned droplet	experimental
	Verwey et al.[47]	turbulence effect on elevated temperature and pressure	suspended droplet	experimental

Chapter 3

MOTIVATION, OBJECTIVES AND SCOPE OF WORK

3.1 Introduction

In the previous chapters, an overview of the physical phenomena that affect a droplet in a spray are discussed. Moreover, a review of the literature on both droplet evaporation and turbulent effects are presented. In this section the areas where more investigation is required to have a deeper understanding about spray evaporation and cooling is outlined. Then, the objective of the research is explored. Finally, the thesis outline is presented.

3.2 Aims

It was identified that the previous experimental studies available mainly focused on the evaporation of single droplet in zero mean velocity. This means that in most of the researches the droplet was suspended. The influence of the mean flow convection in addition to the turbulence was mostly not properly studied.

On the other hand, in numerical studies it was found that the presence of vapour field around the droplet as a separate phase is ignored by assuming that the media around the droplet is a mixture of the air and the vapour.

Due to the importance of the single droplet study and the complicated mechanisms associated during the evaporation, the present research is devoted to the investigation of a single droplet undergoing an evaporation processes. The application of this study is for the very dilute regime zone after the secondary breakup of sprays where the influence of neighbouring drops are small and can be ignored. So the most important interaction is between the droplet and the ambient gas. To study the effect of turbulence on the evaporation, the drop is considered in a turbulent flow field. The Weber number is assumed to be small enough, $We < 9$, so that, the breakup does not take place [48].

To observe the vapour phase mixing and considering the effect of the vapour into the ambient gas, a three phase mixture is considered which is one of the novelties in this research. The presence of vapour as a separate phase from the ambient gas assists effective cognizance of the mutual influence of vapour and turbulent flow. Here, only the dispersion and the evaporation of droplets in non-reactive flows are taken into account.

This research provides a CFD tool for the modelling of the dispersion and evaporation phenomena by using an innovative method of considering different velocities in the interface to overcome the issue of volume change during the evaporation process. This is an Open source code that can be used by OpenFOAM users to simulate the evaporation modelling.

Numerical LES simulation study of the droplet in a fully-developed channel flow is performed with the developed code to generate a data set with turbulent statistics and heat and mass transfer. The physical phenomena involved in the flow structure and thermal characteristics is scrutinised and explained. Besides, valida-

tion of the numerical method is performed by a set of experimental investigations.

3.3 Research Methods

The current research consists of numerical and experimental investigation. A numerical code is developed based on an innovative approach for modelling droplet evaporation. The VOF method used in the code is mass conservative but not generally volume conservative. The code has been modified by an innovative method to be able to accommodate extra volume generated in evaporation process. For the purpose of validation of the numerical model, some experimental investigations are performed. Subsequently, a series of numerical studies are conducted to simulate the evaporation of a droplet in turbulent gas flow field.

3.3.1 Numerical Investigation

For the numerical investigation, the VOF method was used to solve the Navier-Stokes equations. Particular attempt was done to accommodate three phases in addition to the source terms associated with the phase change mechanism. To overcome the volume change phenomena during the evaporation, a novel technique of using different velocities in droplet interface is introduced. The energy equation according to the requirements of the case is employed.

To study the turbulent flow effects on evaporation, LES model was used. Refined mesh was utilised to capture small perturbations and to resolve any interaction between the liquid, vapour and the ambient gas. To avoid spurious currents near the interface small time steps were deployed.

Two cases of turbulent flow with different Reynolds number are studied. To compare the results, a laminar flow case as well as a stand still case is also considered.

Evaporation rate of different cases along side with the vapour field and temperature field are compared. Q-criterion, vorticity field and dissipation rate of turbulent cases are compared. The reason for different evaporation rate of turbulent cases are discussed in detail.

3.3.2 Experimental Investigation

With the intention of producing fully developed flow, a long channel was fabricated accompanied by flow straightener, flow diffuser, visible test area and special amendments for velocity and temperature recording. The air flow was delivered via a central air supply. After the air pressure reached to a specified amount it was released to the air channel by passing through a control valve and a ball valve. After a specified amount of the time required to have fully developed air flow, the water droplet was released into the visible test area of the channel. At the same time, the high speed camera with particular set-up was used for capturing images. Afterwards, captured images were transferred to computer for post-processing analysis.

Using image processing techniques, the results of the experimental tests were compared with the numerical data.

3.4 Thesis Organisation

Chapter 1 briefly introduces applications of droplet evaporation and the fluid mechanics and heat transfer mechanisms associated with this phenomena. Moreover, the motivation for the present research, the aims and objectives, and an overview of the methods are provided.

Chapter 2 describes a review of studies about heat and mass transfer of droplet with specific attention toward turbulence effects on drop evaporation. It also provides a review of fluid dynamic studies of droplet.

In Chapter 3, the objectives and research methods of the present research is described.

In Chapter 4, detailed explanation about numerical methods and mathematical modelling connected to the present studies as well as the innovative method used for the droplet evaporation modelling are explained. A flow chart of the developed code is also provided.

In Chapter 5, details of the experimental system used in the present work are explained, along side the description of experimental parameters, and the uncertainties in the measured parameters.

Chapter 6 provides the results and discussion from the numerical and experimental investigation presented, which comprises the fluid-dynamics and heat and mass transfer characteristics of droplet.

The conclusions of this research are provided in Chapter 7, as well as suggestions for future work.

Chapter 4

NUMERICAL STUDY

4.1 Introduction

In this chapter the methodology used for numerical simulation as well as the equations applied for the CFD code are detailed. First of all, the volume-of-fluid method is explained. This section is followed by a discussion about the other equations required to solve multiphase fluid flow including pressure equation, pressure-velocity coupling, energy equation, turbulence modelling as well as the strategy for decreasing spurious currents around the interface. The mass transfer equation is also included in this chapter. A section is devoted to the strategies used for turbulence generation in numerical studies. Finally, the code that is developed for the simulation of evaporation is described. All the equations used for the solver, as well as the innovative method used for interface velocity in the developed CFD code is explained.

4.2 Volume of Fluid Method

The fractional volume of fluid (VOF) is a surface capturing method of employing a marker function representing the fraction of the species in each cell, α_i, for which the unity value of the function shows that the cell is fully wetted by the fluid and zero value indicates that it is empty of the fluid

$$\alpha_i = \frac{\textit{volume of the species 'i' in the cell}}{\textit{total volume of species in the cell}} \tag{4.1}$$

and hence,

$$\alpha_i = \begin{cases} 1 & \text{the cell is fully wet with species 'i'} \\ 0 < \alpha_i < 1 & \text{the cell is partially filled with species 'i'} \\ 0 & \text{the cell is empty of species 'i'} \end{cases} \tag{4.2}$$

The cells containing the interface would have values of the function between 0 and 1 and, the position of the interface would be approximated in this way. This method was first introduced by Hirt et al. [49] and due to easy implementation potential, has been widely employed in CFD software for example OpenFOAM, Fluent, CFX and others.

4.2.1 Momentum Equation

The velocity field on the interfaces in the VOF method is considered continuous which means that there is no relative velocity between the phases. As far as the mesh is fine enough, this assumption results in correct solutions [50]. Therefore, the mass averaged velocity and the volume averaged velocity would be equal.

In a multiphase problem, the surface tension between two different phases imposes a surface tension force. To model the effects of the surface tension at the

interfaces, the Continuum Surface Force (CSF) model is applied. Brackbill et al. [51] showed that the surface tension is related to the total tensile forces acting on the interface. Then, by calculating the integral of the acting forces on the surface the following relation for the surface tension force is found:

$$\overrightarrow{F}_{\sigma} = \sigma\kappa\overrightarrow{\nabla}\alpha_q \tag{4.3}$$

where κ is the mean interface curvature and defined as

$$\kappa = \overrightarrow{\nabla}.\left(\frac{\overrightarrow{\nabla}\alpha_q}{|\overrightarrow{\nabla}\alpha_q|}\right) \tag{4.4}$$

α_q is the volumetric fraction of phase q. Equation 4.3 is valid for the cases with constant surface tension, as considered in this research.

To simplify the pressure gradient calculation at the non vertical walls, with no slip velocity boundary condition, Berberovic et al. [52] defined p_{rgh} to separate term ρg from the p term.

$$p_{rgh} = p_m - \rho_m\overrightarrow{g}\overrightarrow{x} \tag{4.5}$$

where $\vec{x}$ is the position vector and p_m and ρ_m are the mixture pressure and density, respectively. To find the pressure gradient, equation 4.5 is used:

$$\overrightarrow{\nabla}p_m = \overrightarrow{\nabla}p_{rgh} + \rho_m\overrightarrow{g} + \overrightarrow{g}\overrightarrow{x}.\overrightarrow{\nabla}\rho_m \tag{4.6}$$

From equation 4.6, it is obvious that the modified pressure gradient contains the static pressure gradient and the body force of gravity as well as a term from the gradient of the density.

Therefore, the system of equations for the VOF for two-phase flow, with no mass transfer between the phases, would be as given bellow and is called the

Weller-VOF formulation [50].

$$\begin{cases} \overrightarrow{\nabla}.\vec{u} = 0 \\ \frac{\partial}{\partial t}(\rho_m \vec{u}) + \overrightarrow{\nabla}.(\rho_m \vec{u} \otimes \vec{u}) = -\overrightarrow{\nabla} p_{rgh} + \overrightarrow{\nabla}.[\mu_m(\nabla\vec{u} + \nabla\vec{u}^T)] - \overrightarrow{xg}\overrightarrow{\nabla}\rho_m \\ \qquad\qquad + \sigma\kappa\overrightarrow{\nabla}\alpha_q \\ \frac{\partial \alpha_q}{\partial t} + \overrightarrow{\nabla}.(\alpha_q \vec{u}) + \overrightarrow{\nabla}.(\alpha_q \alpha_p \vec{v}_{qp}) = 0 \\ \sum_{k=1}^{n} \alpha_k = 1 \end{cases} \tag{4.7}$$

where $\vec{v}_{qp}$ is the relative velocity between phase p and q. More details regarding this velocity can be found in section 4.8.1.

4.2.2 Pressure Equation

There are different methods for discretisation of spatial and temporal derivatives of the VOF system of equations 4.7. Here the Euler implicit difference scheme for the semi-discretised form of the momentum equation is used [50].

$$a_P \vec{u}_P = \overrightarrow{H}(\vec{u}) - \overrightarrow{\nabla} p \tag{4.8}$$

where a_p is the diagonal coefficient of the discretisation matrix. The $\overrightarrow{H}(\vec{u})$ is the operator that accounts for the advective and diffusive terms as well as the source terms and is expressed as:

$$\overrightarrow{H}(\vec{u}) = -\sum_f a_N \vec{u}_N + \frac{\vec{u}^0}{\Delta t} \tag{4.9}$$

where $\vec{u}^0$ is the velocity at the previous time step and a_n is the off-diagonal matrix.

Then, discretisation of the continuity equation gives

$$\overrightarrow{\nabla}.\vec{u} = \sum_f \vec{u}_f.\overrightarrow{S}_f = 0 \tag{4.10}$$

By considering the magnitude of the velocity at the cell centre from the relationship 4.8,

$$\vec{u}_P = \frac{\overrightarrow{H(\vec{u})}}{a_P} - \frac{1}{a_P}\overrightarrow{\nabla}p \tag{4.11}$$

and interpolating at the face,

$$\vec{u}_f = \left(\frac{\overrightarrow{H(\vec{u})}}{a_P}\right)_f - \left(\frac{1}{a_P}\right)_f \left(\overrightarrow{\nabla}p\right)_f \tag{4.12}$$

an equation for the pressure would be obtained, using equation 4.12 on equation 4.10 which is called the Pressure Poisson Equation.

$$\overrightarrow{\nabla}.\left(\frac{1}{a_P}\overrightarrow{\nabla}p_{rgh}\right) = \overrightarrow{\nabla}.\left(\frac{\overrightarrow{H(\vec{u})}}{a_P}\right) \tag{4.13}$$

4.2.3 Pressure Velocity Coupling

Although, by solving the differential equations of the system of equations 4.7, the pressure equation may be derived, due to the need for discretisation, it cannot be guaranteed that the discretised form of the pressure field is compatible with the corresponding terms in the momentum and the continuity equations. Besides, it is hard to assure that the velocity field from the calculated pressure satisfies the continuity and momentum equations simultaneously.

On the other hand, it is possible to find the pressure field from the discretised form of the momentum and continuity equation which satisfies both the momentum and the continuity equations [53].

To solve the complete system of equations over the whole domain there are two approaches; simultaneous and segregated. The simultaneous approach is the

one that solves all of the domain at the same time and is useful when there are a small number of points in the domain. On the other hand, the segregated approach is suitable when there are large number of cells.

There are three segregated inter-equation coupling methods between pressure and velocity field: PISO, SIMPLE and PIMPLE.

SIMPLE stands for Semi-Implicit Methods for Pressure-Linked Equations and is beneficial for steady-state problems. The under-relaxation in the momentum equation is applied to promote the convergence in the SIMPLE algorithm. On the other hand, the relaxation of the pressure equation is used to satisfy the exact velocity correction [54].

PISO initially introduced by Issa [53] is originally developed for transient flow. It is also known as the extension for SIMPLE method. PISO stands for Pressure Implicit with Splitting of Operator. The PISO loop continues until a predetermined tolerance is reached. As already mentioned, the PISO loop has one more corrector step and does not need for the relaxation.

The PIMPLE algorithm is the combination of the PISO and the SIMPLE algorithms and is used in OpenFOAM to benefit both algorithms. In the PIMPLE algorithm the pressure is re-calculated based on the desired numbers of corrections to prevent the divergence of the simulation using the benefit of the relaxation, which is used in the SIMPLE method, while the time step is not as small as the PISO, since the Courant number does not necessarily have to be less than one. In view of its suitability, PIMPLE algorithm has been used in the current study for pressure-velocity coupling.

4.2.4 Energy Equation

The conservation of energy, as part of the Navier-Stokes equations, is determined by the first law of thermodynamics, that is saying that the sum of all forms of

energy in an isolated system remains constant. Thus, for any control volume, the energy conservation equation is as given as [54],

$$\frac{\partial}{\partial t}(\rho e) + \overrightarrow{\nabla}.(\rho \vec{u} e) = -\nabla.\dot{q}_s - \overrightarrow{\nabla}.(p\vec{u}) + \overrightarrow{\nabla}.(\tau.\vec{u}) + \overrightarrow{f}_b.\vec{u} + \dot{q}_v \tag{4.14}$$

where e is the total energy per unit mass, $\dot{q}_s$ is the energy rate transfer across the surface of the control volume per unit mass, $\dot{q}_v$ is the heat source across the surface area of the control volume per unit mass, f_b is the body force term and τ is the viscous stress tensor.

The energy equation can also be rewritten in terms of temperature. For this purpose, the internal energy should be expressed in terms of enthalpy. Enthalpy should be assumed to be a function of pressure and temperature, i.e., $\hat{h} = \hat{h}(p, T)$. Therefore,

$$e = \hat{u} + \frac{1}{2}\vec{u}.\vec{u} = \hat{h} - \frac{p}{\rho} + \frac{1}{2}\vec{u}.\vec{u} = \hat{h}_0 - \frac{p}{\rho} \tag{4.15}$$

where $\hat{u}$ is the internal energy. Then, after some mathematical manipulation the complete form of the energy equation would be [54], as given by

$$\frac{\partial}{\partial t}(\rho C_p T) + \nabla.(\rho C_p \vec{u} T) = -\nabla.\dot{q}_s + \rho T \frac{DC_p}{Dt} - \left(\frac{\partial(Ln\rho)}{\partial(LnT)}\right)\frac{Dp}{Dt} + (\overrightarrow{\tau} : \overrightarrow{\nabla}\vec{u}) + \dot{q}_v \tag{4.16}$$

where $C_p = (\frac{\partial \hat{h}}{\partial T})_p$is the specific heat in constant pressure. The heat flux can be replaced with Fourier's law, $\dot{q}_s = -k\nabla T$, where k is the thermal conductivity of the substance. The term $\overrightarrow{\tau} : \overrightarrow{\nabla}\vec{u}$ can be neglected for low Mach number incompressible flows. Besides, the expression, $\frac{\partial(Ln\rho)}{\partial(LnT)}$, can be ignored if the density is assumed to be independent of the temperature. Therefore, the simplified form of the energy equation is obtained as

$$\frac{\partial}{\partial t}(\rho C_p T) + \nabla.(\rho C_p \vec{u} T) = \nabla.(k \nabla T) + \rho T \frac{DC_p}{Dt} + \dot{q}_v \tag{4.17}$$

4.3 Discretisation

The solution of partial differential equations such as 4.7 in the continuum field requires discretisation. Several methods are available for this purpose, such as the Finite Difference Method (FDM), the Finite Element Method (FEM) and the Finite Volume Method (FVM) for which each one has advantages and disadvantages. The cell-centred Finite Volume Method is used in this study as it is implemented in the OpenFOAM code.

In the FVM the discretisation starts from the integration over the volume of each cell. Hence, the transport equation of ϕ inside the domain is obtained as,

$$\underbrace{\frac{d}{dt}\int_V \phi dV}_{\text{Temporal derivative}} + \underbrace{\int_V \nabla.(\bar{u}\phi) dV}_{\text{Convective term}} - \underbrace{\int_V \nabla.(\Gamma_\phi \nabla\phi) dV}_{\text{Diffusive term}} = \underbrace{\int_V S_\phi(\phi) dV}_{\text{Source term}} \tag{4.18}$$

For a control volume V the computational point P is located at the centroid of the volume such that:

$$\int_{V_P} (x - x_P) dV = 0 \tag{4.19}$$

The face area vector, S_f, is located at the centroid of face f. The variation of a generic scalar magnitude, ϕ, is represented by,

$$\phi_P = \bar{\phi} = \frac{1}{V}\int_V \phi(X) dV \tag{4.20}$$

where the centroid is given by equation 4.19. By utilising Gauss's theorem, the volume integral is converted to a surface integral producing discrete equations for

each term in the governing equations. Therefore, equation 4.18 is converted to,

$$\frac{d}{dt}\int_V \phi dV + \underbrace{\oint_{\partial V} d\boldsymbol{S}.(\bar{u}\phi)}_{\text{Convective flux}} - \underbrace{\oint_{\partial V} d\boldsymbol{S}.(\Gamma_\phi \nabla_\phi)}_{\text{Diffusive flux}} = \int_V \boldsymbol{S_\phi}(\phi) dV \tag{4.21}$$

Discretisation methods for each term will be discussed in detail in the following sections.

4.3.1 Discretisation of The Convective Term

The convective term from equation 4.21, represented by the divergence operator, can be expressed as

$$\underbrace{\int_V \nabla.(\bar{u}\phi)dV}_{\text{Convective term}} = \underbrace{\oint_{\partial V} d\boldsymbol{S}.(\bar{u}\phi)}_{\text{Convective flux}} = \sum_f \int_f d\boldsymbol{S}.(\bar{u}\phi)_f \approx \sum_f \boldsymbol{S_f}.(\bar{u\phi})_f$$

$$= \sum_f \boldsymbol{S_f}.(u\phi)_f \tag{4.22}$$

The approximation of the face value of ϕ_f, from the face centroid magnitudes is the challenging problem in cell-centred finite volume discretisation. For the central differencing (CD) scheme, the value of ϕ_f is derived from the linear interpolation of the cell values at the point $\boldsymbol{P}$ and the neighbouring cell $\boldsymbol{N}$. Therefore, the interface value, ϕ_f, is calculated from the following equation,

$$\phi_{f,CD} = f_{CD}(\phi_P - \phi_N) + \phi_N \tag{4.23}$$

Here, the interpolation factor, f_{CD}, is defined as $f_{CD} = \frac{f\bar{N}}{P\bar{N}}$. This scheme makes unphysical spatial oscillations in convection-dominated flows and causes boundedness of the solution [55].

To ensure the unconditional boundedness, the upwind differencing (UD) scheme is proposed that determines the face value ϕ_f from the direction of the flow:

$$\phi_{f,UD} = f_{UD}(\phi_P - \phi_N) + \phi_N \tag{4.24}$$

where the weighting factor f_{UD} is as following:

$$f_{UD} = \begin{cases} 1, & F_f > 0 \\ 0, & \text{otherwise} \end{cases} \tag{4.25}$$

In the above relation, F_f is the face flux. Generally speaking, upwind scheme suffers from lower accuracy due to the numerical diffusion.

To maintain the boundedness with logical accuracy, OpenFOAM code yields blended schemes which are derived from combining the upwind and central differencing schemes. The face value of ϕ_f is then formulated as

$$\phi_f = (1 - \omega)\phi_{f,UD} + \omega\phi_{f,CD} \tag{4.26}$$

Here, ω is a blending factor which for the upwind scheme $\omega = 0$, and for the central differencing $\omega = 1$.

The evaluation of the blending factor is performed by various methods. However, the promising method which is used in this study is called Total Variation Diminishing (TVD) method [56, 57]. The specification of this method requires creating a differencing scheme with second-order accuracy without the spurious oscillation. Another challenge is the evaluation of the blending factor ω. Among all the proposed methods Van Leer method is chosen for the purpose of the current research. The blending factor is given in equation 4.27 that was proposed by van Leer [58].

$$\omega = \frac{r_f + |r_f|}{1 + |r_f|} \tag{4.27}$$

where, r is the ratio of successive gradients of the interpolated variable. In OpenFOAM, r is obtained by the V-scheme,

$$r_f = \frac{\phi_C - \phi_U}{\phi_D - \phi_C} \tag{4.28}$$

Here, C denotes to the central node, D refers to the downwind node to the C and U is upwind node to the node C [54].

4.3.2 Discretisation of The Diffusion Term

The discretisation of the diffusion term is investigated separately from the convection term as they represent different physical phenomena. The diffusion term is represented by the Laplacian operator and obtained from equation 4.21,

$$\underbrace{\int_V \nabla.(\Gamma_\phi \nabla\phi) dV}_{\text{Diffusion term}} = \underbrace{\oint_{\partial V} d\boldsymbol{S}.(\Gamma_\phi \nabla\phi)}_{\text{Diffusive flux}} = \sum_f \int_f d\boldsymbol{S}.(\Gamma_\phi \nabla\phi)_f$$
$$\approx \sum_f \boldsymbol{S_f}.(\overline{\Gamma_\phi \nabla\phi})_f = \sum_f \boldsymbol{S_f}.(\Gamma_\phi \nabla\phi_f) \tag{4.29}$$

In equation 4.29 the gradient term exists that needs special treatment during discretisation. In orthogonal mesh, the gradient term can be easily obtained,

$$\boldsymbol{S}.(\nabla\phi)_f = |\boldsymbol{S}| \frac{(\phi_N - \phi_P)}{|\boldsymbol{d}|} \tag{4.30}$$

In cases where the mesh is non-orthogonal, the gradient can be split to an orthogonal and a non-orthogonal section.

$$\boldsymbol{S}.(\nabla\phi)_f = \underbrace{\boldsymbol{\delta}.(\nabla\phi)_f}_{\text{orthogonal part}} + \underbrace{\boldsymbol{k}.(\nabla\phi)_f}_{\text{non-orthogonal part}} \tag{4.31}$$

where, δ is the vector component parallel to $\boldsymbol{d}$ and $\boldsymbol{k}$, and it must satisfy $\boldsymbol{S} = \boldsymbol{k} + \boldsymbol{\delta}$. The vector component value is determined from the over-relaxed approach offered by Jasak [59].

$$\boldsymbol{\delta} = \frac{\boldsymbol{d}}{\boldsymbol{d}.\boldsymbol{S}}|\boldsymbol{S}|^2 \tag{4.32}$$

4.3.3 Discretisation of Source Term

The source term in equation 4.18, appears in the governing equations due to, for example, turbulence model, chemical reactions, radiation and phase change. This term affects not only the physical process of the flow but also influences the numerical behaviour of the problem. If it is correctly managed, it may improve the stability. Normally, it is recommended to evaluate the negative values (sinks) implicitly, and treat positive values (sources) explicitly [54]. Therefore,

$$\int_V S_\phi(\phi)dV = \underbrace{S_c V}_{\text{constant term}} + \underbrace{S_p V \phi}_{\text{linear term}} \tag{4.33}$$

4.3.4 Temporal Discretisation

In case of steady-state flow, the variable ϕ is independent to time means that $\phi_C^{t+\Delta t} = \phi_C^t$ when $t \to \infty$. So, the temporal derivative term would be zero. On the other hand, in transient flow the variable ϕ changes by time marching and the temporal derivative is not zero thus, requiring discretisation. To evaluate the temporal derivative of equation 4.18, the Taylor expansion of ϕ about a time direction is required,

$$\phi(t+\Delta t) = \phi(t) + \frac{\phi(t)}{\partial t}\Delta t + \frac{\partial^2\phi(t)}{\partial t^2}\frac{\Delta t^2}{2!} + ... \tag{4.34}$$

From equation 4.34 by ignoring the higher order derivatives and assuming linear variation of the variable ϕ along the time step Δt, following relations are obtained.

$$\left(\frac{\partial\phi}{\partial t}\right)_P = \frac{\phi_P^n - \phi_P^0}{\Delta t} \tag{4.35}$$

$$\int_t^{t+\Delta t} \phi(t)dt = \frac{1}{2}\left(\phi^0 + \phi^n\right)\Delta t \tag{4.36}$$

where, ϕ^n shows the value of ϕ at the current time and, ϕ^0 is the value of ϕ at the previous time step. Hence, the temporal discretisation of equation 4.18 for cell P will be,

$$\frac{\phi_P^n - \phi_P^0}{\Delta t}V_P + \sum_f F\phi_f^n - \sum_f (\Gamma_\phi)_f \boldsymbol{S}.\left(\nabla\phi\right)_f^n = S_c V_P + S_p V_P \phi_P^n \tag{4.37}$$

In the above relation, V_P represents the volume of the cell P. As the equation is divided by Δt, this is a first order discretisation. Since the spacial operator and the new temporal coefficient are calculated at the same time step, resolving the variable ϕ requires solving a system of equations. So, it is an implicit scheme and is called Euler Implicit method [59]. As the second order partial derivative, $\frac{\partial^2\phi(t)}{\partial t^2}$, is ignored in equation 4.35, a numerical diffusion term is added to the solution. A remedy for this problem is explained in the next section.

Crank-Nicholson Scheme

A more accurate time discretisation can be achieved by evaluating the transient term as a function of $t - \Delta t$ and $t + \Delta t$ so that,

$$\begin{cases} \phi(t+\Delta t) = \phi(t) + \dfrac{\phi(t)}{\partial t}\Delta t + \dfrac{\partial^2\phi(t)}{\partial t^2}\dfrac{\Delta t^2}{2!} + \dfrac{\partial^3\phi(t)}{\partial t^3}\dfrac{\Delta t^3}{3!} + ... \\ \\ \phi(t-\Delta t) = \phi(t) - \dfrac{\phi(t)}{\partial t}\Delta t + \dfrac{\partial^2\phi(t)}{\partial t^2}\dfrac{\Delta t^2}{2!} - \dfrac{\partial^3\phi(t)}{\partial t^3}\dfrac{\Delta t^3}{3!} + ... \end{cases} \tag{4.38}$$

By subtracting $\phi(t+\Delta t)$ from $\phi(t-\Delta t)$ in equation 4.38, the first derivative is given as,

$$\frac{\partial\phi(t)}{\partial t} = \frac{\phi(t+t) + \phi(t-\Delta t)}{2\Delta t} + O\left(\Delta t^2\right) \tag{4.39}$$

Consider that the order of accuracy of the derivative is now second order. By substituting equation 4.39 into equation 4.18 yields

$$\begin{aligned} \frac{\phi_P^n - \phi_P^0}{\Delta t}V_P + \frac{1}{2}\sum_f F\phi_f^n - \frac{1}{2}\sum_f (\Gamma_\phi)_f \boldsymbol{S}.\left(\nabla\phi\right)_f^n + \frac{1}{2}\sum_f F\phi_f^0 \\ - \frac{1}{2}\sum_f (\Gamma_\phi)_f \boldsymbol{S}.\left(\nabla\phi\right)_f^0 = S_c V_P + S_p V_P \phi_P^n \end{aligned} \tag{4.40}$$

which is called the Crank-Nicholson method. It is second order accurate in time and has low numerical diffusivity as stated by Jasak [59]. Accordingly, it is selected for the temporal discretisation of this study.

Regarding the stability analysis, the face computed Courant number is defined as,

$$Co = \frac{|\vec{u}_f.\vec{S}_f|}{\vec{d}_{PN}.\vec{S}_f}\Delta t \tag{4.41}$$

To satisfy the Courant-Friedrich-Lewy (CFL) condition, the following condition must be satisfied [54],

$$Co \leq 2 \tag{4.42}$$

The CFL condition is satisfied in this study by having $Co = 0.6$.

4.4 Boundary Conditions

The following describes a brief explanation of the numerical boundary conditions used in this study; the Neumann (fixed gradient), Dirichlet (fixed value) and cyclic boundary condition.

4.4.1 Fixed-Value Boundary Condition

In the Dirichlet or fixed-value boundary condition, the value of the variable ϕ at the face 'b' is ϕ_b. Consequently, it has to be included in the discretisation of the convection and diffusion terms on the boundary faces. To this effect, the convection term is discretised as

$$\int_V \nabla \cdot \left(\vec{u}\phi\right) dV = \sum_f F\phi_f \tag{4.43}$$

for the boundary face 'b' is:

$$F_b\phi_b \tag{4.44}$$

where F_b is the face 'b' flux. Accordingly, the diffusion term is,

$$\int_V \nabla \cdot \left(\Gamma_b \nabla\phi\right) dV = \sum_f \left(\Gamma_\phi\right)_f \boldsymbol{S} \cdot \left(\nabla\phi\right)_f \tag{4.45}$$

So, the face gradient at face b is evaluated from the cell centre value as well as the known face value since $\boldsymbol{S}$ and $\boldsymbol{d}_n$ are parallel [59]:

$$\boldsymbol{S} \cdot \left(\nabla\phi\right)_b = |\boldsymbol{S}| \frac{\phi_b - \phi_P}{|\boldsymbol{d}_n|} \tag{4.46}$$

where $\boldsymbol{d}_n$ is the perpendicular distance of point P to the face b.

Near-Wall Treatment

The turbulent flow features near wall is very inhomogeneous, unsteady and non linear. Looking at the mean velocity profile in fully developed turbulent channel flow, (for example, figure 6.9), the high velocity gradient in this area from viscous flow domination is evident. So, the models used for modelling turbulence in free-stream often cannot be applied for near wall treatment.

In this study no wall treatment is chosen since no slip boundary condition is imposed on the walls. The resolution is estimated based on the value of y^+ as,

$$y^+ = \frac{yu_\tau}{\nu} \tag{4.47}$$

Here, u_τ is the friction velocity and is defined as,

$$u_\tau = \sqrt{\frac{\tau}{\rho}} \tag{4.48}$$

where u_τ is the wall shear stress.

4.4.2 Fixed-Gradient Boundary Condition

For the Neumann or the fixed-gradient boundary condition the dot product of the gradient and the unit normal vector of the surface at the face b are prescribed as,

$$\left(\frac{\boldsymbol{S}}{|\boldsymbol{S}|}.\nabla\phi\right)_b = g_b \tag{4.49}$$

As a result, the face value of ϕ for the convection term is calculated from the cell centre value and the aforementioned gradient:

$$\phi_b = \phi_P + \boldsymbol{d}_n.\left(\nabla\phi\right)_b = \phi_P + |\boldsymbol{d}_n| g_b \tag{4.50}$$

where $\boldsymbol{d}_n$ is the perpendicular distance of point $\boldsymbol{P}$ to the face b. Accordingly, the diffusion term for the face b is given as,

$$\left(\Gamma_{\phi}\right)_{b}|\boldsymbol{S}|g_{b} \tag{4.51}$$

4.4.3 Cyclic Boundary Condition

The cyclic boundary condition that is also known as periodic boundary condition has the capability to relate two boundary regions as if they are physically connected. Its application can be found in repeated geometries, for example, turbomachineries. The ability to recycle turbulent fluctuations back into the domain makes it an appropriate technique to gain fully-developed turbulent boundary layer flow that exists in a channel. The discretisation at the patch faces, is performed as if the connected element of the slave cell had been rotated so that it is a neighbour to the master cell. Therefore, the patch face is treated as an interior face [60]. More details regarding the fully turbulent flow in channel is given in section 4.6.

4.5 Turbulence Modelling

Turbulent flow happens when there are instabilities in laminar flow due to augmentation of the perturbation of highly non-linear inertial terms. Theory of “Energy cascade" of Kolmogorov is the most trusted theory for turbulence modelling. Based on this theory, turbulent flow is composed of certain number of eddies of different sizes. Each eddy has a certain quantity of energy which is proportional to the size of the eddy. The bigger eddies break up to smaller eddies and transfer energy to them in a chain process, and the smaller eddies do the same until there is not enough energy remaining in the eddies for transferring to a smaller one. This occurs when the molecular viscosity is large enough to overcome the turbulent kinetic energy and generates heat [54].

The Kolmogorov length scale and time scale are defined in equations (4.52)

and (4.53) respectively, referring to the smallest turbulent eddy size and the corresponding time scale.

$$\eta = \left(\frac{\nu^3}{\epsilon}\right)^{\frac{1}{4}} \tag{4.52}$$

$$t_\eta = \left(\frac{\nu}{\epsilon}\right)^{\frac{1}{2}} \tag{4.53}$$

where ν is the molecular kinematic viscosity and ϵ is the dissipation rate of turbulent kinetic energy. Moreover, the size of the smallest eddies, (the integral length scale), is proportional to the geometry of the channel and the mean flow Reynold number as following:

$$\frac{\eta}{l} \sim Re_{Mean}^{-3/4} \tag{4.54}$$

where, l is the size of the largest eddies and equals to the half channel height in channel flow.

There are three methods for the computational treatment of turbulent flow: Direct Numerical Simulation (DNS); turbulent viscosity models; and, Large Eddy Simulation (LES).

For solving all the scales of the motion in the Navier-Stokes equations, DNS method is used. Therefore, based on the energy cascade theory the computational grid must be as small as the smallest eddies (equation 4.52) which is a too small magnitude. Consequently, a very small time scale must be used to enforce the Courant number to be less than 1 to resolve the whole temporal and spatial turbulent scales. Hence, the computational cost is excessive.

Another approach is using the statistical averaging of the Navier-Stokes equations and modelling all scales of the turbulent motion which is done in turbulent viscosity models. For this end, the flow variables are decomposed into the mean values and the fluctuations (equation 4.55).

$$\Phi(x,t) = \overline{\Phi}(x,t) + \Phi'(x,t) \tag{4.55}$$

where $\overline{\Phi}(x,t)$ is the mean value of the variable $\Phi(x,t)$ and $\Phi'(x,t)$ is the fluctuation.

The averaging is carried out after substituting the two-component variables in the Navier-Stokes equations. Evidently, as all scales of the turbulent motion is modelled, the mesh size is not as small as the DNS. One of the very popular averaging method is the time-averaging which is as following:

$$\overline{\Phi}(x) = \lim_{T\to\infty} \frac{1}{T} \int_{t}^{t+T} \Phi(x,t)dt$$

$\overline{\Phi}(x)$ represents the average of a variable during the time, and is useful for steady state turbulent flow. The Reynolds Average-Navier-Stokes equations (RANS) is produced by the ensemble averaging:

$$\frac{\partial \overrightarrow{U}}{\partial t} + \overrightarrow{\nabla}.(\overrightarrow{U}\overrightarrow{U}) = -\frac{1}{\rho}\nabla P + \overrightarrow{\nabla}.[\nu(\nabla\overrightarrow{U} + (\nabla\overrightarrow{U})^T)] - \frac{1}{\rho}\nabla.\tau \tag{4.57}$$

where upper-case indicates average quantities and τ is the Reynolds stress tensor which describes turbulent fluctuations [61].

On the other hand, for more accurate turbulent computation and less computationally expensive, large eddy simulation is suitable. The LES method is able to resolve explicitly the larger three-dimensional unsteady turbulent motions and model the very small eddies. As a result, the scales of turbulence with more proportion of energy which depend on the geometry, are computed and the small eddies which are universal and independent of the geometry are modelled. As smaller scales of turbulence behave more like isotropic, the error of modelling is small [54].

Turbulent simulation in this thesis were performed using LES code of OpenFOAM to solve the incompressible Navier-Stokes equations.

The main concept of the LES is based on filtering the Navier-Stokes equations in order to retain big scales of motion and abandon the smaller ones [54]. For instance, the variable v is filtered in equation 4.58 so that the scales less than the size Δ are filtered and the scales bigger than Δ are kept.

$$\langle v(x,t)\rangle = \int\int\int F(x,x' : \Delta)v(x,t)d^3\lambda \tag{4.58}$$

where function $F(x,x' : \Delta)$, the filter kernel, is a function that is zero when x and x' are far apart [61].

Various filters are available for LES modelling including the Gaussian filter, the top-hat filter or box filter, the sharp spectral filter, Cauchy filter and Pao filter [62].

The commonly used filter with finite volume discretisation method is the top-hat filter. The function of the top-hat filter is averaging over a rectangular volume Δ^3. So, in real space it is defined as,

$$F(x) = \begin{cases} \frac{1}{\Delta^3}, & |x-\lambda| \leqslant \Delta/2 \\ 0, & \text{otherwise} \end{cases} \tag{4.59}$$

In the above relation, λ is the integral variable of equation 4.58. The filter width, Δ, is the grid spacing and a common choice is

$$\Delta = \sqrt[3]{\Delta x \Delta y \Delta z} \tag{4.60}$$

By choosing the value for Δ there is no need for explicitly filtering during computational process and filtration is made into the discretisation method. This is the approach used in the current study.

In the next step, the governing equations based on the filtered velocity are derived from the Navier-Stokes equations. The equations are similar to the normal continuity and momentum equation with an additional term for the residual stress tensor.

$$\frac{\partial u_i}{\partial x_i} = 0 \tag{4.61}$$

$$\frac{\partial \bar{u}_i}{\partial t} + \frac{(\partial \bar{u}_i \bar{u}_j)}{\partial x_j} = -\frac{1}{\rho}\frac{\partial \bar{p}}{\partial x_i} + \nu \frac{\partial}{\partial x_j}\left(\frac{\partial \bar{u}_i}{\partial x_j} + \frac{\partial \bar{u}_j}{\partial x_j}\right) - \frac{\partial \tau_{ij}}{\partial x_j} \tag{4.62}$$

4.5.1 Sub-grid scale modelling

A model for the residual stress tensor is needed to close the equations 4.61 and 4.62. The principle task of the sub-grid scale modelling is to represent the effects of unresolved small scale fluid motions in the filtered Navier-Stokes equations as closely as possible to the exact stress tensor. Different types of sub-grid scale modelling exist and most of them are based on an eddy-viscosity assumption to model the sub-grid scale tensor [63]. In the eddy-viscosity models, the eddy-viscosity relationship is assumed to be linear owing to the analogy with molecular degrees of freedom, that is known as the Boussinesq assumption. By replacing the molecular viscosity with a turbulent kinematic viscosity, ν_t, the fluid model would be,

$$\tau_{ij} - \frac{1}{3}\tau_{kk}\delta_{ij} = 2\nu_t \bar{S}_{ij} \tag{4.63}$$

where,

$$\bar{S}_{ij} = \frac{1}{2}\left(\frac{\partial \bar{u}_i}{\partial x_j} + \frac{\partial \bar{u}_j}{\partial x_i}\right) \tag{4.64}$$

In equation 4.63 only the turbulent viscosity must be modelled.

Different models are proposed for ν_t, such as, Smagorinsky [64], dynamic Smagorinsky [65], Filtered Smagorinsky [66], and WALE model [63].

The first presented method for sub-grid modelling is Smagorinsky model. The model assumed that the small scale motions are in equilibrium and dissipate quickly. As non-equilibrium conditions happen in free shear layers such as channel flow, Samgorinsky assumption is no longer acceptable.

Contrary to the Smagorinsky, one-equation model of OpenFOAM adds the history effect for kinetic energy and solves a transport equation [61].

$$\frac{\partial K}{\partial t} + \nabla.(K\bar{u}) = \nabla.[(\nu + \nu_{SGS})\nabla K] - \epsilon - \tau : \bar{S} \tag{4.65}$$

Here, ν_{SGS}, the sub-grid scale eddy-viscosity and ϵ, the dissipation rate are defined as:

$$\nu_{SGS} = C_k K^{1/2} \Delta \tag{4.66}$$

$$\epsilon = C_\epsilon K^{3/2} / \Delta \tag{4.67}$$

It is shown that one-equation model is excellent for channel flows [67]. Therefore, this model is used for the current research.

4.6 Turbulence Generation

Numerical turbulent flow generation has been a challenge as it requires time-dependent turbulent inflow condition at the inlet boundary while down stream flow is mostly highly dependent to up stream condition. On the other side, the inlet boundary condition comply with Navier-Stokes equation which makes the problem hard and as a result detailed simulation is costly. Hence, some levels of

approximation is inevitable. Many attempts have been done in order to create numerical turbulent inlet flow that some of them are discussed in brief in this section.

A straightforward method that can be used is the addition of some random perturbation into a laminar flow and let it to develop naturally to a turbulent flow. Although, it seems easy but the costly process of turning to transition makes it an inefficient approach that is not suggested [68].

Secondly, to avoid the costly process of simulation of transition flow, the inlet mapping method is proposed in which an inflow boundary placed a short distance upstream of the real inlet. By providing accurate inflow condition at this boundary a turbulent boundary layer is achieved. However, in real condition this does not usually happen due to a long distance requirement between the upstream face and inlet, which in turn increases the cost of simulation.

Another approach is called random perturbation. In this method by superposing random perturbation on mean velocity field and simulating during the time the perturbation amplifies over downstream flow. Whereas, synthetic turbulent fluctuations are easily generated, to have a fully developed flow a long development section is required otherwise the turbulent effects would be damped out.

Synchronised method is another way to produce turbulent flow by extracting velocity field from a fixed plane in stream wise direction in the domain into inlet. This method is more accurate than random perturbation.

However, a very efficient technique for producing fully developed turbulent flow that is used in the current study is using periodic boundary conditions in streamwise and spanwise directions and symmetry condition for the direction normal to these two directions. The periodic boundary condition must be accompanied with a source term in the momentum equation to maintain a fully developed turbulent flow. The source term applies an additional volume term in the momentum equation and adds the fluctuating arbitrary velocity filed. This method is

proposed by Spalart [69].

4.7 Spurious Currents

The Continuum Surface Force (CSF) method has been developed to model the flow containing interfaces and are influenced by surface tension. Despite all the success in CFD methods, the existence of parasitic currents, brings some limitation of application to this method. Parasitic currents are non-physical flows appearing near the interface and stem from numerical approximations. Inasmuch as the discrete approximation of the interface behaves like a perturbation in the flow domain near the interface, spurious capillary flow is generated in this area. The curvature computation error as well as the force imbalance are the origins of the perturbation. It is found that the capillary flow velocity is proportional to the size of the perturbations [70].

$$C_{\Delta x} \sim \sqrt{\frac{\sigma}{\rho \Delta x}} \tag{4.68}$$

where Δx is the grid size. Noticeably, decreasing the size of the grid augments the problem. In this regard, precise calculation of the interface curvature (equation 4.4) coupled with accurate computation of the discrete balance between pressure gradient and surface tension (equation 4.6) will reduce the currents. Consistently, two types of time step limitations must be applied to avoid the spurious currents:

Firstly, for numerical stability of the temporal-discretized forms of the Navier-Stokes equations as well as the transport equation (equation 4.7), because of the existence of the convective terms, CFL condition must be obeyed [71]:

$$\Delta t < c_0 \sqrt{\frac{\rho \Delta x^3}{\sigma}} = \tau_\rho \tag{4.69}$$

where c_0 is a constant related to the discretisation scheme of the transport equation.

Secondly, to minimise the effect of the perturbation, the time step must be small enough to keep the displacement of the interface smaller than the δ of perturbation (figure 4.1). So that the following condition has to be satisfied:

$$\Delta t < \frac{\mu \Delta x}{\sigma} = \tau_{\mu} \tag{4.70}$$

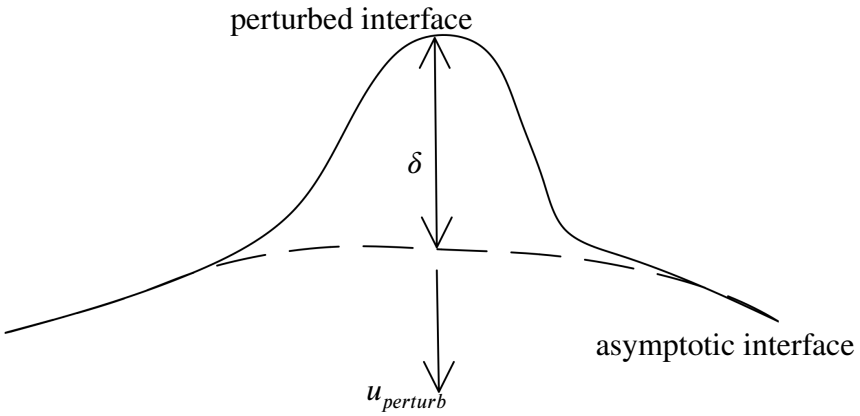

Figure 4.1: A perturbed interface of an ampliture δ and the perturbation velocity $u_{perturb}$ [71]

Consequently, the time step has to meet equation 4.71 [70] that is considered in this investigation.

$$\Delta t \leqslant max(10\tau_{\mu}, 0.1\tau_{\rho}) \tag{4.71}$$

4.8 OpenFOAM CFD Code Solvers

OpenFoam stands for Open Source Field Operation And Manipulation. It is an open source CFD software developed in C++ environment and has the capability of programming solvers as well as benefiting from customised pre-processing and post-processing utilities. Each solver is designed to solve a specific problem in computational continuum mechanics. For instance, there are separate solvers for incompressible flow, compressible flow, multiphase flow, heat transfer and particle tracking flows. One of the multiphase flow solvers is interFoam that is a solver for 2 incompressible isothermal immiscible fluids based on the VOF method and, another one is interMixingFoam that is a solver for 3 incompressible isothermal fluids, two of which are miscible using the VOF method.

4.8.1 interFoam

The built-in solver interFoam is a two-phase formulation volume of fluid method using interface capturing approach in OpenFOAM. In this model, in addition to Navier-Stokes equation a transport equation of the phase fraction for each of the phases is computed in order to have a sharp interface. Therefore, the transport equation phases are [50]

$$\frac{\partial \alpha}{\partial t} + \overrightarrow{\nabla}.(\vec{u}_l \alpha) = 0 \tag{4.72}$$

$$\frac{\partial (1-\alpha)}{\partial t} + \overrightarrow{\nabla}.[\vec{u}_g (1-\alpha)] = 0 \tag{4.73}$$

where in a liquid-gas mixture, α is the volumetric phase fraction of the liquid, $\overrightarrow{u_g}$ and $\overrightarrow{u_l}$ are the velocity of the gas phase and the liquid phase, respectively. By using the VOF assumption about weighted average of properties, the effective velocity can be expressed as

$$\vec{u} = \alpha\overrightarrow{u_l} + (1-\alpha)\overrightarrow{u_g} \tag{4.74}$$

By defining the relative velocity as

$$\overrightarrow{u_r} = \overrightarrow{u_l} - \overrightarrow{u_g} \tag{4.75}$$

equation 4.72 can be rearranged to equation 4.76.

$$\frac{\partial\alpha}{\partial t} + \overrightarrow{\nabla}.(\vec{u}\alpha) + \overrightarrow{\nabla}.[\vec{u}_r\alpha(1-\alpha)] = 0 \tag{4.76}$$

The term $\overrightarrow{\nabla}.[\vec{u}_r\alpha(1-\alpha)]$ on the liquid phase transport equation is an additional term referred to as the compression term [50] which makes the interface sharper and acts just on the interface region and it is zero far from the interface where α has the magnitude of zero or one. Numerical diffusion due to discretisation of convective terms can be reduced by means of the compression term.

All properties of the mixture such as density and viscosity are assumed to be the volumetric average of phases, for instance,

$$\rho = \rho_l\alpha_l + \rho_g\alpha_g \tag{4.77}$$

The momentum equation (4.7), pressure coupling equation (4.13) as well as the transport equation (4.76) are solved to find the velocity, pressure and the volume fraction of the liquid. As $\alpha_l + \alpha_g = 1$, there is no need to solve a separate transport equation for α_g.

4.8.2 interMixingFoam

interMixingFoam is a built-in solver for a mixture of three incompressible fluids, two of which are miscible. This solver is derived from interFoam and uses the

same momentum and pressure equations as interFoam. The transport equations are derived from the third equation in 4.7.

Despite there are three phases in the current study, only two transport equations must be solved. Using the fourth equation in 4.7, the third phase volume fraction is calculated. Assuming that α_1 is immiscible and α_2 and α_3 are miscible, the transport equations for α_1 and α_2 are given as

$$\frac{\partial \alpha_1}{\partial t} + \overrightarrow{\nabla}.(\vec{u}\alpha_1) + \overrightarrow{\nabla}.(\vec{u}_c\alpha_1) = 0 \tag{4.78}$$

$$\frac{\partial \alpha_2}{\partial t} + \overrightarrow{\nabla}.(\vec{u}\alpha_2) - D\nabla^2\alpha_2 + \overrightarrow{\nabla}.(\vec{u}_c\alpha_2) = 0 \tag{4.79}$$

where $\vec{u}_c$ and D are the compression terms at the interface and diffusion coefficient, respectively. Details regarding the diffusion coefficient is provided in section 4.9.4.

4.9 interMixingHeatFoam

interMixingHeatFoam is a solver originated from interMixingFoam developed for the purpose of the current research with the capability to model evaporation process and heat transfer. The code is capable of solving three phases: liquid, vapour and gas simultaneously. The special feature of the code is in considering the volume change effect during evaporation and accommodating the added volume in the continuity equation.

4.9.1 Momentum Equation in interMixingHeatFoam

The momentum equation is similar to interFoam, the second equation 4.7, with an additional momentum source term to produce turbulent flow as it is discussed in section 4.5. Hence, the momentum equation used is,

$$\frac{\partial}{\partial t}(\rho_m \vec{u}) + \nabla.(\rho_m \vec{u} \otimes \vec{u}) = -\vec{\nabla} p_{rgh} + \vec{\nabla}.[\mu_m(\nabla\vec{u} + \nabla\vec{u}^T)] - \vec{x}\vec{g}\vec{\nabla}\rho_m + \sigma\kappa\vec{\nabla}\alpha_l \tag{4.80}$$

The last term in the right-hand side of equation 4.80, is the surface tension force. As the liquid phase is assumed to be immiscible and vapour miscible into the gas, the sole phase that has surface tension is the liquid phase. So, the surface tension force that is defined in equation 4.3 has been modified to equation 4.81 to include the effect of the liquid surface tension into account.

$$\vec{F}_\sigma = \sigma\kappa\vec{\nabla}\alpha_l \tag{4.81}$$

where α_l is the liquid phase fraction. ρ_m and μ_m are the volumetric average of the density and viscosity of phases, respectively. Therefore, for the density it would be expressed as

$$\rho_m = \rho_l\alpha_l + \rho_v\alpha_v + \rho_g\alpha_g \tag{4.82}$$

To enable turbulence generation, ***meanVelocityForce*** in fvOptions was enabled. This utility calculates a momentum source so that a desired mean velocity all over the domain be applied. Hence, the turbulent flow with specified ***Re*** after long enough time of simulation, will be generated.

4.9.2 Pressure Equation in interMixingHeatFoam

Pressure equation is the same equation as interFoam which is described in section 4.2.2.

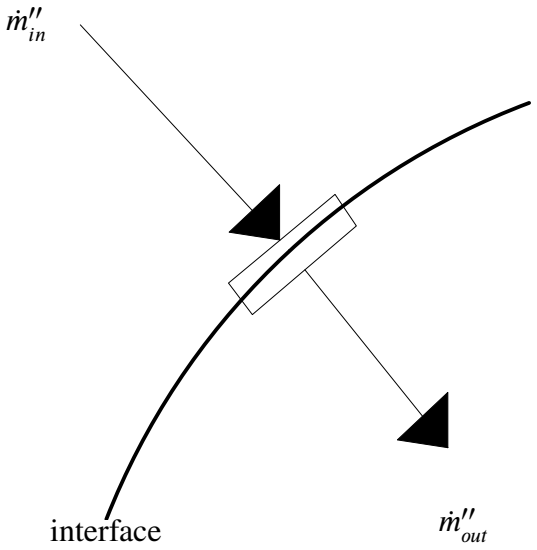

Figure 4.2: Schematic of the droplet-vapour interface control volume

4.9.3 Interface Jump Condition

As stated in section 4.2 based on the VOF method there is one field formula for the velocity, i.e., the velocity field is assumed to be continuous in the whole domain. On the other hand, due to the process of phase change which happens during evaporation, new volume is generated on the interface area which must be numerically accommodated as a source term. In this regard, an innovative solution is proposed based on the work of Ma et al. [72]. Different velocities at the interface are defined whereas the velocity of each phase on the interface is assumed to be equal to the average velocity of the phase in the control volume and they are derived from the mass continuity equation at the interface. Figure 4.2 shows the mass continuity criteria used for equation 4.84.

So as,

$$\dot{m}''_{in} = \dot{m}''_{out} = \dot{m}'' \tag{4.83}$$

Therefore,

$$\rho_l(v_{int} - v_d) = \rho_{gp}(v_c - v_{int}) = \dot{m}'' \tag{4.84}$$

Where $\vec{v}_{int}$ represents the interface velocity and $\dot{m}''$ is the mass transfer flux. Therefore, the relative velocity of phases on the interface, is defined as,

$$\vec{v}_{rel} = \overline{\vec{v}}_d - \overline{\vec{v}}_c = -\dot{m}''[\![\frac{1}{\rho}]\!]\vec{n}_\Sigma \tag{4.85}$$

Where the symbol $[\![]\!]$ around a property depicts the variation of the property at both sides of the interface. By defining the dispersed phase as the liquid phase in the evaporation phenomena, $\overline{\vec{v}_d}$ is the average velocity of the dispersed phase. Here, liquid phase is the dispersed phase and the gas and vapour are regarded as the continuous phase. ρ_{gp} is the density of the gas phase or continuous phase and defined in equation 4.100 and $\overline{\vec{v}_c}$ is the average velocity of the continuous phase. It is assumed that the vapour phase has no relative velocity to the ambient gas. Finally, $\vec{n}_\Sigma$ is the interface normal vector and is defined as

$$\vec{n}_\Sigma = \frac{\overrightarrow{\nabla}\alpha_l}{|\overrightarrow{\nabla}\alpha_l|} \tag{4.86}$$

The volume averaged velocity can be defined as,

$$\vec{u} = \alpha_d\overline{\vec{v}_d} + (1 - \alpha_d)\overline{\vec{v}_c} \tag{4.87}$$

Where $\alpha_d = \alpha_l$ and the term $1 - \alpha_d = \alpha_v + \alpha_g$. The mass averaged velocity would be as following:

$$\vec{v}_m = \frac{\alpha_d\rho_d\overline{\vec{v}}_d + (1 - \alpha_d)\rho_c\overline{\vec{v}_c}}{\rho_m} \tag{4.88}$$

Therefore, the velocity of each phase can be expressed explicitly by $\vec{u}$ and $\vec{v}_{rel}$ as

$$\overline{\vec{v}_d} = \vec{u} + (1 - \alpha_d)\vec{v}_{rel} \tag{4.89}$$

and

$$\overline{\vec{v}_c} = \vec{u} - \alpha_d \vec{v}_{rel} \tag{4.90}$$

Then, the mass averaged velocity can be obtained.

$$\vec{v}_m = \vec{u} + [\![\rho]\!] \frac{\alpha_d(1 - \alpha_d)}{\rho} \vec{v}_{rel} \tag{4.91}$$

Regarding the fact that the velocity field calculated in the momentum equation by means of the VOF method, is the mass averaged velocity [72, 73], $\vec{v}_m$ can be obtained from the momentum equation 4.80. Then, $\vec{v}_{rel}$ can be obtained from equation 4.85. Consequently, the dispersed and the continuous velocity, $\overline{\vec{v}_d}$ and $\overline{\vec{v}_c}$, are derived from equations 4.89 and 4.90, respectively.

These different velocities are used in the transport equations, 4.92 and 4.93, only and the one field formula for the momentum equation is still applicable.

4.9.4 Transport Equation in interMixingHeatFoam

The transport equations originated from the third equation in 4.7, and accommodated to include the source term to account for the mass transfer during the evaporation process.

Despite there are three phases in the current study, only two transport equations must be solved. Using the forth equation of equations 4.7, the third phase volume fraction will be calculated. Knowing that α_l is immiscible and α_v and α_g are miscible, the transport equations for α_l and α_v are given as

$$\frac{\partial \alpha_l}{\partial t} + \vec{v}_d \overline{\nabla} \alpha_l = \frac{\dot{m}'''}{\rho_l} \tag{4.92}$$

$$\frac{\partial \alpha_v}{\partial t} + \vec{v}_c.\vec{\nabla}\alpha_v = -\frac{\dot{m}'''}{\rho_v} - \vec{\nabla}.(D\vec{\nabla}\alpha_v) \tag{4.93}$$

Where, $\dot{m}'''$ is the mass source term and is generated at the interface during phase change. It is obtained from the following

$$\dot{m}''' = |\nabla \alpha_l| \dot{m}'' \tag{4.94}$$

Next, gas phase volume fraction can be obtained.

$$\alpha_g = 1 - \alpha_l - \alpha_v \tag{4.95}$$

Relation of the volume specific mass flux is given in equation 4.104.

The second term in the right hand side of equation 4.93 represents the diffusion process of the vapour into the ambient gas as it assumed to be miscible into the ambient gas. Though, the liquid is not soluble in the gas. Consequently, no diffusion term is included in the liquid transfer equation. D in 4.93 is the diffusion coefficient and is defined from the following equation [74]:

$$D = \frac{10^{-7} T_g^{1.75} \sqrt{\frac{1}{\hat{M}_g} + \frac{1}{\hat{M}_v}}}{p_g (v_{diff,g}^{1/3} + v_{diff,v}^{1/3})^2} \tag{4.96}$$

Where $v_{diff,v}$ and $v_{diff,g}$ as well as $\hat{M}_v$ and $\hat{M}_g$ are the atomic diffusion volume of the vapour and the gas, and the molar weight of the vapour and the gas, respectively. T_g and p_g are the temperature(K) and pressure(atm). The diffusion coefficient is assumed to be constant in the simulation and its value is calculated based on the average temperature.

Similar to interMixingFoam, equation 4.95 is applied between the phases, since there is no need to solve a separate transport equation for all three phases. However, the magnitude of the vapour and liquid volume fraction during the evaporation process change more than the gas phase. For example for a case that there is no

vapour at the beginning of the evaporation process and there are only pure liquid in ambient gas, α_l in cells containing the drop, changes from 1 at the start to 0 at the end of evaporation where no liquid left. Simultaneously, the α_v in cells around the drop alters from 0 to 1. On the other hand, due to the fact that gas phase occupied more space, the magnitude of α_g is nearly one in most of the cells. Therefore, it is crucial to calculate the transport equations of liquid and vapour phases separately and the gas phase will be given from equation 4.95.

4.9.5 Mass Transfer in interMixingHeatFoam

Evaporation process is the motion of the vapour from the surface of the liquid into the surrounding gas which is different from the vaporisation that is the process of vapour transfer into its pure vapour. Evaporation consists of the diffusive processes that does not appear in vaporisation.

The total mass transfer in a fluid comprises convective mass transfer as well as diffusive mass transfer. While the convective mass transfer process is happening with the bulk motion of the mass, the diffusive mass transfer is caused by concentration gradient because a concentration gradient makes the concentration flux [75]. This relation is firstly introduced with mathematical relation by Adolf Fick in 1855. Fick's first law of the diffusion is given in equation 4.97.

$$N_j = -D_j \nabla c_j \tag{4.97}$$

Where N_j, D_j and c_j are the molar flux of component j, the diffusion coefficient of component j and the concentration, respectively.

For a mixture including species liquid, vapour and gas, by manipulating equation 4.97, the one dimensional diffusional flux of species vapour at the interface of liquid-vapour can be derived.

$$\dot{m}''_{v,diff} = -\rho D \frac{dY_v}{\partial x} \tag{4.98}$$

Where Y_v is the vapour species mass fraction and can be given from the following equation:

$$Y_v = \frac{\rho_v}{\rho_{gp}} \tag{4.99}$$

Where ρ_{gp} is the gas phase density and can be obtained from

$$\rho_{gp} = \frac{\alpha_g \rho_g + \alpha_v \rho_v}{\alpha_g + \alpha_v} \tag{4.100}$$

As the bulk flux of vapour is given by equation 4.101

$$\dot{m}''_{v,bulk} = Y_v \dot{m}'' \tag{4.101}$$

the total flux of species vapour would be obtained in equation 4.102.

$$\dot{m}''_v = Y_v \dot{m}'' - \rho D \frac{dY_v}{\partial x} \tag{4.102}$$

The total mass flux of the system equals to $\dot{m}'' = \dot{m}''_l + \dot{m}''_v$. By assuming that liquid is insoluble in the vapour, $\dot{m}'' = \dot{m}''_v$. So equation 4.102 is in the form of

$$\dot{m}''_v = Y_v \dot{m}''_v - \rho_{gp} D \frac{dY_v}{\partial x} \tag{4.103}$$

Therefore, the mass flux of liquid into gas and vapour in the general form is given:

$$\dot{m}''_v = -\frac{\rho_{gp} D}{1 - Y_v} \nabla Y_v . \vec{n}_\Sigma \tag{4.104}$$

The above relation is used for the mass transfer equation of the evaporation process.

4.9.6 Energy Equation in interMixingHeatFoam

To include the effect of temperature change and the latent heat of evaporation in the energy content of the system, the energy equation is applied as described in section 4.2.4 and re-written in a form to include the temporal and convectional alteration of the density and specific heat.

$$\frac{\partial}{\partial t}(\rho c_p T) + \nabla.(\rho c_p \vec{u} T) = \nabla.(k \nabla T) + T_0 \frac{\rho \partial(\rho c_p)}{\partial t} + T_0 \nabla(\rho c_p \vec{u}) + \dot{q}_v \qquad (4.105)$$

Where the term $\dot{q}_v$ is defined as

$$\dot{q}_v = h_{fg} \dot{m}''' \qquad (4.106)$$

Here, h_{fg} is the latent heat of evaporation of the liquid and T_0 is the reference temperature for the latent heat.

4.9.7 intermixingHeatFoam Algorithm

The algorithm for the interMixingHeatFoam solver is outlined in figure 4.3.

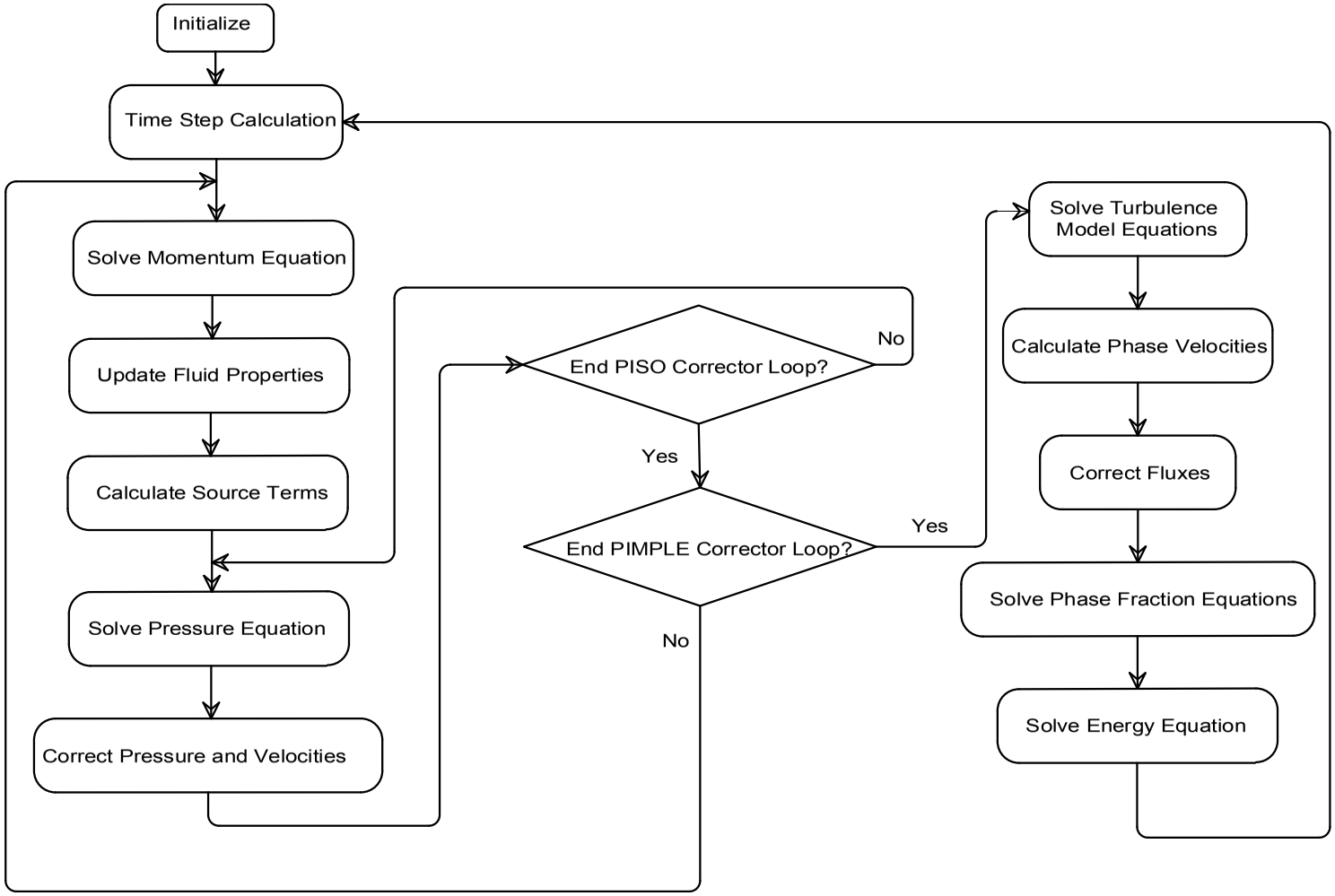

Figure 4.3: Schematic of the algorithm used in interMixingHeatFoam

4.10 Summary

In this chapter, detailed computational strategies used for the results presented in the following chapters are presented. The basic idea of the VOF method, the governing equations, the discretisation schemes, the mathematical formulation of the boundary conditions, turbulence modelling as well as the turbulence generation method employed in this study are discussed in detail. The OpenFOAM built-in solver interFoam which is the basis for the developed code is described followed by inteMixingFoam solver description. The special features of the developed code, interMixingHeatFoam, for the purpose of simulation of evaporation is explained. The innovation of the code and the necessity for the development of a new code with the aforementioned capabilities are explained. Finally, all the features and algorithms deployed to develop a code in order to model a three phase evaporation model are explained.

Chapter 5

EXPERIMENTAL SETUP

5.1 Introduction

The experimental part of the thesis is performed to validate the results of the developed numerical code, interMixingHeatFoam. In this chapter the experimental set-up used for droplet investigation is discussed. First of all, the air flow system and design criteria are described. Next, the air flow characteristic is described. The specifications of various components used for the design of the system are explained in detail. The imaging system and calibration process is explained. Then, the experimental parameters and procedure are detailed. Afterwards, the fluid properties used for the experiments are explained. Finally, the uncertainty of the measurements are described.

5.2 Air Flow System

A continuous jet method has been chosen for studying the droplet behaviour. The test rig is designed to produce fully developed turbulent air flow. To this end, a long enough channel is designed. Figure 5.1 shows the schematic of the air flow

system. Compressed air is supplied from the central air facility of the laboratory. It proceeds to an air filter for cleaning purpose and flows through a pressure regulator. The air then passes through a mist separator. Next, the clean dry air is stored in a 150 litre air tank until specified amount of pressure is achieved. The air tank provides a continuous and stable supply of pressurised air for the experiments. The design pressure and temperature of the air tank are 1100 kPa and $120°C$, respectively. After that, pressurised clean air up to 10 bar is delivered to the air channel via a control valve and a ball valve. The control valve is used for air pressure regulation. A honeycomb straightener plate is located inside the channel to smooth the flow into the whole cross section of the channel. The droplet is released into the second last part of the channel where the fully developed flow has been reached. This section is made of transparent polycarbonate to enable image capturing. Finally, air flows out smoothly via a diffuser.

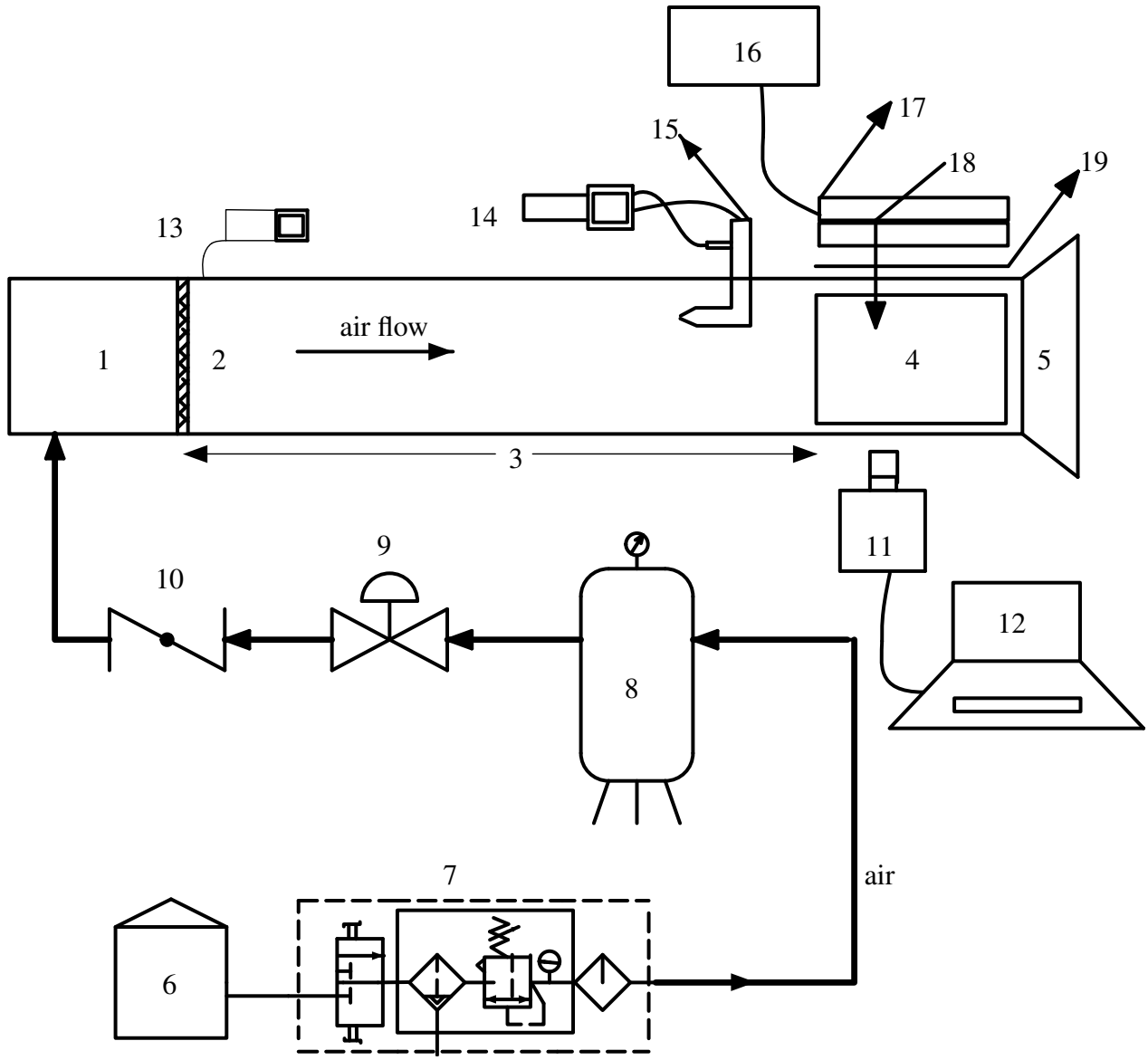

Figure 5.1: Schematic of test rig; (1) Inlet section (2) Honey comb straightener (3) Entry length (4) Viewing window (5) Diffuser of the channel (6) Central air supply (7) Air filter, mist separator and pressure regulator (8) Air tank (9) Control Valve (10) Ball valve (11) High speed camera (12) Laptop (13) Thermometer (14) Anemometer (15) Pitot tube (16) DC power supply (17) LED light (18) Droplet dispenser (19) Light diffuser

Many components have been used in the fabrication of the test rig. Most of these components were purchased, while some of them built in- house to suit the design requirements. Specification of components used in the test rig is provided in Table 5.1.

Table 5.1: Specification of components used in the experimental setup

Component	Make and Model	Specifications
Mist separator	NORGREN®OLYMPIAN F51-008-MOTO	maximum pressure 10 bar and maximum temperature 50°C
Control valve	Parker 51/17	maximum temperature 66°C maximum inlet pressure 21 bar
High speed camera	PHOTRON FASTCAM SA3	frame rate maximum 120,000 fps
Interchangeable lens	DG MACRO SIGMA	24-70 mm
Air receiver	PILOTAIR	design pressure 1100 kPa design temperature 120°C
Air filter and pressure regulator and	NORGREN®OLYMPIAN	maximum pressure 10 bar and maximum temperature 50°C

Table 5.1: Continued...

Component	Make and Model	Specifications
Micromanometer	TSI DP-CALC^{TM} model 5828	-3735 to +3735 Pa
LED light	ALTRONICS	2×36pcs LED, DC 12 V, 4W, Lumen per LED bar: $210LM \pm 5\%$
Droplet dispenser	NEXTY WATSON	$10 \sim 100\mu l$
Pitot tube	DWYER	$1/8''$ diameter and $6''$ insertion length
DC power supply	GWINSTEK	
Thermometer	Lutron LM8000	-100 to 1300 $°C$

Air Channel

The air channel, (including sections 1 to 5 of the schematic diagram in figure 5.1), is designed to provide fully developed turbulent flow in order to study the motion and evaporation of droplet. To this end, it comprises different sections; a connection part that is designed to receive air from the connecting hose and deliver to the honeycomb plate, (section 1 in figure 5.1). The air hose is connected to the

bottom of the connection part. Therefore, the air flow releases from the bottom of the connection and hits to the top. A honeycomb straightener plate is located inside the channel after the connection part, (section 2), to smooth the flow into the whole cross section. After that there is the entry region, (section 3), where the boundary layer grows. Next, the test section is located, (section 4), where the air flow is fully developed. Lastly, a diffuser provided to deliver smooth air flow to the atmosphere.

Entrance Region

The velocity of fluid near the walls at the inlet section of the channel, (section 3 in figure 5.1), is zero for viscous fluids and gradually increases going further from the wall towards the centre. The boundary layer span expands from each side of the channel going further into the channel until they reach together. This is the point where boundary layer join together and fill the chamber. The flow after this entry length region is fully developed flow as the whole region of the channel has the same flow properties.

The length of the channel is designed to be long enough to maintain fully turbulent flow in the test section, where droplets are released. The criteria for development length required for turbulent entrance region is based on Nikuradse [76] approximation:

$$L_{turb} \approx 40 d_H \tag{5.1}$$

where hydraulic diameter, d_h is used for rectangular channels. This is a long enough length so that a fully developed hydrodynamic boundary layer is achieved.

By choosing a channel with cross section $50\,mm \times 200\,mm$ the corresponding hydrodynamic diameter and the entrance length from the equation 5.1 are calculated. The reasons for choosing the channel dimensions are given in section 6.2.

Table 5.2: Equations used for the design of the air channel

Hydraulic diameter	$d_h = \frac{4A}{P}$
Developed length	$L_{develop} = 40d_h$ (equation 5.1)
Corresponding velocity	$v = \frac{Re\mu}{\rho h}$
Time required for the drop to fall down	$\Delta t = \sqrt{\frac{2h}{g}}$(displacement equation)
Horizontal displacement during falling time	$\Delta x = v\Delta t$
Minimum total length required	$L = L_{develop} + \Delta x$

After the entrance length, where the fully developed flow is achieved, a viewing window is provided, which is made of polycarbonate to enable image capturing process. All other parts are made from medium-density fibreboard (MDF). The length of this section is designed based on the horizontal displacement of the droplet when it falls from the top of the channel. The maximum Reynolds number is considered for calculating the horizontal droplet trajectory.

To facilitate the process of manufacturing and maintenance, the channel is divided into 4 pieces of 1m length as well as a 40 cm length piece before the viewing section. This section is used for velocity measurement purpose.

Diffuser Design

Flow separation of the air, happens when turbulent flow exits to the atmospheric air. In order to prevent separation of the flow from the wall which brings noise and energy loss, a diffuser has been designed, (section 5 in figure 5.1). The diffuser is employed to convert kinetic energy into potential energy smoothly. When the turbulent flow encounters a sudden expanding area, pressure falls to zero quickly and the flow separates from the exit plane. A properly designed diffuser will help the flow to exit the channel smoothly.

As diffuser stall is mostly a function of diffuser geometry [77], the diffuser performance is proportional to the ratio of the length to diameter since momentum exchange can happen gradually. Figure 5.2 shows the schematic of a typical diffuser. As a result, based on pressure discovery pattern of two-dimensional diffusers, the following relationship for a diffuser is defined:

$$\frac{A_2}{A_1} = \frac{W_2}{W_1} \tag{5.2}$$

Where W_1 and W_2 are the widths and A_1 and A_2 are the corresponding areas of the cross section of the two sides of the diffuser.

Hence, for $W_1 = 50\,mm$ and based on Blevins's formula (equation 5.2) [77] by choosing $\frac{N}{W_1}$=3, N, the length of the diffuser would be 150 mm (figure 5.2). To have no appreciable stall, the following criteria has been selected:

$$\frac{A_2}{A_1} - 1 = 0.6 \Rightarrow A_2 = 1.6A_1 = 80\,mm \times 200\,mm$$

A photograph of the laboratory set-up including the camera and the imaging system is shown in 5.3. Detailed fabrication drawings are provided in Appendix.

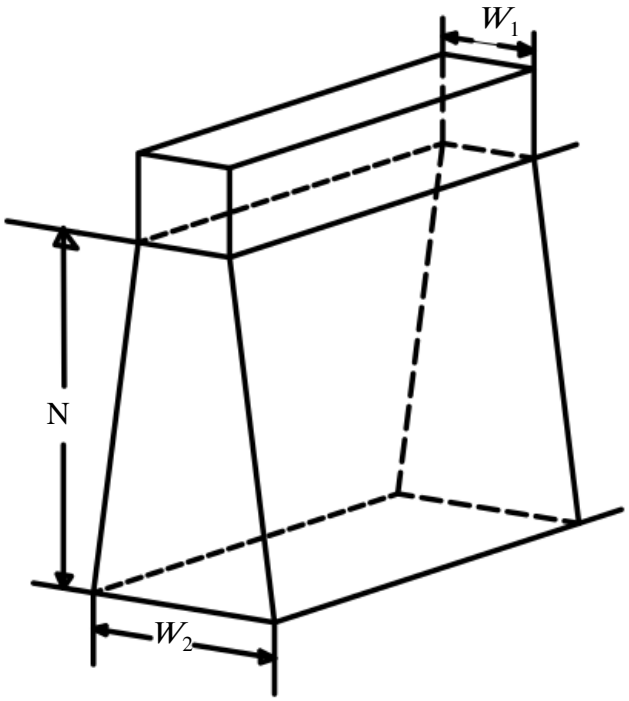

Figure 5.2: Schematic of the diffuser [77]

Figure 5.3: Photograph of the test rig

5.3 Air Flow Characteristics

Flow velocity is measured by means of a Pitot tube placed at locations of the channel cross section to read the static and total pressure of the flow. Cross sectional view of the test section as well as measuring locations are shown in figure 5.4. Pitot tube was connected to a digital manometer to convert the dynamic pressure to the velocity. The manometer is a TSI DP-CALC Micromanometer model 5825. To have higher accuracy, the velocity measurements are done near to the test section. Then, the mean velocity is calculated. The velocity profile for the turbulent flow is obtained and shown in figure 5.5. Large velocity gradient near the walls and

nearly constant velocity further from the walls represent fully-developed turbulent flow conditions in the channel before the test section.

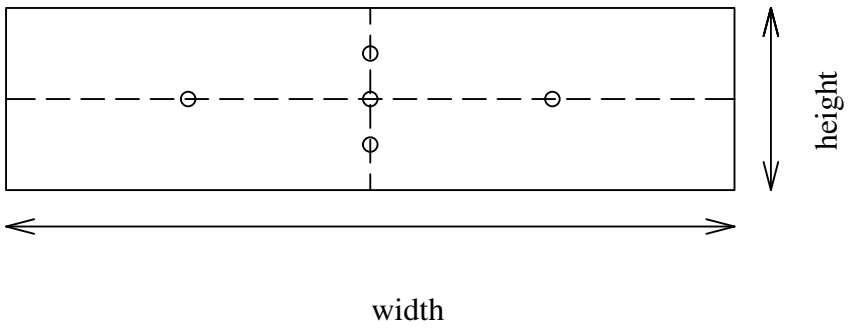

Figure 5.4: Schematic of the test-section and cross sectional view. ∘ represents measuring locations

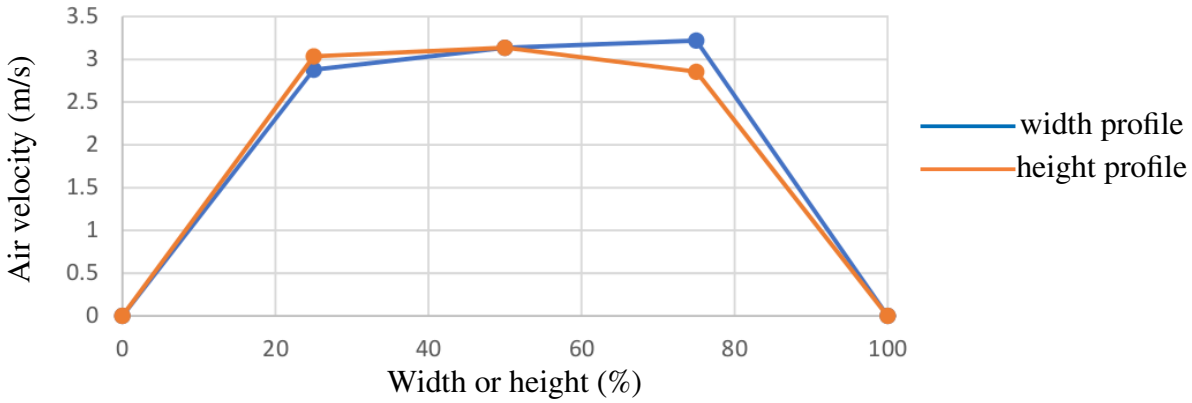

Figure 5.5: Turbulent flow velocity profile along width and height of the channel

5.4 Droplet Dispenser Nozzle

For droplet injection, Watson Nexty-100 micropipette is used (figure 5.6). It has the capability of producing droplets of sizes $10 \sim 100\mu l$. It consists of a volume setting dial and a digital indicator to set the desired size of the drop before injection. In addition, a push button is provided to release the drop. The droplet dispenser is located on the top of the test section filled with the test liquid and can be used for manual injection of the drop when required.

Figure 5.6: Watson Nexty-100 micropipette [78]

5.5 High Speed Imaging System and Calibration

Figure 5.7 shows the imaging system used for capturing images. The system includes a high speed camera capable of capturing images up to 120,000 images per second. To have photos with the required contrast, a suitable focal lens is attached to the digital camera. The camera was placed perpendicular to the air flow direction and focused on the droplets. The illumination was provided by a set of LED lights. The beams of the lights scattered with an acrylic diffusing plate resulted in smooth high intensity light capable of capturing droplet size and motion in air

flow. To have a smooth light during image shooting, DC power supply is provided for LED lights. Using this setup, images of drops were captured at 6000 fps with a capture window time of 1500 sec, successfully taking the trajectory and evaporation of drops. Images were captured by means of the PFV-LabVIEW®program.

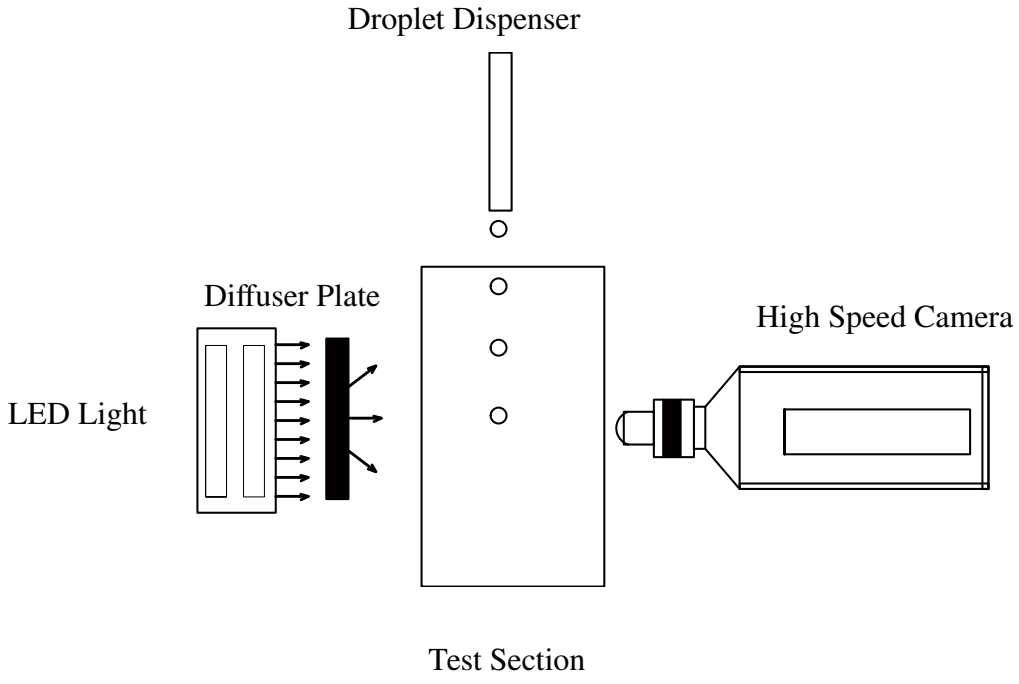

Figure 5.7: High speed imaging system

Clear focus is provided by means of correct placement of the camera position, adjustment of the focal lens and aperture. In addition, in order to increase the quality of measurement and minimising the effects of parallax error, all in-focus droplets are released in the same plane.

To further augment the level of image quality, a calibration key provided in the camera was used whenever any changes in frame rate, resolution and aperture were performed. This resulted in a more accurate determination of sufficient detail in the images.

The calibration was accomplished by measuring a known reference length placed in the same plane as the droplets were released prior to the test. Hence, an accurate determination of the pixels to millimetres conversion was carried out. The diameter of each droplet was measured at a time that the droplet was completely detached from the nozzle and had a nearly spherical shape. This was done by measuring drop diameter from left to right and top to bottom (figure 5.8). The image analysis was performed using Matlab®.

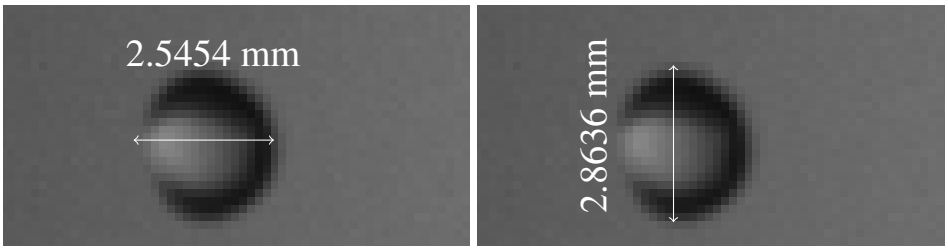

Figure 5.8: Droplet diameter measurement

5.6 Experimental Parameters and Procedure

The experimental parameters for droplet evaporation are given in Table 5.3.

Table 5.3: Parameters for the experimental system

	d_0(mm)	Re_{hyd}	T_{amb} (°C)	$T_{i,d}$(°C)	drop material
standstill	2	0	22	22	water
turbulent flow	2	8900	20	22	water

In order to perform the experiment, a series of procedures were followed: First of all, the air was supplied to the receiver up to a specified pressure. The illumination light connected to the DC power supply was turned on.

Then, the camera was connected to the laptop. Next, the Photron FASTCAM Viewer software on the laptop was activated to record images captured by the camera by selecting the desired frame rate, shutter speed, resolution and trigger mode. The camera was placed perpendicular to the test section and was set to the full capture of the channel height with specified resolution and frame rate. The focal lens was adjusted to focus on the injection device tip clearly.

Then, the droplet dispenser was filled with the liquid. The length of the liquid in the droplet dispenser tip was measured, and used for the purpose of calibration. The air flow was released by opening the control valve. The image capturing software was adjusted to capture images. Air temperature within the channel was recorded at the same time that droplets were released. Finally, the captured images were transferred to the laptop for further analysis.

5.7 Material Properties

For the purpose of this study, atmospheric air is chosen as the fluid medium. The reason for choosing air as the fluid is due to the fact that it is used in most industrial applications in addition to being safe and available freely. Water is chosen for the liquid droplet as it is safe in experimental conditions in the laboratory. The properties of the fluid at atmospheric pressure and $20°C$ are found in Table 5.4.

5.8 Experimental Results

The ambient temperature in figure 5.9 is $22.9°C$ and air flow temperature in figure 5.10 is $20.9°C$. The liquid temperature in both of the figures is $22.9°C$. The Re_{hyd} of the turbulent flow is 16000. The frame rate of all images are 6000 fps.

Table 5.4: Fluid properties at 20°C and atmospheric pressure

	density (ρ) $[kg/m^3]$	surface tension (σ) $[mN/m]$	viscosity (μ) $[Pa.s \times 10^{-5}]$
air [79]	1.205		1.822
water [79]	998.2	72.8	100.2

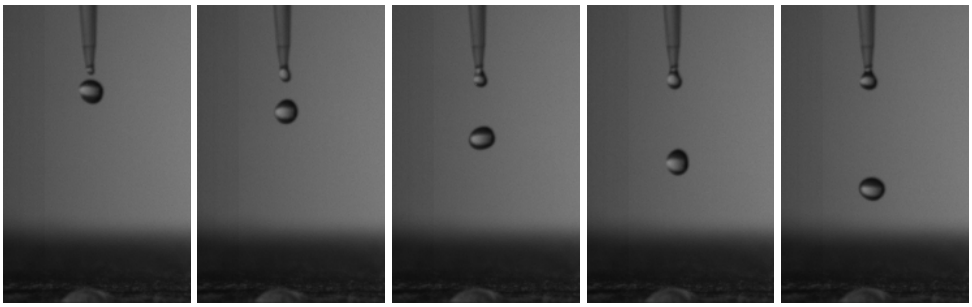

Figure 5.9: Water droplet falling in stand-still air; timing sequence from left to right are 0, 0.01, 0.02, 0.03, 0.04 sec, respectively.

5.9 Experimental Uncertainty

The uncertainty analysis is divided to two sections. In the first section, the uncertainty of measured parameters is presented, and in the second section the uncertainty of calculated parameters based on the first section analysis is considered.

5.9.1 Uncertainty Analysis of Measured Parameters

There are 3 types of measurements in the experiments; the velocity measurement, the drop size quantification and the time interval captured by the camera.

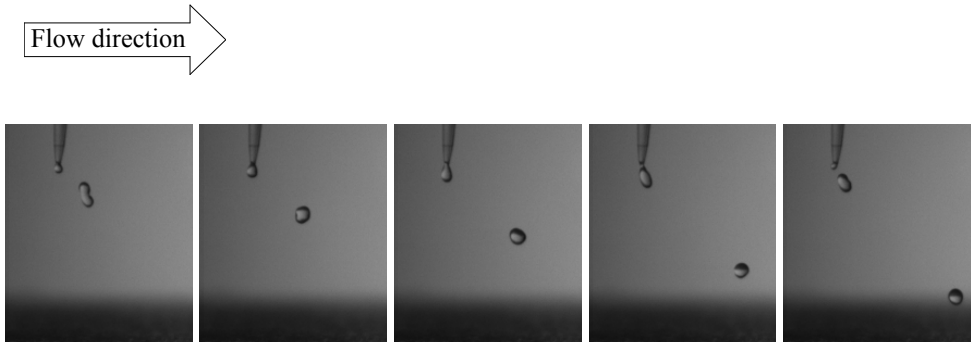

Figure 5.10: Water droplet falling in turbulent air flow with $Re_{hyd} = 16000$; timing sequence from left to right are 0, 0.01, 0.02, 0.03, 0.04 sec, respectively.

Uncertainty Analysis of Air Flow Mean Velocity

The most prominent uncertainty in air velocity originates from the measurement uncertainty. The uncertainty of using Pitot tube for the velocity measurement is $\pm 4.2\%$ based upon the anemometer documentation. Therefore, the uncertainty of the measured velocity would be $\approx 4.2\%$.

Uncertainty Analysis of Droplet Diameter

Uncertainty of drop diameter is assumed to be affected by uncertainty in choosing the droplet edge. In spite of the accurate focus and short capture window, the edge of the drop diameter could only be precisely determined to within ± 1 pixel. Converting pixel to millimetre showed that the uncertainty in the diameter measurement is nearly ± 0.15 mm.

In our investigation droplet diameters ranged around 2.5 mm which gives the typical uncertainty approximately $\pm 6\%$.

Uncertainty Analysis of Time Interval

According to Photron FASTCAM-SA3 hardware manual, the uncertainty in time interval is $\pm 18.5ns$. As the shutter speed of the images is 1/6000 sec, the uncertainty of timing interval is calculated as, 0.0111%.

5.9.2 Uncertainty Analysis of Calculated Values

The uncertainty analysis of the calculated parameters are based on the method proposed by Kline et al.[80]. The uncertainty of the parameter R is obtained from equation 5.3.

$$u_R = \Big[\sum_{i=1}^{n} \Big(\frac{\partial R}{\partial V_i} u_{V_i} \Big)^2 \Big]^{1/2} \tag{5.3}$$

Where u_{V_i}, u_R and n are the uncertainties of the independent variable V_i and the parameter R, and the number of the independent variables, respectively.

Uncertainty Analysis of Reynolds Number

Based on equation 5.3, the uncertainty of Reynolds number, ($Re = \frac{V D_h}{\nu}$), is calculated from equation 5.4.

$$u_{Re} = \Big[\Big(\frac{\partial Re}{\partial V} . \frac{V}{Re} u_V \Big)^2 + \Big(\frac{\partial Re}{\partial D_h} . \frac{D_h}{Re} u_{D_h} \Big)^2 + \Big(\frac{\partial Re}{\partial \nu} . \frac{\nu}{Re} u_\nu \Big)^2 \Big]^{1/2} \tag{5.4}$$

where:

$$\frac{\partial Re}{\partial V} = \frac{D_h}{\nu} \tag{5.5}$$

$$\frac{\partial Re}{\partial D_h} = \frac{V}{\nu} \tag{5.6}$$

$$\frac{\partial Re}{\partial \nu} = -\frac{V D_h}{\nu^2} \tag{5.7}$$

The uncertainty of D_h is from the measurement error which is $\pm$0.5 mm. Since the magnitude of the kinematic viscosity is obtained from tables, the corresponding uncertainty is assumed to be negligible. Therefore, the relative uncertainty of Re is $\pm$4.2%.

Uncertainty Analysis of Evaporation Rate

The uncertainty of evaporation rate, $K = \frac{d_0^2 - d^2}{t_0 - t_1}$, can be obtained from equation 5.8.

$$u_K = \left[\left(\frac{\partial K}{\partial d_0}.\frac{d_0}{K}u_{d0}\right)^2 + \left(\frac{\partial K}{\partial d}.\frac{d}{K}u_d\right)^2 + \left(\frac{\partial K}{\partial t}.\frac{t}{K}u_t\right)^2\right]^{1/2} \tag{5.8}$$

Here:

$$\frac{\partial K}{\partial d_0} = \frac{2d_0}{t} \tag{5.9}$$

$$\frac{\partial K}{\partial d} = -\frac{2d}{t} \tag{5.10}$$

$$\frac{\partial K}{\partial t} = -\frac{d_0^2 - d^2}{t^2} \tag{5.11}$$

By substituting the magnitude of all relative uncertainties, the uncertainty of evaporation rate is calculated as $\pm$1.07%.

5.10 Summary

A detailed description of the experimental system used in the current research was provided. The design criteria of the air flow system, air flow characteristics

and specifications of all components used in the experiment were explained in detail. The imaging system and the calibration procedure were described. Then, the experimental procedure was explained. The captured images were presented. Finally, the uncertainty of the measured and calculated parameters were provided.

Chapter 6

RESULTS AND DISCUSSION

6.1 Introduction

Results of the numerical simulation and experimental studies are presented in this chapter. The chapter will begin with problem description and continued with the mesh study for numerical simulation. Then the model validation is presented. This section comprises two parts; validation of the fully-developed turbulent channel flow with the help of DNS results and, validation of the numerical model and developed code with experimental tests. This is followed by the description of the results of the simulation of droplet in different flow fields. It concludes with a discussion on different evaporation rates in flow field.

6.2 Problem Description

The channel considered for numerical modelling has the same dimensions as the one utilised in the experimental studies. The schematic of the channel, flow direction, inlet and outlet, walls as well as the direction of gravity, g, are given in figure 6.1. The dimensions of the channel are depicted in figure 6.2. In all of the

simulations the channel is filled with air and the droplet is located initially at a point indicated in figure 6.2. It is then allowed to freely fall due to gravity.

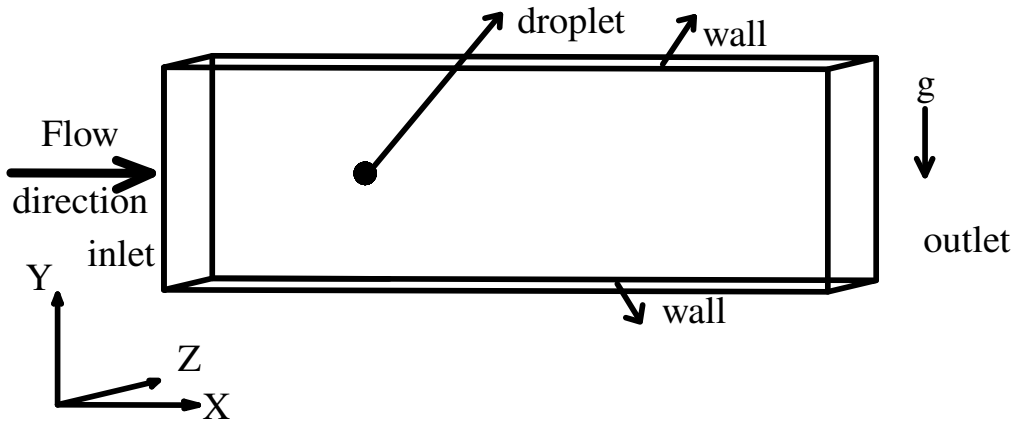

Figure 6.1: Schematic view of computational domain and the droplet

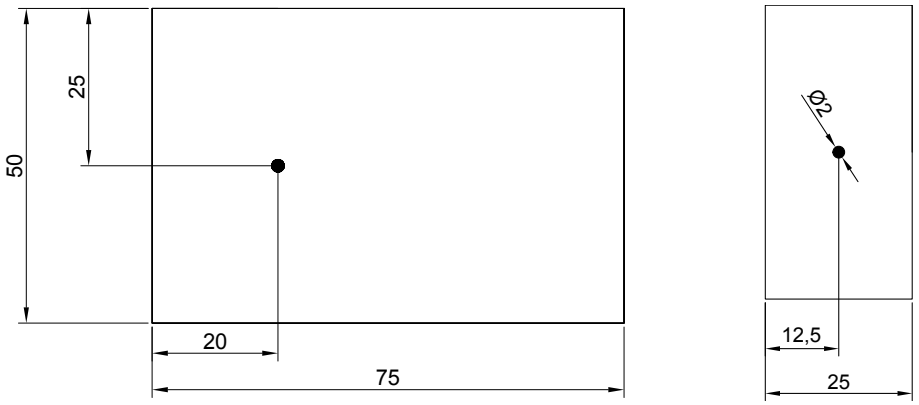

(a) (b)

Figure 6.2: Computational domain and initial location of the droplet (a) X-Y view (b) Y-Z view (dimensions in mm)

The height of the channel is chosen based on the experiments of Daïf et al.

[81] to minimise the effect of geometry on the evaporation process. As the faces on spanwise and streamwise directions have cyclic boundary conditions, coupled faces treat as if there is a one-to-one mapping between them on each side. Therefore, the length and the width of the channel represents an infinitely long (x-axis) and wide (z-axis) domain. No-slip boundary conditions were selected for the walls that are shown in figure 6.3 with hatched surfaces. The rest of the boundaries are cyclic.

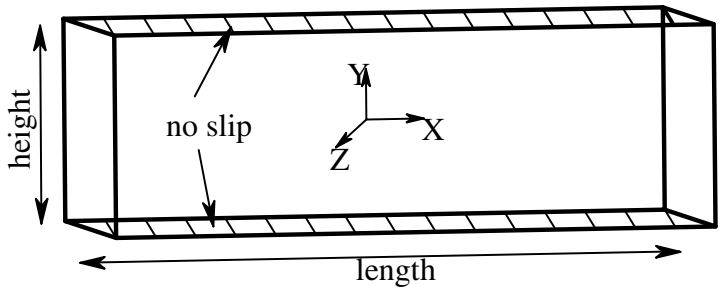

Figure 6.3: Boundary condition for the channel

6.3 Mesh Independent Study

The computational domain consists of two boxes located one on top of the other in the Y direction to enable the use of cyclic boundary condition. Each box is split in three sections in each direction. The part of the domain that the droplet locates and moves has the finest mesh with cells of uniform length and height all over the section. This helps having finer mesh around the droplet where the pressure and velocity gradients are higher. In other parts of the domain, the mesh size increases in X and Z directions further from the droplet. Meanwhile, the cell size near the walls are refined in order to have enough cells to resolve near wall eddies correctly.

The schematic of the computational mesh is presented in figure 6.4.

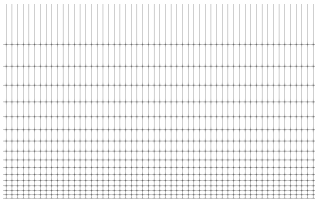

(a) Near-wall refined mesh

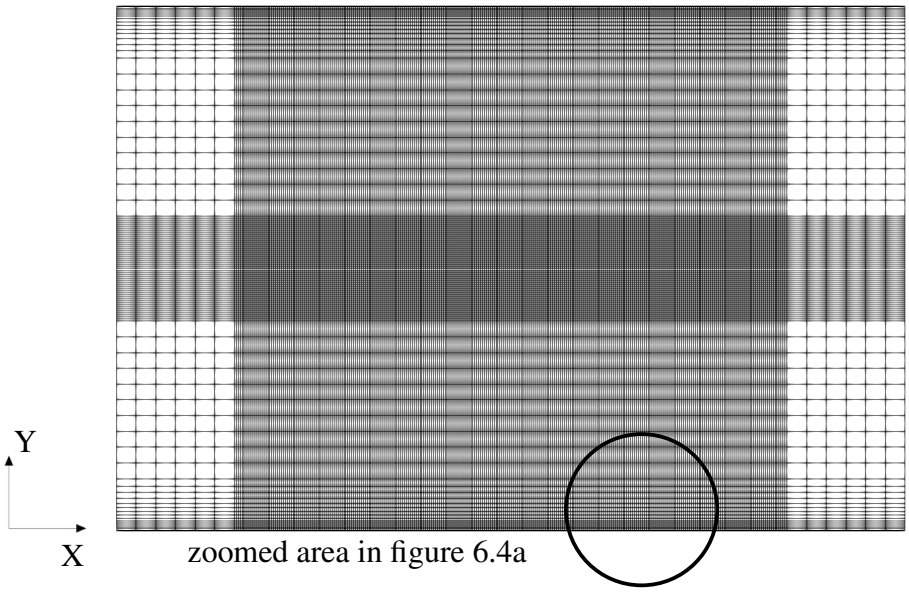

Figure 6.4: Computational domain in X-Y view showing the near wall refinement and cell grading

Four meshes have been studied for mesh dependency investigation to ensure that the solution does not change with grid density. The total number of cells are 1.9 M, 1.6 M, 1.3 M and 0.8 M for the fine, standard, moderate and the coarse cases, respectively with the following parameters: $Re = 16000$; LES turbulent model; channel size 0.075 m $\times$ 0.050 m $\times$ 0.025 m; ambient temperature; and droplet initial temperature 363 K and 343 K, respectively. The ambient pressure is considered 1 atm. The total number of cells and smallest cell size for the solution time of 2 ms of the simulation are listed in Table 6.1. Plots of the volumetric

fraction of water (figure 6.5), volumetric fraction of vapour (figure 6.6) and temperature (figure 6.7) at t=2 ms along the line where the deformation due to the presence of the droplet is large is provided for mesh independent study. It can be seen that 1.6 M cells is satisfactory for the present simulations.

Table 6.1: Meshes used for mesh independence study

Mesh	Number of cells	Smallest cell size [mm]
coarse	0.8 M	0.1714
moderate	1.3 M	0.1442
standard	1.6 M	0.1376
fine	1.9 M	0.1314

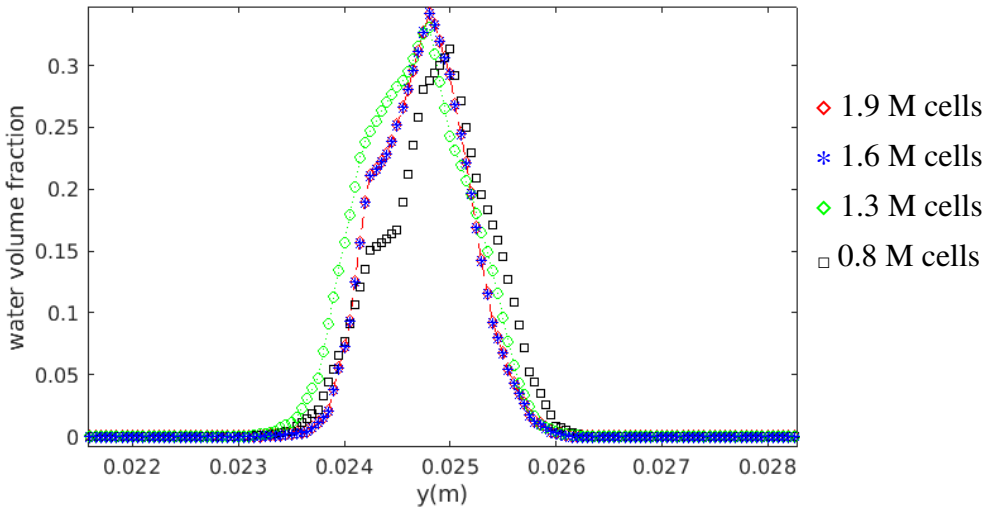

Figure 6.5: Volumetric water fraction for mesh study at ambient temperature 363 K, ambient pressure 1 atm and $Re = 16000$

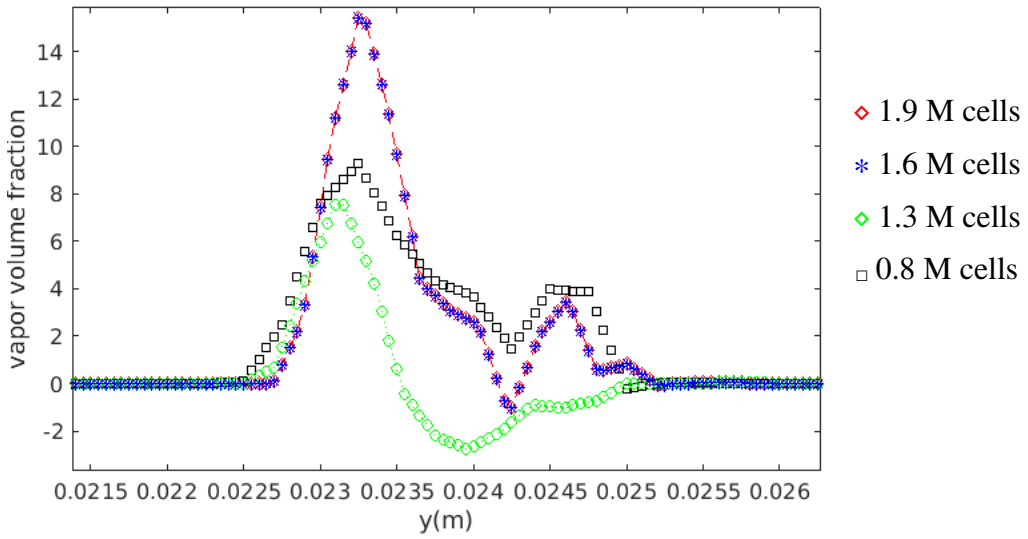

Figure 6.6: Volumetric vapour fraction for mesh study at ambient temperature 363 K, ambient pressure 1 atm and $Re = 16000$

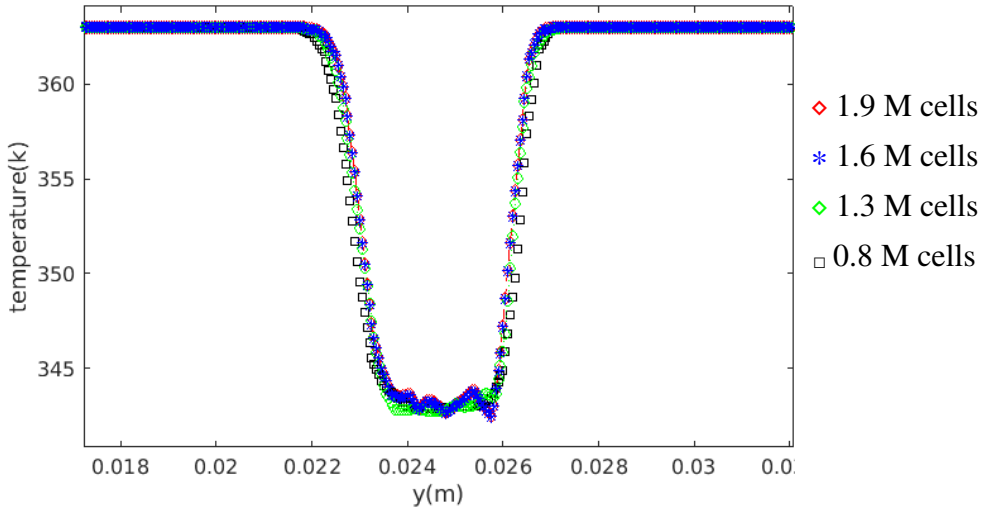

Figure 6.7: Temperature of the flow field for mesh study at ambient temperature 363 K, ambient pressure 1 atm and $Re = 16000$

6.4 Model Validation

The turbulent channel flow validation is performed by comparing the LES results of the current computational solver with DNS results of Moser et al. [82]. The validation of the developed code (interMixingHeatFoam) achieved by comparing results obtained using the solver with experimental results obtained by conducting experiments in the laboratory as well as comparing with empirical correlation of Yearling [83].

6.4.1 Validation of Turbulent Channel Flow

In this section, comparison between LES simulation of gas flow field in current study with DNS data in terms of mean and root mean squared fluctuations is performed.

Fully developed turbulent channel flow is produced by constant pressure gradient in streamwise direction which is taken as X-direction in this study. The Y-direction is orthogonal to the walls and is the wall-normal direction. Finally, the Z direction is the spanwise direction orthogonal to the X and Y directions (figure 6.2).

The study domain and flow direction are shown in figures 6.2 and 6.3. The computation was carried out on a volume mesh of $100 \times 80 \times 80$ grid points along the X, Y and Z directions, respectively. The hexahedral mesh was produced by OpenFOAM utility blockMesh and is shown in figure 6.8.

The mean velocity and the fluctuating components are solved with second order Gaussian integration. The second-order implicit backward scheme was used for time discretization. A second-order accuracy was utilised for the divergence term.

The pressure-velocity coupling was solved by PISO-SIMPLE (PIMPLE) algorithm, that is the combination of the PISO and the SIMPLE algorithms and solves

the momentum and pressure equations, respectively, within the required number of iterations in a time-step. The variable time step was chosen to let the CFL number be always less than the specified number. The solution was carried out using SCOTCH algorithm partitioning to decompose the domain into specified number of sub-domains for parallelizing in MPI protocol.

The mesh was refined near the wall region to include the small eddy behaviour in this area, so that the non-dimensional wall distance, $y_0^+ < 1$ for the first cell (figure 6.8c).

The normalised profile of the averaged velocity scaled with the friction velocity in streamwise direction is illustrated in figure 6.9. The results were compared with the DNS results of Moser et al. [82]. It can be seen that a fully developed symmetrical mean flow velocity profile is reached and in good agreement with DNS data of Moser et al. [82]. Therefore, the resolution of the simulation was found to be sufficient.

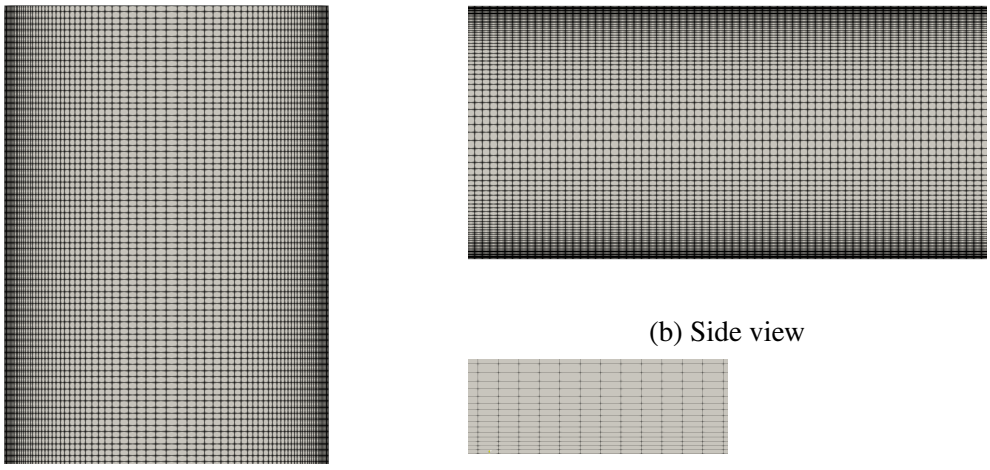

(a) Top view

(b) Side view

(c) Near wall refined mesh

Figure 6.8: Mesh used for the channel flow LES simulation and compared with DNS study Moser et al. [82]

The numerical technique of generating fully developed turbulent flow by means

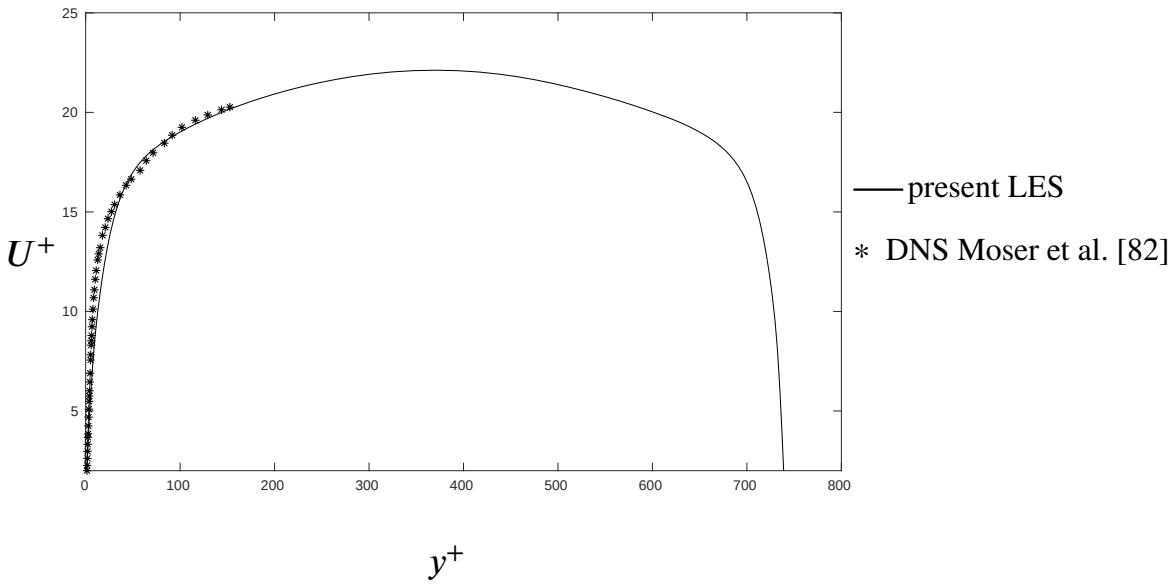

Figure 6.9: Profile of the normalised streamwise mean velocity for turbulent channel flow for $Re_b = 13350$ and $Re_\tau = 395$

of cyclic boundary conditions must be validated to ensure that simulation is performed without non-physical flow features. To this end, LES of an incompressible fully developed channel flow was performed with mean flow Reynolds number and friction Reynolds number, comparable to the Direct Numerical Simulation (DNS) of Moser et al. [82]. Therefore, the Reynolds number of the flow based on the channel height was set to $Re_b = 13350$ and defined as $Re_b = \frac{U_b h}{\nu}$. The bulk velocity is obtained as follows:

$$U_b = \frac{1}{h} \int_0^h u d y \tag{6.1}$$

Where h is the height of the channel. Another characteristic velocity scale to describe turbulent channel flow is the friction Reynolds number, defined as

$$Re_\tau = \frac{u_\tau \delta}{\nu} \tag{6.2}$$

In validated turbulent case, the friction Reynolds number was set to $Re_\tau = 395$, where $\delta = \frac{h}{2}$. The friction velocity, u_τ, is given as,

$$u_\tau = \sqrt{\tau_w / \rho} \tag{6.3}$$

Here, τ_w is the wall shear stress and ρ is the fluid density.

The importance of the Re_τ can be explained from the correlation between the pressure gradient and the wall shear stress [62].

$$-\frac{dp}{dx} = \frac{\tau_w}{\delta} \tag{6.4}$$

As a result, by setting the correct pressure gradient, the desired Re_τ can be achieved. This was accomplished by introducing an external force term in the momentum equation that is calculated based on the bulk velocity, U_b, magnitude. Therefore, in each time step, the external force is adjusted by recalculating U_b.

The primary quantities describing the turbulent fluctuations are the Reynolds stress tensors. It is usual to use the root mean square (r.m.s) of the velocity deviation. Figure 6.10 shows the normalized $u^{r.m.s}$ in the wall-normal direction as a function of the normalized wall distance, y/δ, and figure 6.11 illustrates the wall direction fluctuation. The magnitude of $v_{r.m.s}$ are in good agreement in most of the regions. The maximum value and its location are calculated correctly. The overall results across the entire range are in adequate accurate condition for the purpose of the current study.

The instantaneous velocity fields scaled with the bulk velocity is depicted in figure 6.12 in X-Y plane. The same contour as well as the vorticity in Y-Z plane at the same time are also visualised in figures 6.13a and 6.13b. It can be seen that the flow structures are preserved and turbulent in the core region containing large scale

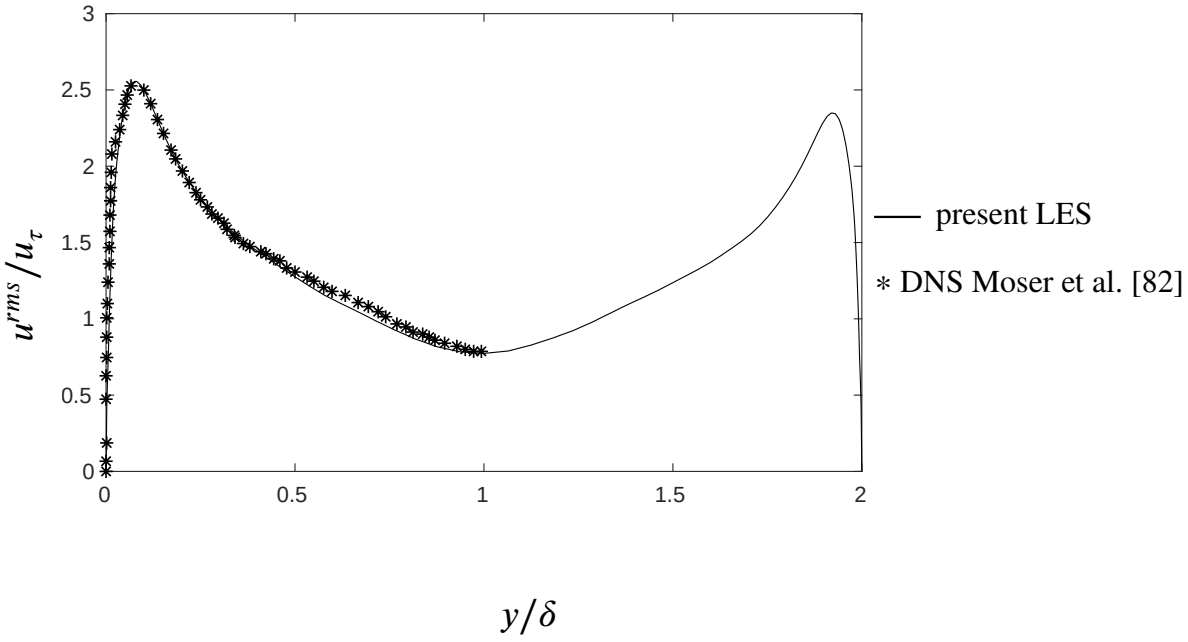

Figure 6.10: Profile of normalised streamwise r.m.s velocity for turbulent channel flow for $Re_b = 13350$ and $Re_\tau = 395$

motions and strong vortical structures bulge toward the walls. In near wall area, (figure 6.14) long elongated structures are seen. The vorticity near the wall region look-like the well known streaky structure in streamwise direction described by Kim and Moin [84]. Maximum value of vorticity, $w = |\nabla \times U|$, occurs in wall regions as predicted by Jiménez et al. [85]. In conclusion, as the mean and instantaneous characteristics of turbulent flow are in good agreement with DNS and turbulent wall bounded flow field structures, the computational solver is suitable for simulation of a fully developed turbulent flow.

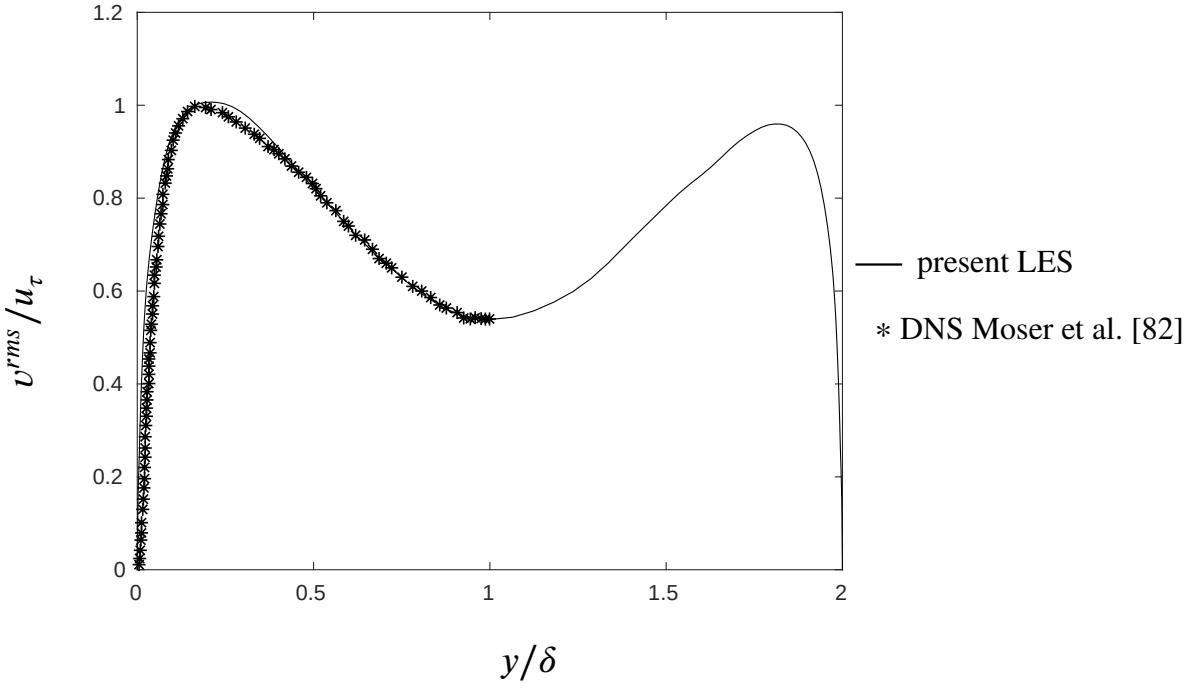

Figure 6.11: Profile of the normalised wall direction r.m.s velocity for turbulent channel flow for $Re_b = 13350$ and $Re_\tau = 395$.

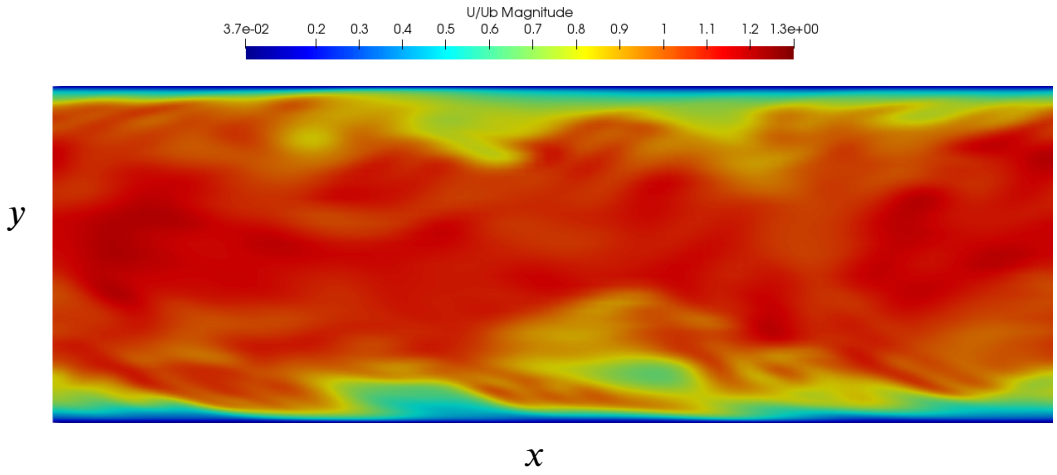

Figure 6.12: Visualisation of the turbulent channel flow given by instantaneous velocity magnitude normalised by bulk velocity over a constant Z plane for $Re_b = 13350$.

6.4.2 Validation of Computational Set-up and Developed Code

The primary validation of numerical results obtained by interMixingHeatFoam was tested by some set of experimental tests. Details about the experimental setup are given in section 5.6. The comparison of the experimental results and numerical simulation for water droplet falling in turbulent flow field is illustrated in figure 6.15 where the time evolution of drop diameter is illustrated. The droplet diameter for the numerical case is calculated based on the liquid volume fraction, $\alpha_l = 0.9$. The variation of the drop size in the evaporation process can be related to the time as given by equation 6.5.

$$d^2 = d_0^2 - Kt \tag{6.5}$$

In this equation, K depends on the thermodynamic properties of the droplet as well as the flow characteristics and is called evaporation rate. Here, t, d and d_0

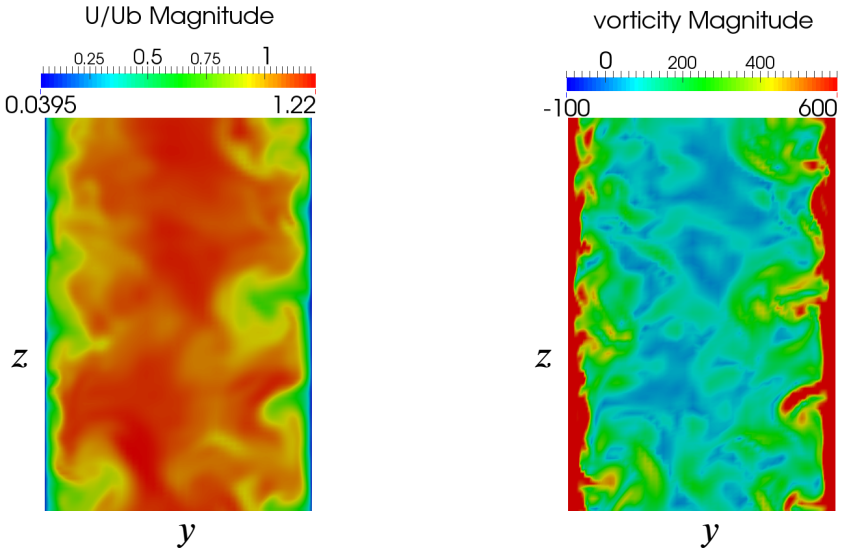

(a) (b)

Figure 6.13: Visualisation of the turbulent channel flow characteristics; (a) instantaneous velocity magnitude normalised by bulk velocity and, (b) instantaneous streamwise vorticity over a constant X plane at $Re_b = 13350$.

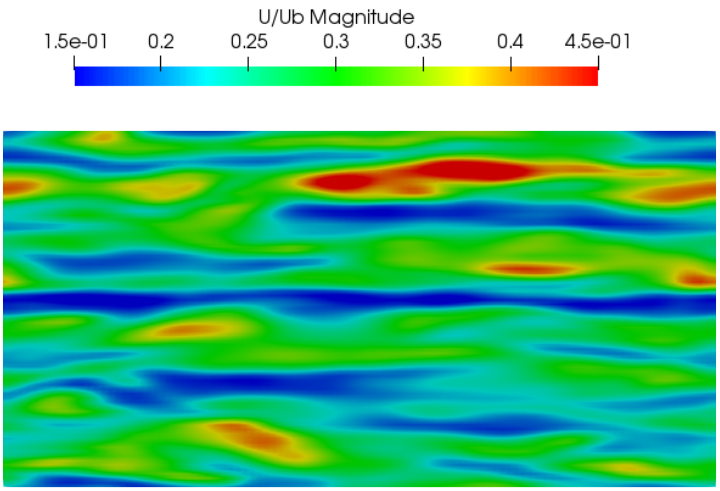

Figure 6.14: Turbulent flow structures in near-wall region

are the time of evaporation, droplet instantaneous diameter and initial diameter, respectively. The droplet diameter in the experimental analysis is calculated by assuming ellipsoidal shape for the droplet as proposed by Sakai and Saito [86].

$$d = \sqrt[1/3]{d_h^2 d_v} \tag{6.6}$$

Here, d_h and d_v are minor and major axis length, respectively. However, the rotation of the drop due to the turbulent nature of the air flow makes the droplet deform and flatten. Therefore, referring to figure 6.16, the ellipsoidal assumption for the drop is not acceptable any more. On the other hand, due to the special setup of the test rig, the addition of another camera to capture the third dimension of the droplet was impossible. As can be seen in figure 6.16, the evolution of the droplet size in the experimental test is mostly in very good agreement with numerical data. Though, in two points there are some differences between the numerical and the experimental data that can be justified by the non-elliptical shape of the droplet during the experiment. Therefore, the numerical results are still reasonably in good agreement with the experimental data.

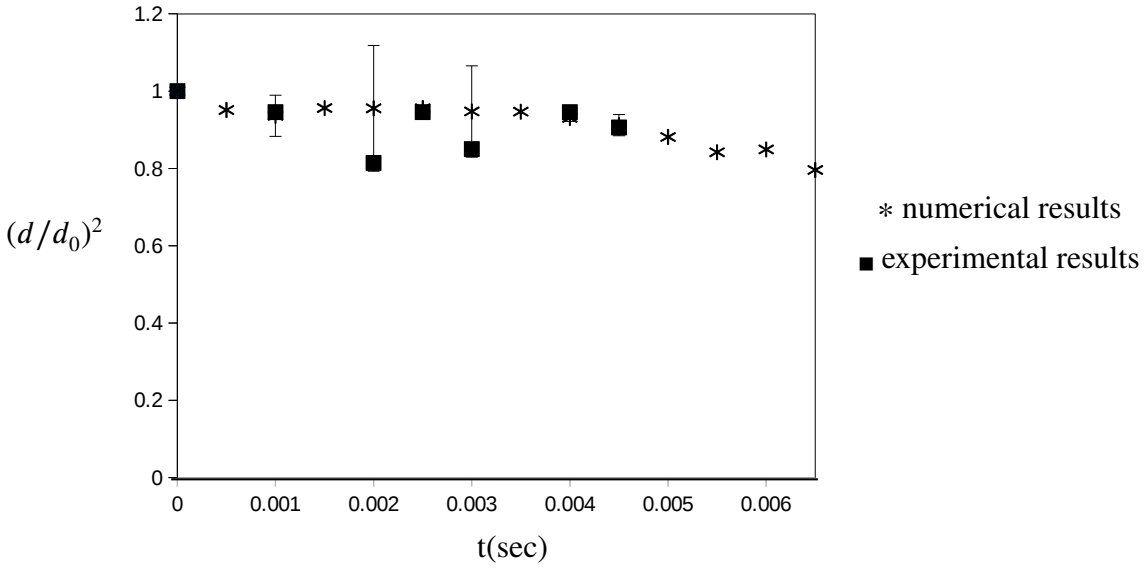

Figure 6.15: Water droplet diameter history in turbulent air flow

Another validation is performed using empirical correlations developed by Yearling [83]. This relationship is for turbulent flow mass transfer and includes wide range of Reynolds number, $2 \leqslant Re_\infty \leqslant 1.33 \times 10^6$, and droplet diameter, $0.50 \leqslant d(mm) \leqslant 305$. The correlation states a relationship for Sherwood number as a function of mass transfer number, B_M, to account vapour species around the droplet.:

$$Sh = \frac{2 + Re_D^{1/2} Sc^{1/3}(0.562 + 0.1807 d^{1/2} + 0.0672 I_\infty (I_\infty + 0.05) Re_\infty^{1/2})}{(1 + B_M)^{0.7}} \quad (6.7)$$

where $Sc = \mu / D_{vg}$ is the Schmidt number, Re_D is the Reynolds number based on droplet diameter and Re_∞ is the freestream Reynolds number. In correlation 6.7, d is the droplet diameter and B_M is Spalding mass transfer number, defined as

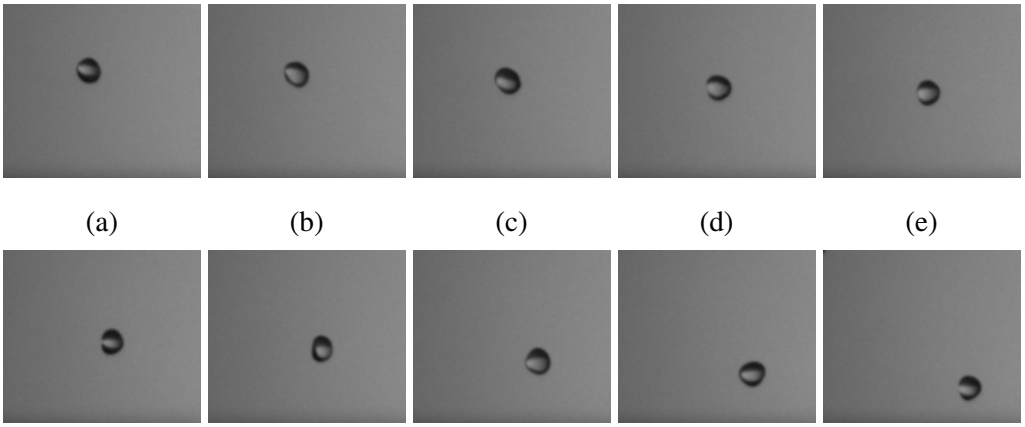

(a) (b) (c) (d) (e)

(f) (g) (h) (i) (j)

Figure 6.16: Water droplet spinning and deformation into non-elliptical form in turbulent flow in experimental study; $\Delta t \approx 1ms$

$$B_M = \frac{Y_{Fs} - Y_{F\infty}}{1 - Y_{Fs}} \tag{6.8}$$

where Y_{Fs} and $Y_{F\infty}$ are vapour mass fraction at the droplet surface and far from the droplet, respectively. The comparison of asymptotic Sherwood number of the present study with Yearling [83] and the corresponding error are presented in Table 6.2. It can be seen that the error between the numerical model and the experimental correlation is less than 5% and small. Therefore, this comparison suggests that the numerical model can be used for further investigation of droplet evaporation in turbulent channel flow.

Table 6.2: Comparison of *Sh* with empirical correlation

	Sh		
	interMixingHeatFoam	Yearling [83]	Error(%)
$Re = 12000$	24	23.16	3.6
$Re = 16000$	21.6	20.71	4.3

6.5 Results

This section is devoted to the investigation of the effect of turbulence on the evaporation of a single water droplet in turbulent channel flow. To this end, the effect of turbulence on the evaporation is considered for two different Reynolds numbers for turbulent flows. Besides, the evaporation of droplet in a laminar flow field and standstill air are inspected. The results are obtained with numerical study by means of the developed code, interMixingHeatFoam. Air is the fluid medium for all of the simulations, acting as a carrier gas.

6.5.1 Effect of Reynolds Number on Evaporation

To investigate the effect of turbulence on evaporation, four cases for the air inside the channel are considered; two in the turbulent region, one in laminar flow, and one in quiescent air. The only variable parameter is the air flow velocity. All other properties are the same. The droplet size and flow characteristics are given in Table 6.3. Reynolds number is based on the hydraulic diameter of the channel. Normalised velocity profile as a function of the channel wall distance is illustrated in figure 6.17 where the flat profiles for developed turbulent flows are compared to the parabolic profile of the developed laminar flow.

Normalised RMS velocities in streamwise direction, wall direction and spanwise direction are shown in figure 6.18 in order to compare turbulent characteristics of different turbulent flows. In a fully-turbulent channel flow, the RMS velocities exhibit weak dependence on Re [62]. Therefore, nearly similar values of u/u_{mean} are seen.

The diameter time history of the droplet is illustrated in figure 6.19. The droplet lifetime in quiescent air and laminar flow follow the well known d^2-law. However, due to high evaporation rate in turbulent flow, droplet evolution does not obey the

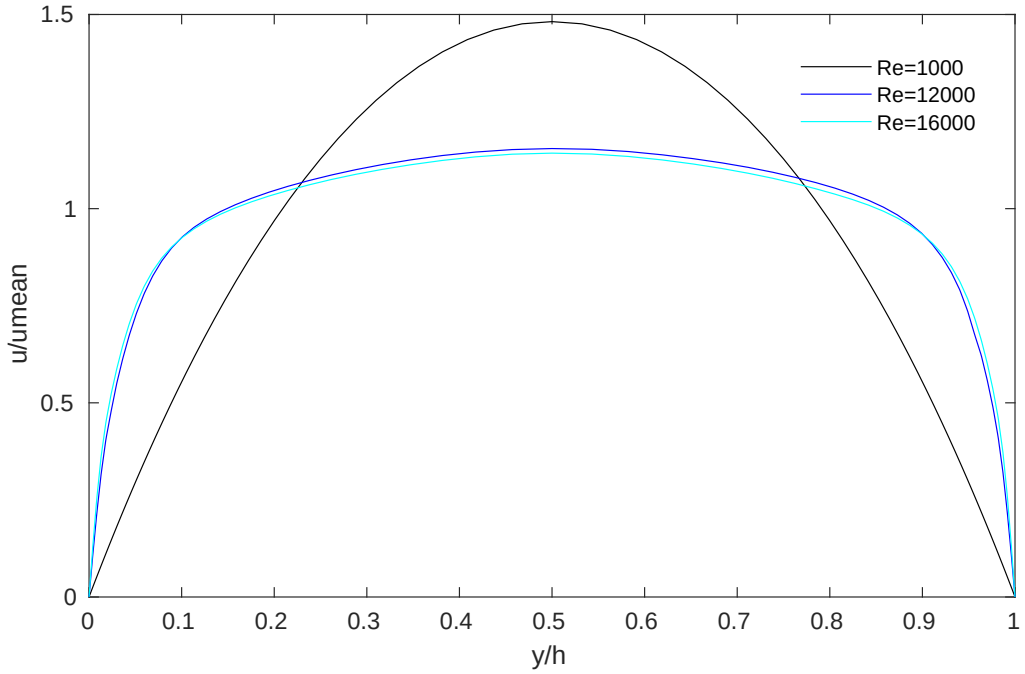

Figure 6.17: Normalised velocity profile of different Reynolds numbers.

Table 6.3: Droplet and air flow characteristics in turbulent study

Case	Re_{hyd}	Re_{τ}	T_{air}(K)	T_{drop}(K)	r_0(mm)	liquid
quiescent	0		313	295	4	water
laminar	1000		313	295	4	water
turbulent1	12000	234	313	295	4	water
turbulent2	16000	306	313	295	4	water

d^2-law in turbulent flows. The average droplet lifetime, defined as the time taken by a droplet to completely evaporate, varies with the Re number. Corresponding evaporation rate is given in Table 6.4. For the laminar flow the lifetime of the drop is slightly less than the lifetime of the drop in quiescent air and is nearly 93 ms. However, turbulence affects the lifetime tremendously. While, the lifetime in both of the turbulent cases are less than the laminar case, the higher Re does not

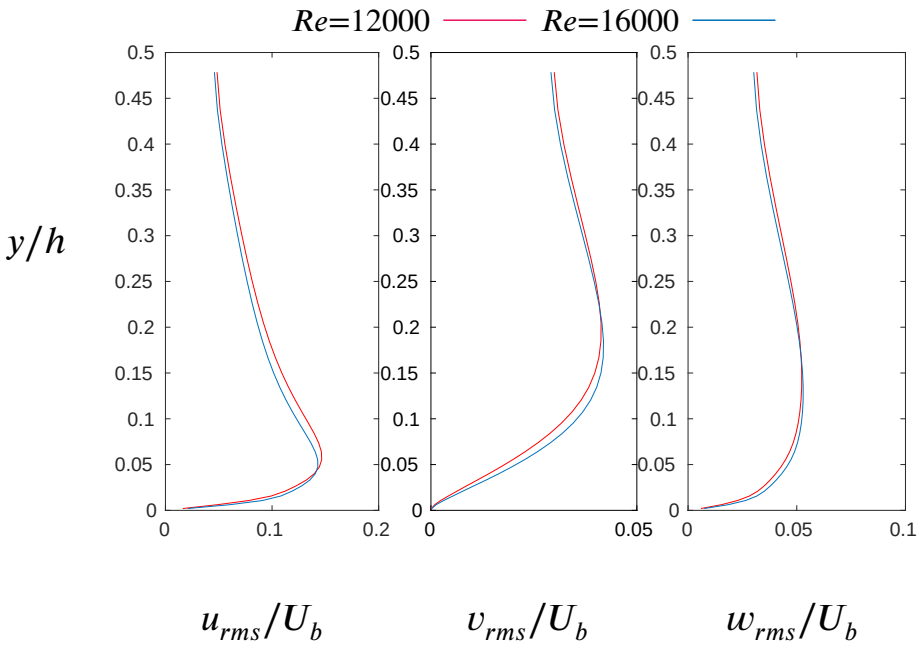

Figure 6.18: RMS velocity normalised by the bulk velocity in near wall region (a) streamwise direction, (b) wall direction and (c) spanwise direction.

increase the lifetime as much as the lower Re in turbulent region. The total lifetime in $Re = 16000$ and $Re = 12000$ are around 48 ms and 28 ms, respectively.

Table 6.4: Evaporation rate for different flow regimes

	quiescent	laminar	$Re = 12000$	$Re = 16000$
$K(mm^2/s)$	0.00048	0.00060	0.00208	0.00118

Hereafter, the reason for different evaporation rates of the droplet in different flow regimes is explained. The cause for higher evaporation in lower Re in turbulent flow is of special interest.

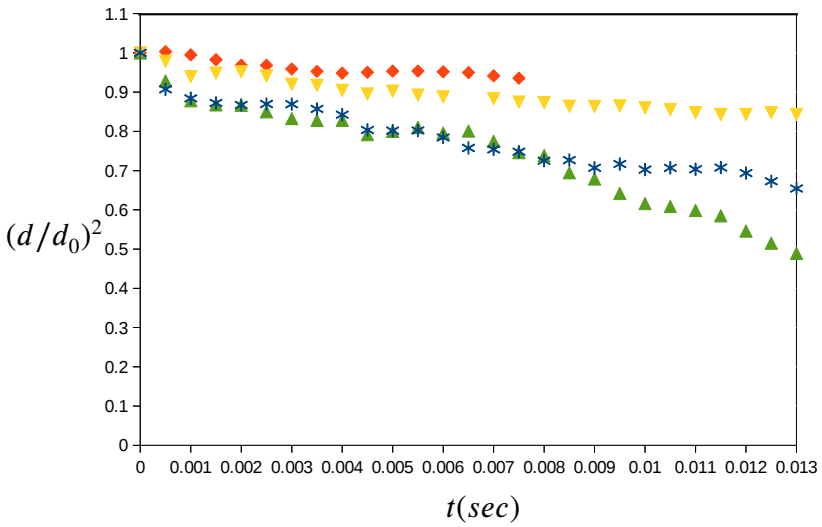

Figure 6.19: Normalised drop diameter squared history; ◆ quiescent, ▼ laminar, ∗ $Re = 16000$ and ▲ $Re = 12000$.

6.5.2 Unsteady Flow Around The Droplet

First of all, to see the effect of Re on droplet evaporation, the mixing dynamics around the drop is considered. The mixing affects the turbulence generation and consequently the evaporation. Figure 6.20 shows the vorticity in streamwise direction around the droplet for $Re = 12000$.

Looking at the vorticity field, defined as $w = |\nabla \times U|$, during the time, the turbulence modulation on the area surrounding the droplet can be noticed. In fact, there is a two-way coupling between the drop and the flow, inasmuch as, the momentum exchange between the drop and the flow happens and changes the turbulence. The drop surface behaves like a wall and affects the local flow and mixing characteristic. Vortex shedding by the droplet reshapes the flow structure and turbulence scale. Hence, it is a source of turbulence generation.

Vorticity fields of turbulent flow for $Re = 16000$ is depicted in figure 6.21, to show the effect of Re on the fluid dynamics surrounding the drop. Comparing

figures 6.20 and 6.21, it can be seen that the vortical structure near the droplet for lower *Re* seems thicker all the times. Near the droplet in both of the turbulent cases, there are some rotating vortices, known as rolls, connecting together. However, during the time some rolls go further from the droplet. This is the result of the vapour creation due to evaporation from the droplet. The vapour envelops the drop and mixes with vortical structure to push the strong vorticities away from the droplet. As a result, the turbulence structure is modulated. In figure 6.20, vorticity field nearer to the droplet seems thicker and stronger and contains more rolls comparing to higher *Re* that can increase mixing of vapour and ambient air and subsequently increases evaporation rate. Figures 6.22 and 6.23 show vapour mixing with vortical structure at 12.5 ms. The major difference between two cases is the more mixing between the vapour and fluid structure for lower *Re*, that is seen by nearly uniform distribution of vapour concentration around the droplet. In contrast, less and non uniform vapour concentration for higher *Re*, implies less mixing.

Despite the popularity of the vorticity magnitude contours for the purpose of identifying vorticity, due to the fact that the method is not able to discern between swirling motion and shearing motion in boundary walls (where there is noticeable shear), it is not sufficient to use for identifying vortices [87, 88] in a channel flow simulation. Therefore, to have a better understanding of the vortices and assess the consequent influence in overall flow, another approach is pursued.

By defining a vortex as a connected fluid realm with a second invariant of ∇u [89], the gas-phase eddies also can be visualised by iso-surface of second invariant of the velocity gradient tensor (Q-criterion) defined as

$$Q = \frac{1}{2}(\Omega_{ij}\Omega_{ij} - S_{ij}S_{ij}) \tag{6.9}$$

where $\Omega_{ij}$is the skew-symmetric rate-of-rotation-tensor, and equals to the vortic-

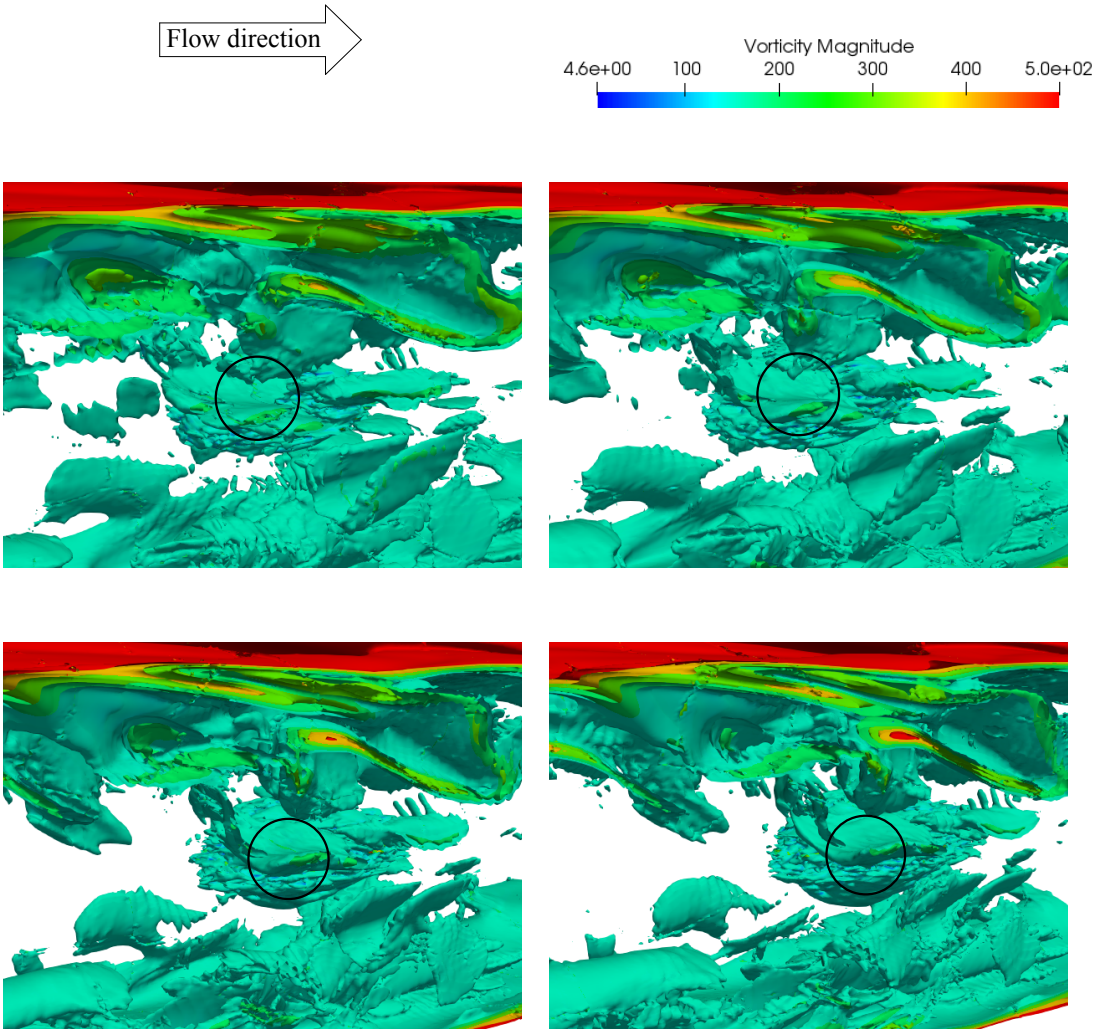

Figure 6.20: Vorticity field around the droplet in $Re = 12000$ at (a) 9 ms, (b) 12.5 ms, (c) 17.5 ms and (d) 22.5 ms left to right, respectively in streamwise direction.

ity as well. It is defined as

$$\Omega_{ij} = \frac{1}{2}\left(\frac{\partial u_i}{\partial x_j} - \frac{\partial u_j}{\partial x_i}\right) \tag{6.10}$$

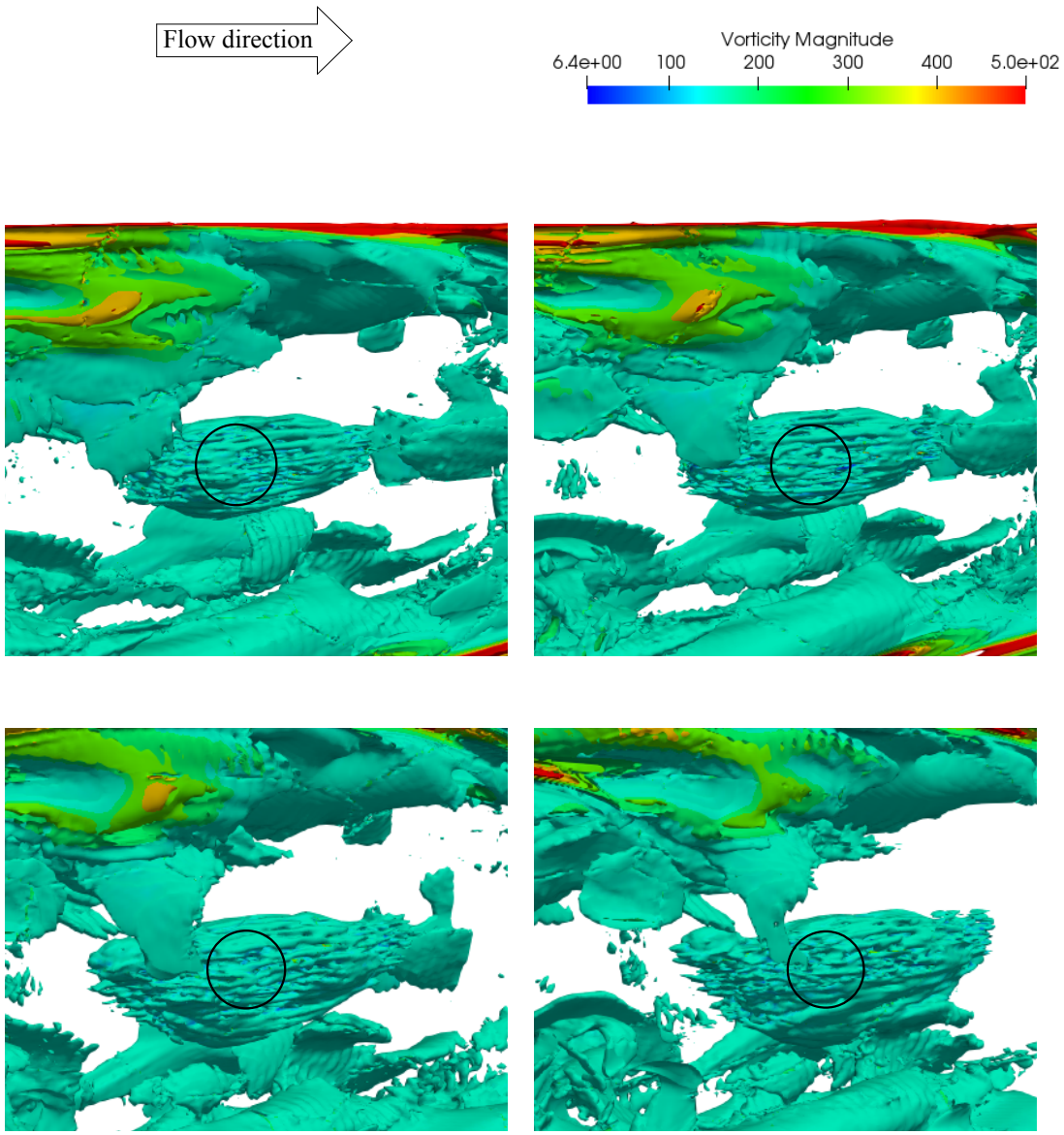

Figure 6.21: Vorticity field in streamwise direction around the droplet in $Re = 16000$ at (a) 9 ms, (b) 12.5 ms, (c) 17.5 ms and (d) 22.5 ms left to right, respectively.

and $S_{ij} = \frac{1}{2}(\frac{\partial u_i}{\partial x_j} + \frac{\partial u_j}{\partial x_i})$is the symmetric rate-of-strain-tensor. Figure 6.24

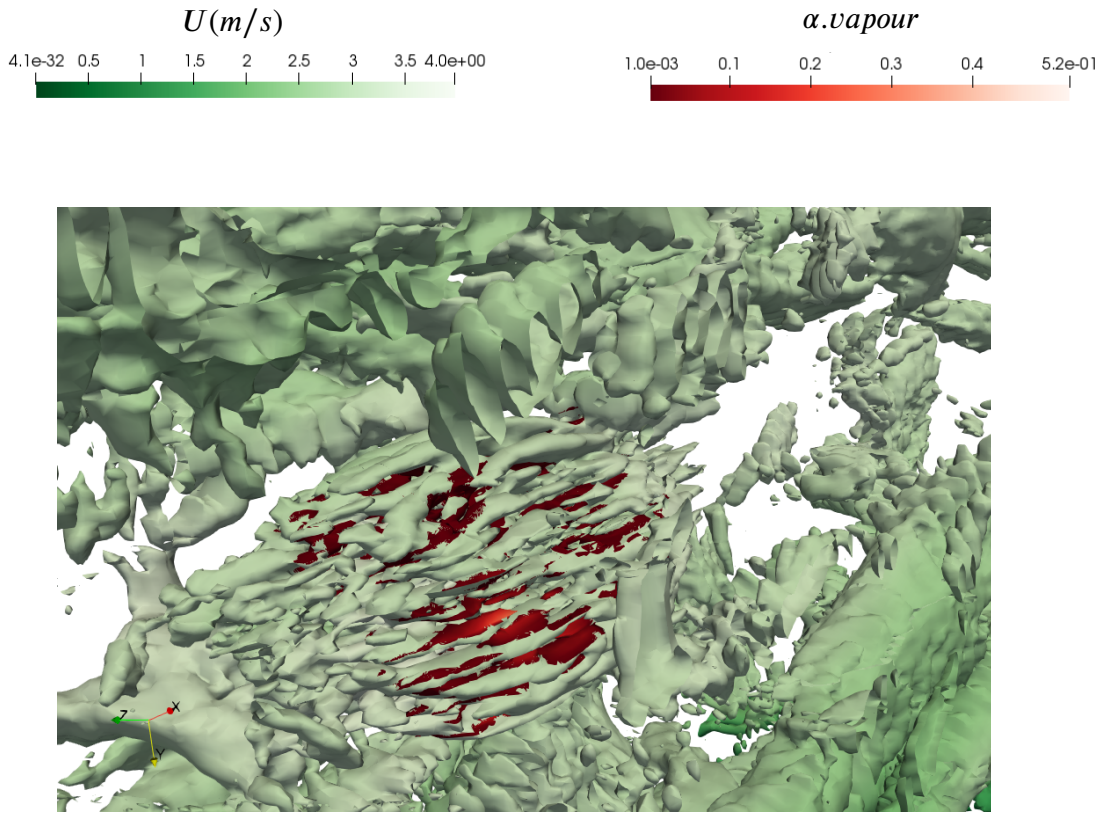

Figure 6.22: Vapour mixing with fluid structure at 12.5ms coloured by streamwise velocity in $Re = 12000$.

presents Q-criterion of two different turbulent fields normalised by mean streamwise velocity containing a droplet at different times coloured by streamwise velocity. Due to the fact that the positive value of Q-criterion denotes vorticity, the values shown in figure 6.24 are representing the vortices. Apparently, larger coherent turbulent eddies and streamwise vortices are seen through the channel as well as around the drop in lower Re causing more pronounced mixing layer around the drop. However, vortex stretching is relatively stronger bringing bigger wake region past the drop in higher Re due to higher mean velocity.

In conclusion, comparing the results of figures 6.20 and 6.21 with figure 6.24, implies different fluid structures in two turbulent flows. More coherent structures

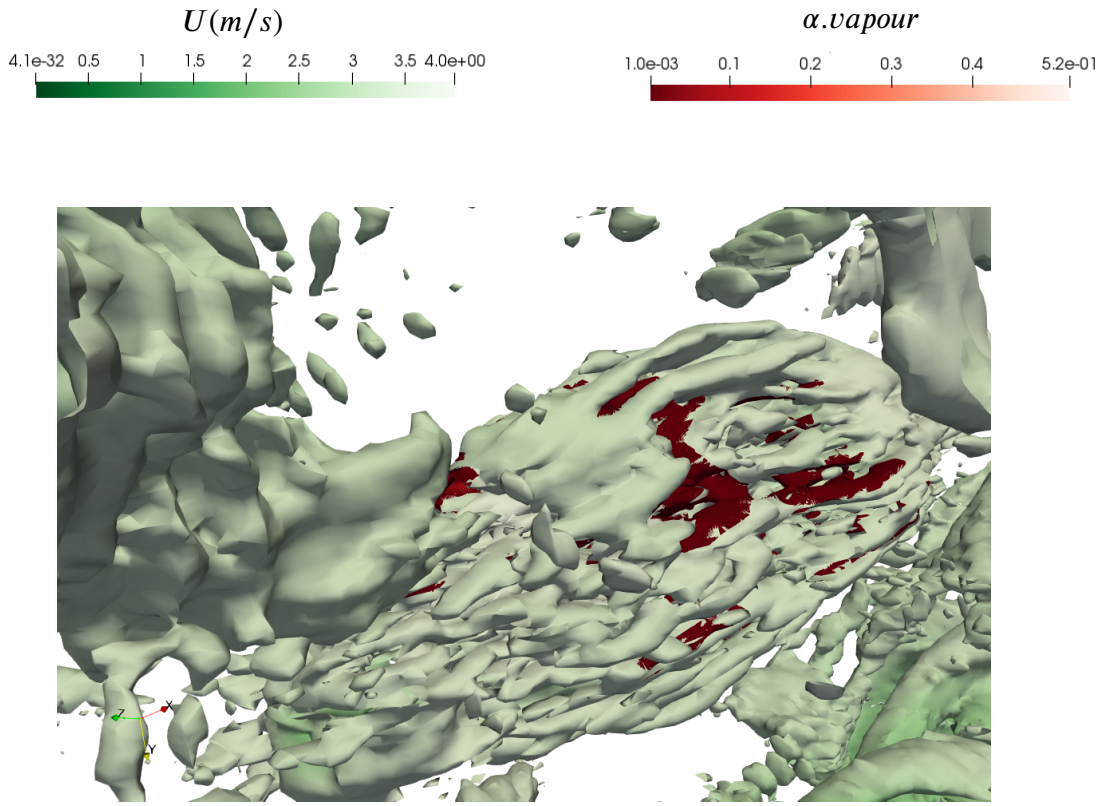

Figure 6.23: Vapour mixing with fluid structure at 12.5ms coloured by streamwise velocity in $Re = 16000$.

in lower Re resulting in greater mixing layer in lower Re near the droplet is observed. Contrary to this, the higher Re broadens the wake area and brings less strong interaction with the drop.

To have a better understanding about the turbulent characteristics of two turbulent cases, the dissipation rate defined in equation 6.11 can be used.

$$\epsilon = 2\nu s_{ij} s_{ij} \tag{6.11}$$

Where ν and s_{ij} are the kinematic viscosity and fluctuating rate of strain. Dissipation rate of turbulent flows are shown in figure 6.25 upstream of the droplet. As can be seen, dissipation rate is higher near the droplet due to higher strain rate in

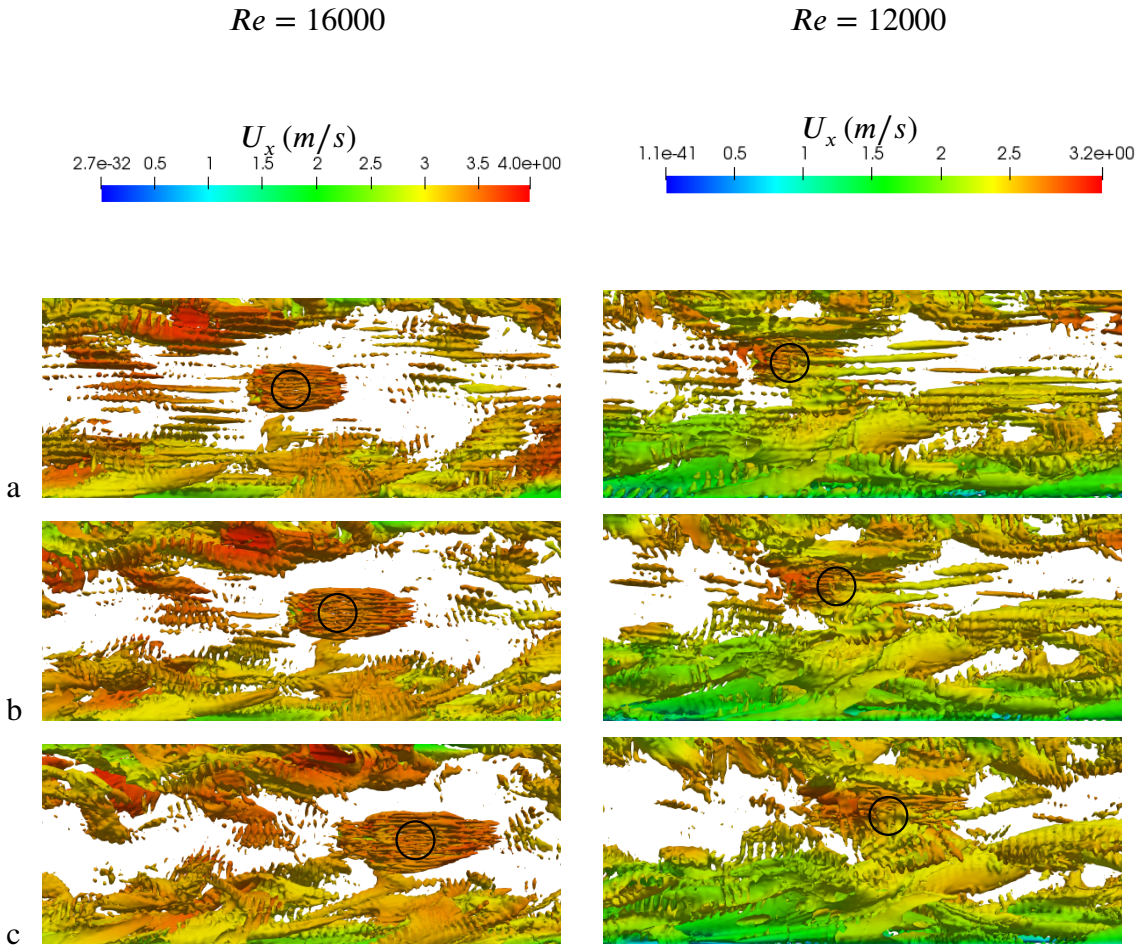

Figure 6.24: Visualisation of vortical structures by Q-criterion iso-surface at $Q/(U_x/h)^2 = 0.5$ coloured by mean streamwise velocity at (a) 3 ms (b) 6 ms (c) 12.5 ms. Droplet is shown by a circle

all cases. The increase of dissipation rate near the droplet is in accordance with the argument that the droplet behaves like a wall, makes the local flow non-isotropic and changes local mixing. According to figure 6.25, dissipation rate for Re=16000 at 3 ms is higher than Re=12000 and at 6 ms and 9 ms is lower. In fact, dissipation rate does not depend on Re in fully developed channel flow [90]. Therefore,

higher Re does not provide higher ϵ in outer region of the duct. On the other hand, comparing the droplet boundary layers at these times (figure 6.24), it can be concluded that the dissipation rate is higher when there is thicker boundary layer as it is in Re=12000 at 6 ms and 9 ms (It agrees the fact that the droplet operates like a wall, since ϵ is higher near the wall). Thicker boundary layer around the droplet brings more transformation of turbulent kinetic energy into internal energy. Therefore, higher heat transfer can be provided and appears to be the reason for higher evaporation rate at these times.

6.5.3 Impact of Reynolds Number On Temperature Field

The temperature field in quiescent air and laminar flow are shown in figures 6.26 and 6.27, respectively. The initial temperature of the air and droplet are 310 K and 290 K, respectively. Hence, there is initially 20K temperature difference between the air and the droplet. In standstill air and laminar flow, after 4 ms has elapsed the temperature inside the droplet increased to nearly 295 K. The temperature in the interface region is higher compared to the droplet temperature. A symmetrical temperature field around the drop is also observed for the droplet in laminar flow. In contrast, a slightly asymmetrical field near the drop exists in laminar flow which is the result of shear layer in the flow field. However, the heat transfer around the droplet in laminar flow is not improved comparing to the quiescent air. This means that the primary mechanism of heat transfer in laminar flow, similar to the quiescent air, is conduction heat transfer.

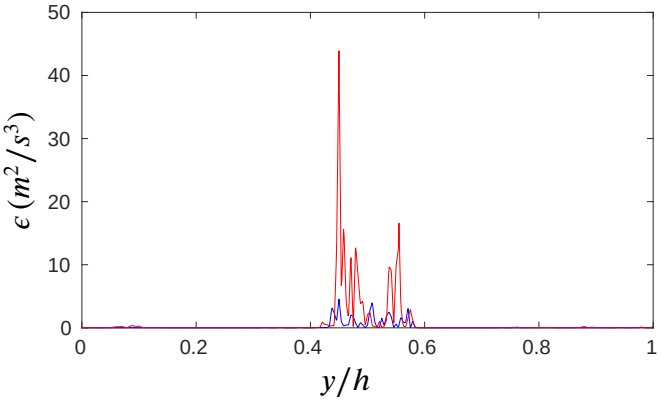

(a)

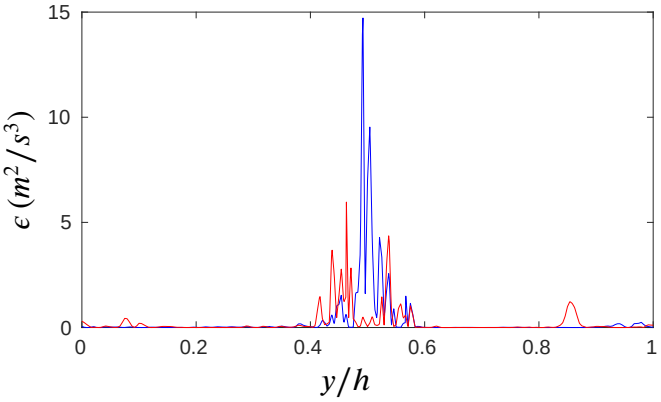

(b)

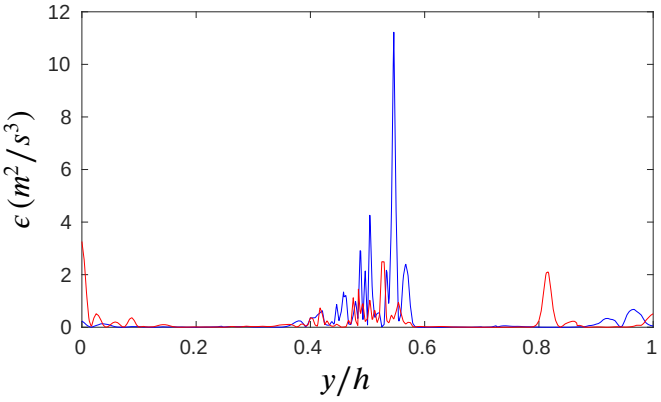

(c)

Figure 6.25: Dissipation rate upstream of the droplet along the channel height; blue line represents Re=12000 and red line shows Re=16000 at (a) 3 ms (b) 6 ms (c) 12.5 ms

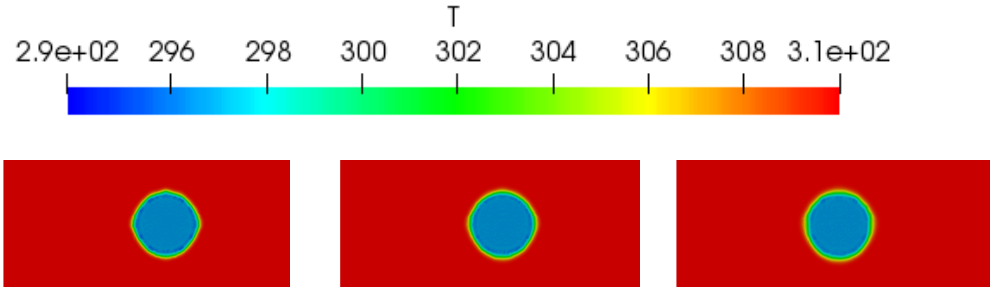

Figure 6.26: Temperature field (K) around the droplet in quiescent air at (a) 4 ms, (b) 5.5 ms and (c) 7.5 ms left to right, respectively.

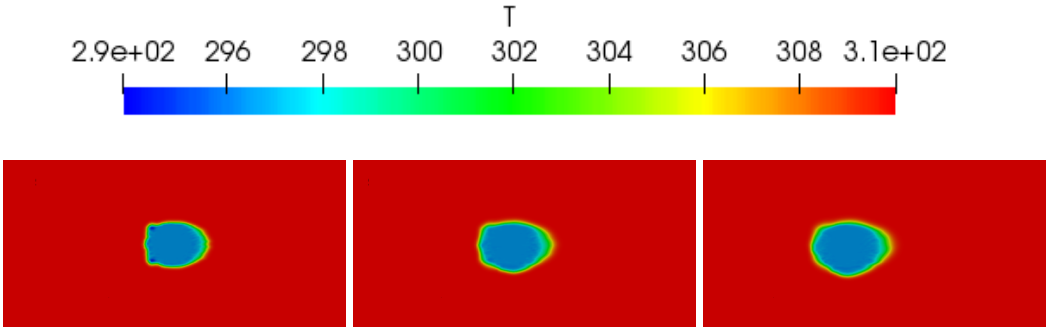

Figure 6.27: Temperature field (K) around the droplet in laminar flow, Re=1000, at (a) 4 ms, (b) 9 ms and (c) 12.5 ms left to right, respectively.

An obvious difference between temperature field in standstill air and laminar flow when compared with turbulent flow cases is the lower temperature field inside and around the droplet in turbulent flow cases. This means that the cooling process happens faster and extends to a larger area in turbulent flow. In non-turbulent cases, the higher temperature inside the droplet at the same time period shows that the drop warms up faster without significant heat transfer to the surrounding environment. The generated layer of vapour envelopes the droplet in the non-turbulent flow and the lack of strong turbulent field to scatter it, acts like a blanket

for the drop, and heats up the droplet by conduction mechanism without increasing evaporation. Hence, there is only an increase in temperature but no evaporation.

The high vorticity area around the droplet is explained by considering the temperature field in the region (figures 6.28 and 6.29). The temperature field around the droplet is not symmetric. This finding highlights the correlation between streamwise velocity and temperature in boundary layer flow. However, the initial uniform temperature field inside the channel does not let the temperature field to be streaky near the walls.

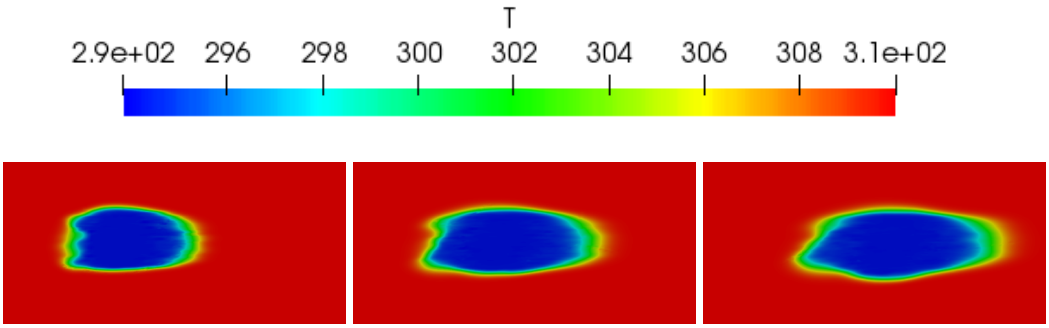

Figure 6.28: Temperature field (K) around the droplet for $Re = 12000$ at (a) 4 ms, (b) 9 ms and (c) 12.5 ms left to right, respectively.

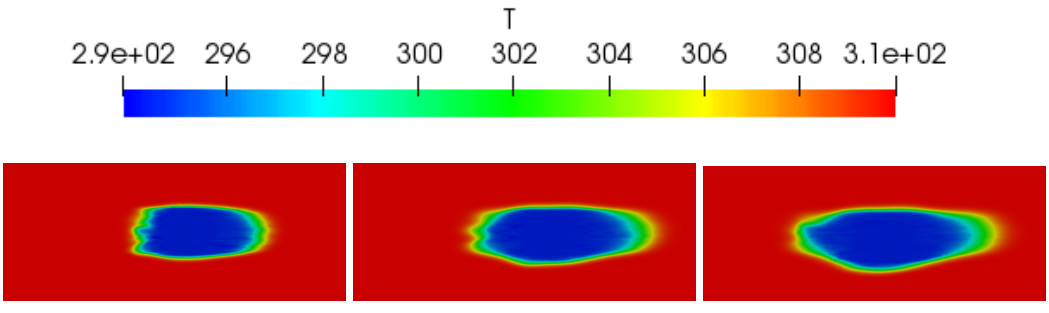

Figure 6.29: Temperature field (K) around the droplet for $Re = 16000$ at (a) 4 ms, (b) 9 ms and (c) 12.5 ms left to right, respectively.

6.5.4 Impact of Reynolds Number On Vapour Distribution

Figures 6.30 to 6.33 show the vapour volume fraction generated around the droplet for different flow regimes. In addition to the different amounts of the produced vapour around the droplet, the distribution of the vapour has distinct pattern in quiescent air, laminar flow and turbulent flows. In quiescent air, a perfect symmetrical boundary layer around the drop is formed. While, in laminar flow the Fickian flow operation disperses the vapour layer in streamwise direction and, hence the vapour can be seen just in wall direction which there is no convectional air flow.

Despite there is no sharp clear-cut between vapour layer in turbulent flows, in $Re = 12000$ especially at 17.5 ms thicker vapour layer can be seen. Referring to figure 6.25, it can be concluded that the higher dissipation rate for $Re = 12000$ is likely to disperse vapour more effectively than for $Re = 16000$.

Comparing the vapour field in figure 6.32 and 6.33, with the results of Happer et al. [91] shown in figure 6.34, dissimilarity between the vortical structure around the drop in these figures with the simulation of Happer et al. [91] exits. This is explained due to the presence of the vapour layer in the current case while in the case of Happer and Moore [91] there is only a pure liquid drop and no vapour. Evaporated vapour released from the drop interacts with the ambient air in the channel and creates clusters of vapour which affects the fluid structure near the drop. Consequently, the importance of considering the vapour as a separate phase to understand the effect of turbulent flow on evaporation dynamics is highlighted.

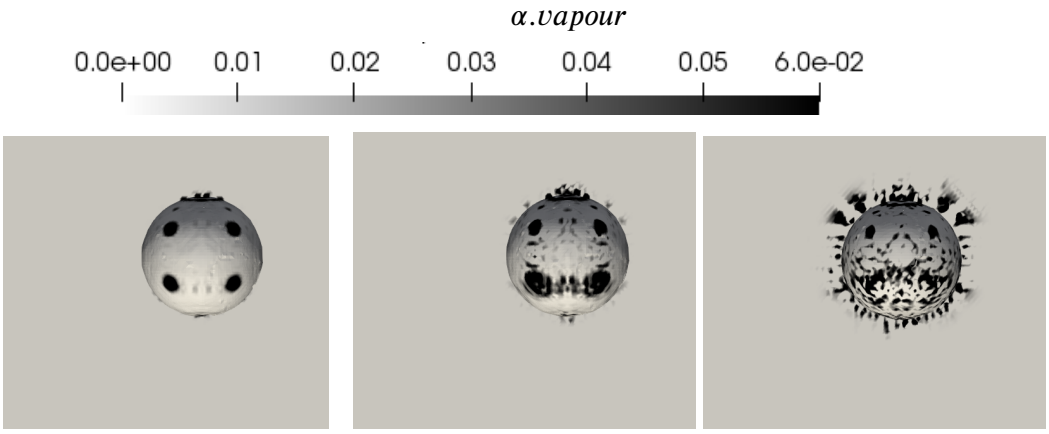

Figure 6.30: Vapour field around the droplet in quiescent air at (a) 4 ms, (b) 5.5 ms and (c) 7.5 ms left to right, respectively.

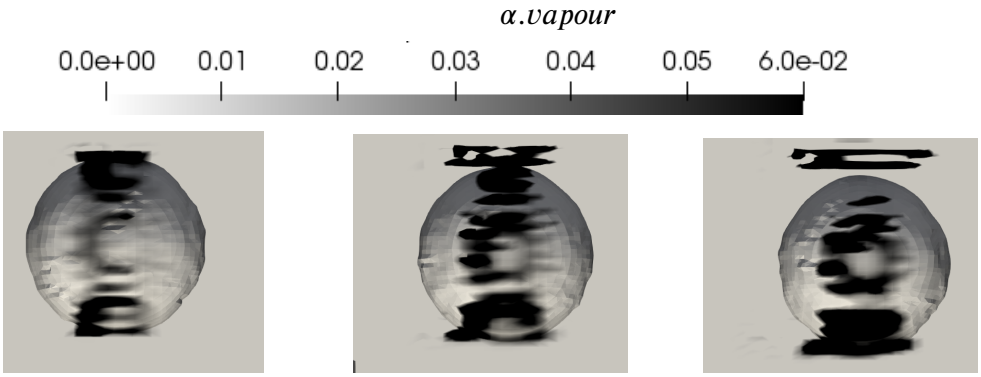

Figure 6.31: Vapour field around the droplet in laminar flow at (a) 4 ms, (b) 9 ms and (c) 12.5 ms left to right, respectively.

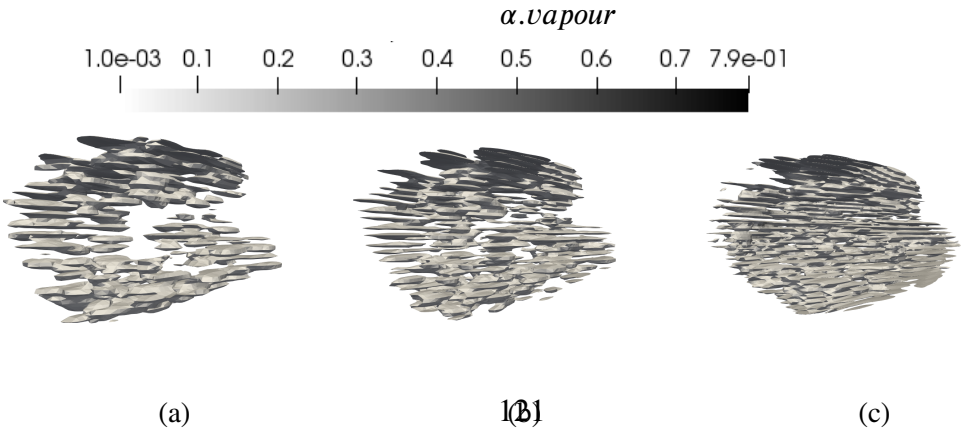

(a) (b) (c)

Figure 6.32: Vapour field around the droplet in $Re = 12000$ at (a) 9 ms, (b) 12.5 ms and (c) 17.5 ms left to right, respectively.

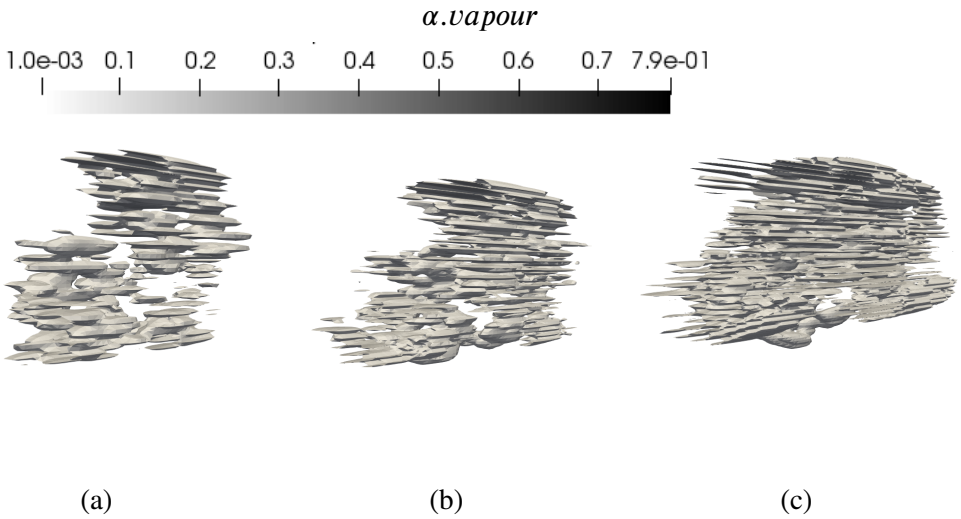

(a) (b) (c)

Figure 6.33: Vapour field around the droplet in $Re = 16000$ at (a) 9 ms, (b) 12.5 ms and (c) 17.5 ms left to right, respectively.

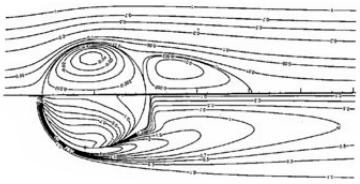

Figure 6.34: Streamlines and vorticity field of a droplet [91]

Referring to section 1.2, one of the mechanisms involved in evaporation improvement by turbulent flow, is the diffusion of vapour layer around the drop. As the vapour layer is broken (destructed) by the ambient flow, more intense turbulent flow does not create more improvement in evaporation rate. This is in accordance with the finding of Birouk et al. [42] and Zoby et al. [41]. As matter of fact, higher Re has larger conventional flow which is able to stretch more the boundary layer surrounding the drop and makes it thinner that decrease mixing. That is why the

higher *Re* does not guarantee the higher evaporation rate. Hence, there might be an optimised *Re* for channel flow which is providing enough energy for scattering vapour layer and still has low convectional flow that does not decrease mixing.

6.6 Summary

This chapter has detailed the numerical case description, problem description and mesh independent study. The turbulent channel flow validation and the developed code validation are carried out by means of the DNS results and experimental data, respectively. The evaporation rate obtained from the simulation of droplet in standstill air, laminar flow and turbulent flow are presented and discussed in detail. The reasons of different evaporation rates especially in two different turbulent cases are discussed.

Chapter 7

SUMMARY AND CONCLUSIONS

In the preceding chapters detailed description of the importance of the current study, the developed code and the numerical methods used for the analysis, experimental setup designed and utilised to verify the numerical results and the findings obtained from the analysis are presented. The following section presents the summary of the main findings from the current research and recommendations for future studies on the topics.

7.1 Summary and Conclusions

The innovative research presented in the thesis can be categorised into two sections. Firstly, a novel method is used to model evaporation process using the VOF method, proposing a remedy for accommodating the extra volume of vapour generated during the phase change. The code is capable of considering three different phases-liquid, vapour and ambient gas. In this regard, a C++ code has been developed in OpenFOAM and used to model the heat and mass transfer of a drop. A set of laboratory experiments were performed to verify the numerical results with the experimental data. To this end, an experimental rig was designed and fabricated to

comply with the requirement of the current research. Besides, another validation is performed using experimental data of Yearling [83]. The effect of turbulent flow on drop evaporation is studied by comparing the results with those of the evaporation in laminar flow and tranquil atmosphere. The numerical data simulation of droplet freely falling in turbulent flow with specific consideration in the presence of the vapour phase has produced significant results.

The evaporation rate was found to be sensitive to the turbulence but the higher Reynolds number does not provide higher evaporation rate. In the following, the important findings drawn from the numerical investigation of the current research are presented:

- Droplet acts like a solid wall in turbulent flow in adjusting turbulence and reforming vortical structures.

- During simulation, the vapour phase was considered as a separate phase, to investigate the behaviour of vapour boundary layer in evaporation and turbulence which has been ignored by many other investigators. It is shown that, the vapour phase is able to modify the turbulence structure by mixing with the vortical structure.

- Comparing two fully turbulent channel flow cases, higher Reynolds number generates thinner vorticity area around the drop due to higher mean convective flow. This makes less mixing between the vapour boundary layer and ambient flow also results in smaller coherent structures around droplet.

- Temperature field inside the droplet in quiescent air and laminar flow cases increase rapidly and have less cooling effect due to the ambient air. This is due to the generated vapour layer around the drop that resists heat and mass transfer.

- In turbulent flow, the heat transfer between the drop and the environment is stronger and affects a larger area compared to non-turbulent flow.

- The vapour field surrounding the drop in standstill air is symmetrical. In laminar flow diffusion of air flow makes vapour boundary layer dispersed in wall direction by enabling higher Fickian flow. However, the generated vapour in turbulent cases are scattered due to higher convection in the mean flow.

- There is a difference in the vapour boundary layer thickness in the two turbulent flow cases. The difference between vapour boundary layer thickness in two turbulent cases is due to different turbulent kinetic energy dissipation rates. Dissipation rate is independent of Reynolds number in fully turbulent channel flow. However, since lower Reynolds number flow provides thicker boundary layer around the droplet, the dissipation rate is higher in this area. Higher dissipation rate causes more turbulent kinetic energy to be transferred into internal energy which in turn brings higher heat transfer, more evaporation and consequently thicker vapour layer around the droplet.

- Evaporation of a free falling droplet in turbulent flow is a strong function of dissipation rate rather than mean flow Reynolds number.

- Turbulence has significant effect on evaporation of a droplet in a channel. However, higher evaporation rate may be achieved with low turbulent Reynolds number. This means that less energy is required to optimise the spray evaporation and operation.

7.2 Recommendations For Future Work

7.2.1 Experimental Work

The experimental work performed in this research can only capture the image of the droplet in two dimensions. Due to the nature of the turbulent flow the droplet undergoes rotation and deformation that must be captured with two high-speed cameras to measure the third dimension as well.

7.2.2 Numerical Work

The developed code in this investigation is a platform for future studies to investigate turbulence effects on the evaporation by considering more turbulent cases with different turbulence intensities. The fluid properties were assumed to be constant during the evaporation in the current research. This is not likely to be accurate for droplets involving high temperature gradients. Hence, variable property investigations could be explored for future work.

Chapter 8

REFERENCES

[1] Z. Feng and E. E. Michaelides. Drag coefficients of viscous spheres at intermediate and high Reynolds numbers. *ASME. J. Fluids Eng.*, 123(4):841–849, 2001.

[2] W. A. Sirignano. Fluid dynamics of sprays. *ASME. J. Fluids Engineering*, 115(3):345–378, 1993.

[3] O. A. Kabov, D. Zaitsev, D. P. Kirichenko, and V. S. Ajaev. Interaction of levitating microdroplets with moist air flow in the contact line region. *Nanoscale and Microscale Thermophysical Engineering*, 21(2):60–69, 2017.

[4] N. Ashgriz, editor. *Handbook of atomization and sprays: Theory and Applications*. Springer, New York Dordrecht Heidelberg London, 2011. ISBN 978-1-4419-7263-7.

[5] D. R. Guildenbecher. *Secondary atomization of electrostatistically charged drops*. PhD thesis, Purdue University, 2009.

[6] P. Sierra Sánchez. *Modeling the dispersion and evaporation of sprays in aeronautical combustion chambers*. PhD thesis, Institut National Polytechnique de Toulouse, 2012.

[7] B. Abramzon and W.A. Sirignano. Droplet vaporization model for spray combustion calculations. *International Journal of Heat and Mass Transfer*, 32:1605–1618, 1989.

[8] J. C. Maxwell. Theory of the Wet Bulb Thermometer. *Encyclopedia Britannica*, 2:625, 1890.

[9] N. Frössling. Uber die Verdunstung fallender Tropfen. *Gerlands Gerlands Beitrage zur Geophysik*, 52:170–175, 1938.

[10] G.A.E. Godsave. Studies of the combustion of drops in a fuel spray—the burning of single drops of fuel. *Symposium (International) on Combustion*, 4(1):818–830, 1953. ISSN 0082-0784.

[11] S. Sazhin. Heating and evaporation of monocomponent droplets. In *Droplets and Sprays*. Springer, London, 2014. ISBN 978-1-4471-6385-5.

[12] N. A. Fuchs and J. N. Pratt. *Evaporation and Droplet Growth in Gaseous Media*. Pergamon Press, London, 1959.

[13] G. F. Yao, S. I. Abdel-Khalik, and S. M. Ghiaasiaan. An investigation of simple evaporation models used in spray simulations. *ASME Journal of Heat Transfer*, 125:179–182, 2003.

[14] Ch. Yin. Modelling of heating and evaporation of n-Heptane droplets: Towards a generic model for fuel droplet/particle conversion. *Fuel*, 141:64–73, 2015. ISSN 0016-2361.

[15] A. P. Kryukov, V. Yu. Levashov, and S. S. Sazhin. Evaporation of diesel fuel droplets: kinetic versus hydrodynamic models. *International Journal of Heat and Mass Transfer*, 47:2541–2549, 2004.

[16] K. Aoki, C. Bardos, and S. Takata. Knudsen layer for gas mixtures. *Journal of Statistical Physics*, 112:629–655, 2003.

[17] S. Takata and K. Aoki. Two-surface problems of a multi-component mixture of vapors and noncondensable gases in the continuum limit in the light of kinetic theory. *Physics of Fluids*, 11(2743-2756), 1999.

[18] V.S. Zubkov, G.E. Cossali, S. Tonini, O. Rybdylova, C. Crua, M. Heikal, and S.S. Sazhin. Mathematical modelling of heating and evaporation of a spheroidal droplet. *International Journal of Heat and Mass Transfer*, 108: 2181–2190, may 2017. ISSN 0017-9310.

[19] N.T. Hsu and B.H. Sage. Thermal and material transfer in turbulent gas streams: Local transport from spheres. *AIChE Journal*, 3(3):405–410, 1957.

[20] R. A. S. Brown and B. H. Sage. Material Transfer in Turbulent Gas Streams: Effect of Turbulence on Local Transport from Spheres. *Journal of Chemical & Engineering Data*, 6(3):355–359, 1961.

[21] T.R. Galloway and B.H. Sage. Local and macroscopic thermal transport from a sphere in a turbulent air stream. *AIChE Journal*, 18(2):287–293, 1972.

[22] W.J. Lavender and D.C.T. Pei. The effect of fluid turbulence on the rate of heat transfer from spheres. *International Journal of Heat and Mass Transfer*, 10(4):529–539, 1967.

[23] K. Torii, M. Isobe, T. Horikosi, and N. Miura. Free-stream turbulence effects on heat and mass transfer from spheres: 2nd report, local transfer coefficients. *Bulletin of the JSME*, 24(187):138–146, 1981.

[24] M. Birouk and S. Toth. Evaporation of n-heptane Droplet in a Turbulent Atmosphere at Elevated Pressure and Temperature Conditions –An Experimental Study. In *24th ICDERS*, Taipei, 2013.

[25] W. E. Ranz and W. R. Marshal. Evaporation from drops part ii. *Chemical Engineering progress*, 48:173–180, 1952.

[26] T. Yuge. Experiments on heat transfer of spheres; influence of free stream turbulence at higher Reynolds numbers. *Rep Inst High Speed Mech Japan*, 11(209), 1959.

[27] J. G. Sandoval-Robles, H. Delmas, and J. P. Couderc. Influence of turbulence on mass transfer between a liquid and a solid sphere. *Journal of AIChE*, 27: 819–823, 1981.

[28] M. Birouk and I. Gökalp. Current status of droplet evaporation in turbulent flows. *Progress in Energy and Combustion Science*, 32(4):408–423, 2006. ISSN 03601285.

[29] M. Masoudi and W.A. Sirignano. Collision of a vortex with a vaporizing droplet. *International Journal of Multiphase Flow*, 26(12):1925–1949, 2000.

[30] I. Gökalp, C. Chauveau, O. Simon, and X. Chesneau. Mass transfer from liquid fuel droplets in turbulent flow. *Combustion and flame*, 89:286–298, 1992.

[31] N. Hiromitsu and O. Kawaguchi. Influence of flow turbulence on the evaporation rate of a suspended droplet in a hot air flow. *Heat Transfer—Japanese Research*, 24(8):689–700, 1995.

[32] J.-S. Wu, Y.-J. Liu, and H.-J. Sheen. Effects of ambient turbulence and fuel properties on the evaporation rate of single droplets. *International Journal of Heat and Mass Transfer*, 44(24):4593–4603, 2001.

[33] J.-S. Wu, K.-H. Hsu, P.-M. Kuo, and H.-J. Sheen. Evaporation model of a single hydrocarbon fuel droplet due to ambient turbulence at intermediate Reynolds numbers. *International Journal of Heat and Mass Transfer*, 46 (24):4741–4745, 2003.

[34] Y. Ohta, K. Shimoyama, and S. Ohigashi. Vaporization and combustion of single liquid fuel droplets in turbulent environment. *Bull JSME*, 18:47–56, 1975.

[35] M. Birouk. *Isotropic turbulence effect on the vaporization and combustion of hydrocarbon droplets*. PhD thesis, The University of Orleans, 1996.

[36] M. Birouk, C. Chauveau, B. Sarh, A. Quilgars, and I. Gökalp. Turbulence effects on the vaporization of mono-component single droplets. *Combust Sci Technol*, 113-114:413–28, 1996.

[37] M. Birouk and I. Gökalp. A new correlation for turbulent mass transfer from liquid droplets. *International Journal of Heat and Mass Transfer*, 45(1):37–45, 2001.

[38] S. Whitaker. *Fundamental principles of heat transfer*. Pergamon Press, New York, 1977.

[39] Y. Wang and C. J. Rutland. Direct numerical simulation of turbulent flow with evaporating droplets at high temperature. *Journal of Heat and Mass Transfer*, 42(12), 2006.

[40] P. Schroll, A.P. Wandel, E. Cant, and E. Mastorakos. Direct numerical simulations of autoignitionin turbulent two-phase flows. In *Proceedings of the Combustion Institute 32*, 2009.

[41] M.R.G. Zoby, S. Navarro-Martinez, A. Kronenburg, and A.J. Marquis. Evaporation rates of droplet arrays in turbulent reacting flows. *Proceedings of the Combustion Institute*, 33(2):2117–2125, 2011. ISSN 1540-7489.

[42] M. Birouk and S. C. Fabbro. Droplet evaporation in a turbulent atmosphere at elevated pressure – Experimental data. *Proceedings of the Combustion Institute*, 34(1):1577–1584, 2013. ISSN 1540-7489.

[43] J. Shinjo, J. Xia, and A. Umemura. Droplet/ligament modulation of local small-scale turbulence and scalar mixing in a dense fuel spray. *Proceedings of the Combustion Institute*, 35(2):1595–1602, 2015. ISSN 15407489.

[44] L. Méès, Th. Tronchin, N. Grosjean, J.-l. Marié, and C. Fournier. Evaporating droplets tracking by holographic high speed video in turbulent flow. 2016.

[45] C. Verwey and M. Birouk. Experimental investigation of the effect of droplet size on the vaporization process in ambient turbulence. *Combustion and Flame*, 182:288–297, 2017. ISSN 15562921.

[46] F. Marti, O. Martinez, D. Mazo, J. Garman, and D. Dunn-Rankin. Evaporation of a droplet larger than the Kolmogorov length scale immersed in a relative mean flow. *International Journal of Multiphase Flow*, 88:63–68, 2017. ISSN 03019322.

[47] C. Verwey and M. Birouk. Fuel vaporization: Effect of droplet size and turbulence at elevated temperature and pressure. *Combustion and Flame*, 189:33–45, 2018. ISSN 0010-2180.

[48] A K Flock, D R Guildenbecher, J Chen, P E Sojka, and H.-J Bauer. Experimental statistics of droplet trajectory and air flow during aerodynamic fragmentation of liquid drops. *International Journal of Multiphase Flow*, 47:37–49.

[49] C. W. Hirt and B. D. Nichols. Volume of fluid (VOF) method for the dynamics of free boundaries. *Journal of Computational Physics*, 39(1):201–225, 1981. ISSN 10902716.

[50] S. M. Damián. *An extended mixture model for the simultaneous treatment of short and long scale interfaces*. PhD thesis, Universidad Nacional Del Litoral, 2013.

[51] J. U. Brackbill, D. B. Kothe, and C. Zemach. A continuum method for modeling surface tension. *Journal of Computational Physics*, 100(2):335–354, 1992. ISSN 10902716.

[52] E. Berberovic, N. P. Van Hinsberg, S. Jakirlic, I. V. Roisman, and C. Tropea. Drop impact onto a liquid layer of finite thickness: Dynamics of the cavity evolution. *Physics review*, 79, 2009.

[53] R. I. Issa. Solution of the implicitly discretised fluid flow equations by operator-splitting. *Journal of Computational Physics*, 62(1):40–65, 1986. ISSN 10902716.

[54] F. Moukalled, L. Mangani, and M. Darwish. *The finite volume method in computational fluid dynamics - an advanced introduction with OpenFOAM*

and Matlab. Springer International Publishing Switzerland, 2016. ISBN 9783319168739.

[55] Y. Liu and O. Hinrichsen. CFD modeling of bubbling fluidized beds using OpenFOAM®: Model validation and comparison of TVD differencing schemes. *Computers & Chemical Engineering*, 69:75–88, 2014. ISSN 0098-1354.

[56] A. Harten. High resolution schemes for hyperbolic conservation laws. *Journal of Computational Physics*, 49(3):357–393, 1983.

[57] P. K. Sweby. High resolution schemes using flux limiters for hyperbolic conservation laws. *SIAM Journal on Numerical Analysis*, 21(5), 1984.

[58] B. van Leer. Towards the ultimate conservative difference scheme. II. Monotonicity and conservation combined in a second-order scheme. *Journal of Computational Physics*, 14(4):361–370, 1974.

[59] H. Jasak. *Error analysis and estimation for the finite volume method with applications to fluid flows*. PhD thesis, Imperial College of Science, Technology and Medicine, 1996.

[60] L. Mangani, M. Buchmayr, and M. Darwish. Development of a novel fully coupled solver in OpenFOAM: Steady-state incompressible turbulent flows in rotational reference frames. *Numerical Heat Transfe Part B*, 66:526–543, 2014.

[61] E. DeVilliers. The potential of large eddy simulation for the modeling of wall bounded flows. (July):1–375, 2006.

[62] S. B. Pope. *Turbulent Flows*. Cambridge University Press, Cambridge, 1st edition, 2000. ISBN 0521591252.

[63] F. Ducros, F. Nicoud, and T. Poinsot. Wall-adapting local eddy-viscosity models for simulations in complex geometries. *Numerical Methods for Fluid Dynamics VI*, 1998.

[64] J. Smagorinsky. General circulation experiments with the primitive equations: I. the basic experiment. *Monthly weather review*, 91(3):99–164, 1963.

[65] M. Germano, U. Piomelli, P. Moin, and W. H Cabot. A dynamic subgridscale eddy viscosity model. *Physics of Fluids A: Fluid Dynamics*, 3:3128, 1991.

[66] F. Ducros, P. Comte, and M. Lesieur. Large-eddy simulation of transition to turbulence in a boundary layer developing spatially over a flat plate. *Journal of Fluid Mechanics*, 326:1–36, 1996.

[67] C. Fureby, G. Tabor, H. G. Weller, and A. D. Gosman. A comparative study of subgrid scale models in homogeneous isotropic turbulence. *Physics of Fluids*, 9:1416, 1997.

[68] T. Lund, X. Wu, and K. D. Squires. Generation of turbulent inflow data for spatially-developing boundary layer simulations. *Journal of Computational Physics*, 140, 1998.

[69] P. R. Spalart. Direct numerical simulation of a turbulent boundary layer up To Reθ= 1410. *Journal of Fluid Mechanics*, 187:61–98, 1988.

[70] S. S. Deshpande, L. Anumolu, and M. F. Trujillo. Evaluating the performance of the two-phase flow solver interFoam. *Computational Science and Discovery*, 5(1), 2012. ISSN 17494680.

[71] C. Galusinski and P. Vigneaux. On stability condition for bifluid flows with surface tension: Application to microfluidics. *Journal of Computational Physics*, 227(12):6140–6164, 2008. ISSN 0021-9991.

[72] C. Ma and D. Bothe. Numerical modeling of thermocapillary two-phase flows with evaporation using a two-scalar approach for heat transfer. *Journal of Computational Physics*, 233:552–573, 2013. ISSN 0021-9991.

[73] J. Schlottke and B. Weigand. Direct numerical simulation of evaporating droplets. *Journal of Computational Physics*, 227(10):5215–5237, 2008. ISSN 00219991.

[74] B. Sobac, P. Talbot, B. Haut, A. Rednikov, and P. Colinet. A comprehensive analysis of the evaporation of a liquid spherical drop. *Journal of Colloid and Interface Science*, 438:306–317, 2015. ISSN 0021-9797.

[75] W. M. Kays and M. E. Crawford. *Convective heat and mass transfer*. 1980. ISBN 9788578110796.

[76] G. Nikuradse. Laws of turbulent flow in smooth pipes. *Journal of the Royal Aeronautical Society*, 36(264):1050–1051, dec 1932. ISSN 0368-3931.

[77] R. D. Blevins. *Applied fluid dynamics handbook*. Van Nostrand Reinhold, New York, 1984.

[78] Watson. https://watsonbiolab.com/.

[79] Y. Nakayama and R. F Boucher. *Introduction to Fluid Mechanics*. Butterworth-Heinemann, 1999. ISBN 9780080291420.

[80] S.J. Kline and F.A Mcclintock. Describing uncertainties in single-sample experiments. *Mechanical Engineering*, 75:3–8, 1953.

[81] A. Daïf, M. Bouaziz, X. Chesneau, and A. Ali Chérif. Comparison of multi-component fuel droplet vaporization experiments in forced convection with the Sirignano model. *Experimental Thermal and Fluid Science*, 18(4):282–290, 1998. ISSN 08941777.

[82] R. D. Moser, J. Kim, and N. N. Mansour. Direct numerical simulation of turbulent channel flow up to Reτ=590. *Physics of Fluids*, 11(4):943–945, 1999. ISSN 10706631.

[83] P.R Yearling. *Experimental determination of convective heat and mass transfer rates from single evaporating droplets in a turbulent air flow*. PhD thesis, North Carolina State Universi, 1995.

[84] J. Kim and P. Moin. Transport of passive scalars in turbulent channel flow. In *The Sixth International Symposium on Turbulent Shear Flows*, page 14, Toulouse, France, 1987.

[85] J. Jiménez, P. Moin, R. Moser, and L. Keefe. Ejection mechanisms in the sublayer of a turbulent channel. *Physics of Fluids*, 31(6):1311–1313, 1988. ISSN 00319171.

[86] T. Sakai and M. Saito. Single-droplet combustion of coal slurry fuels. *Combustion and Flame*, 51(C):141–154, 1983. ISSN 00102180.

[87] R.J. Adrian, K.T. Christensen, and Z.C Liu. Analysis and interpretation of instantaneous turbulent velocity fields. *Experiments in Fluids 2*, 29:275–290, 2000.

[88] S. Kida and H. Miura. Identification and analysis of vertical structures. *European Journal of Mechanics-B/Fluids*, 17:471–488, 1998.

[89] Václav Kolář. Vortex identification: New requirements and limitations. *International Journal of Heat and Fluid Flow*, 28(4):638–652, 2007. ISSN 0142-727X.

[90] R.A. Antonia, M. Teitel, J. Kim, and W.B. Browne. Low-Reynolds-number effects in a fully developed turbulent channel flow. *Journal of Fluid Mechanics*, 236:579–605, 1992.

[91] J. Happer and D. W. Moore. The motion of a spherical liquid drop at high Reynolds number. *Journal of Fluid Mechanics*, 32(part 2):367–391, 1968.

Appendix

Drawings

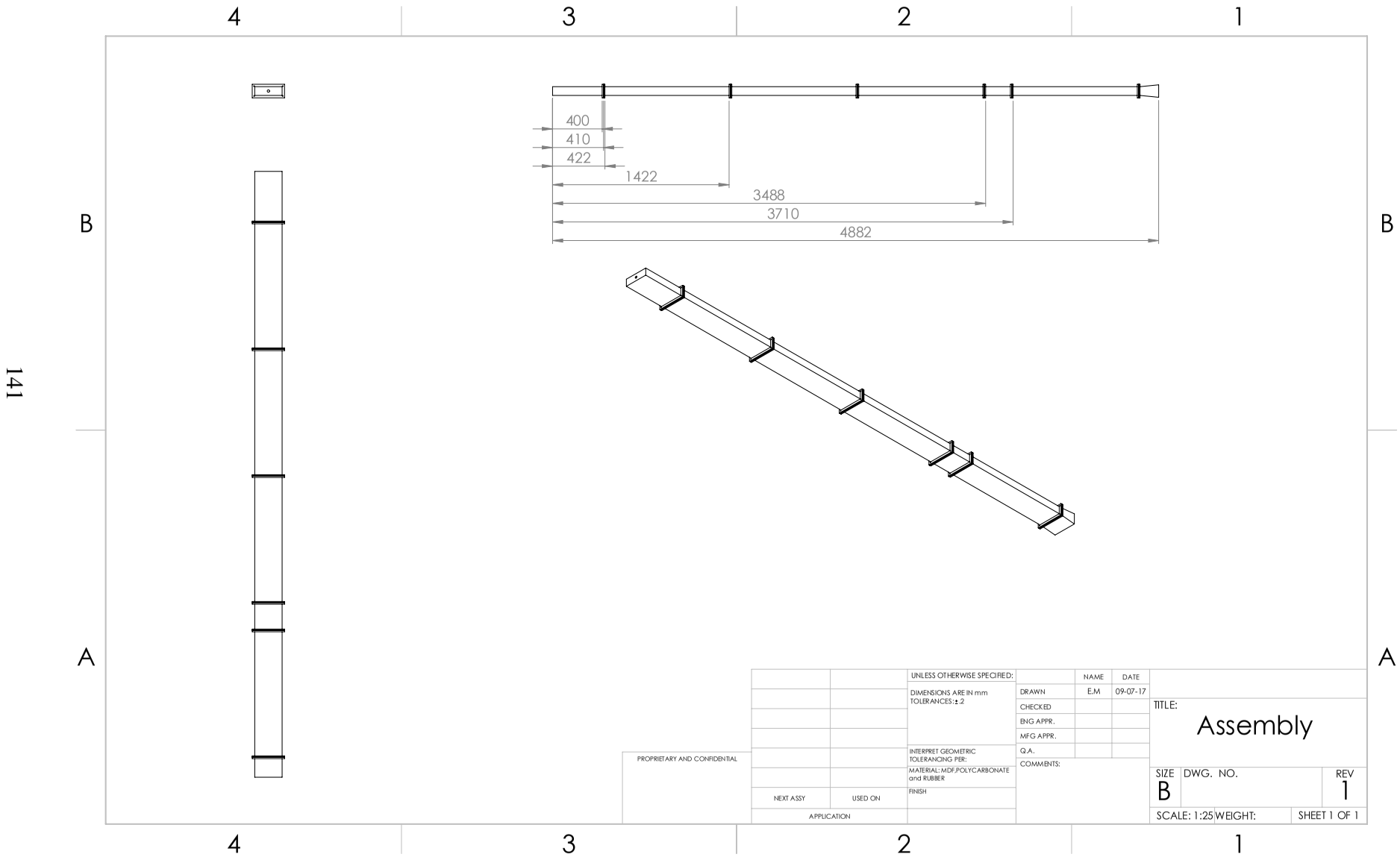

141

Figure 1: Air channel assembly

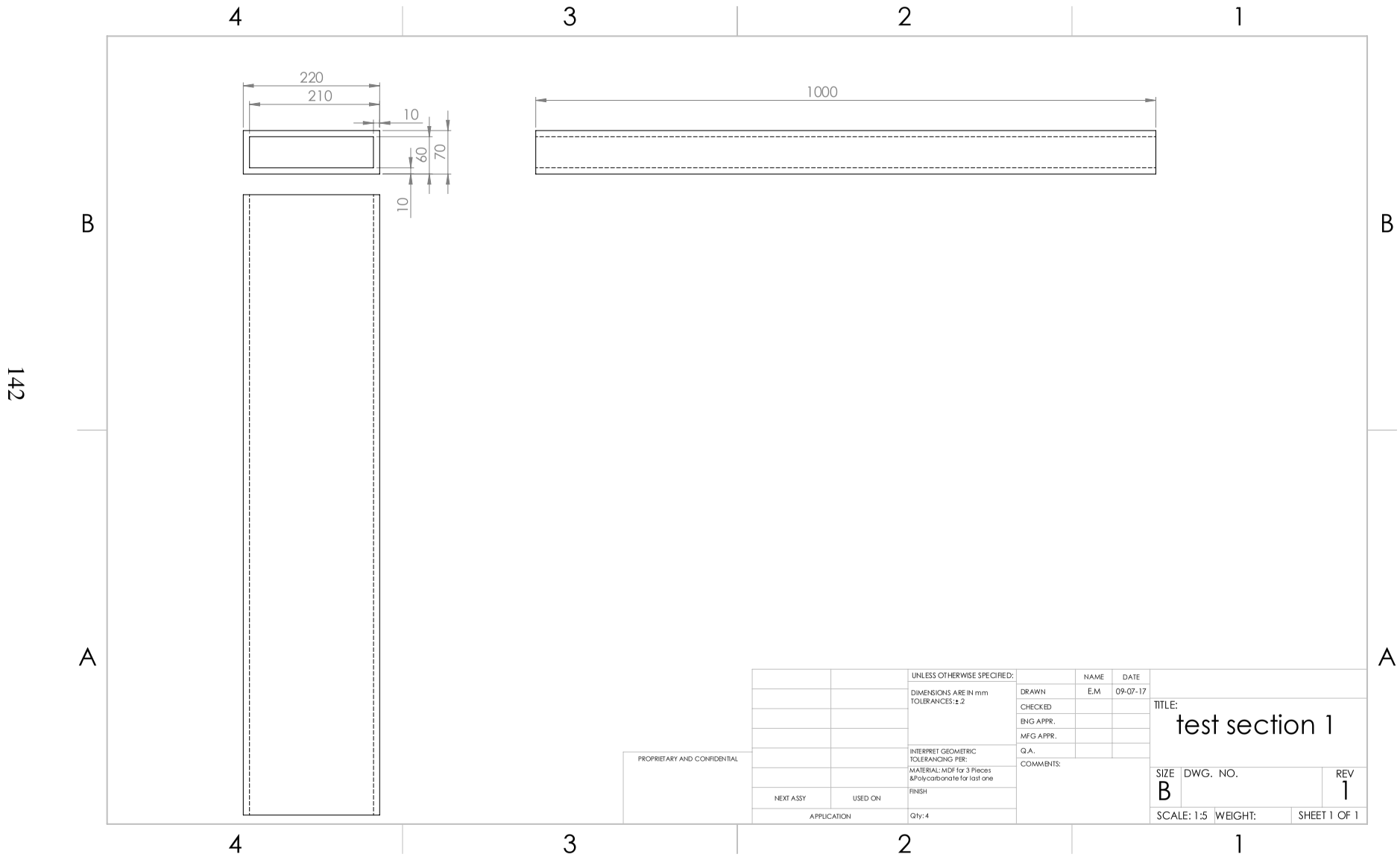

142

Figure 2: Air channel test sections

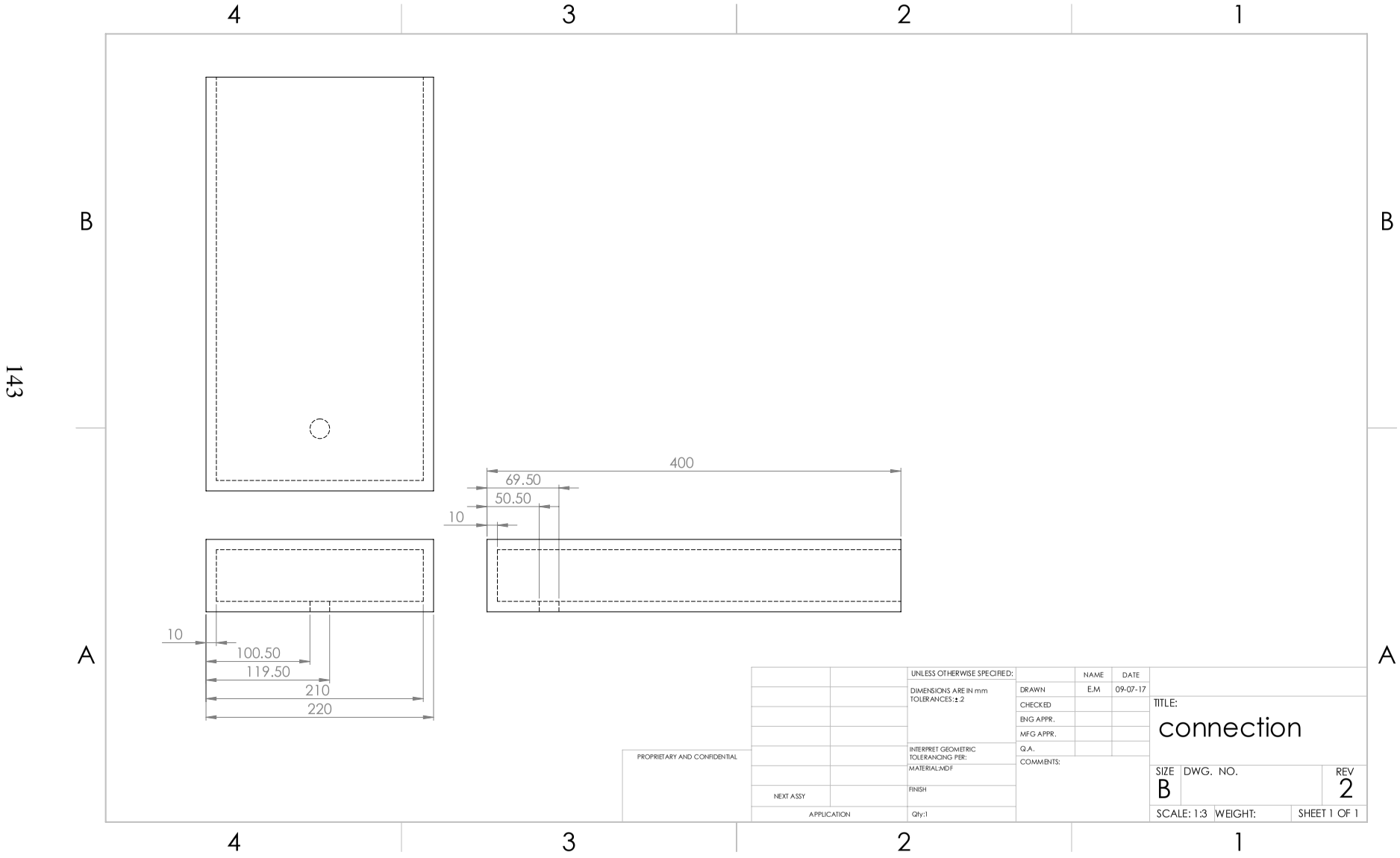

Figure 3: Air channel inlet part

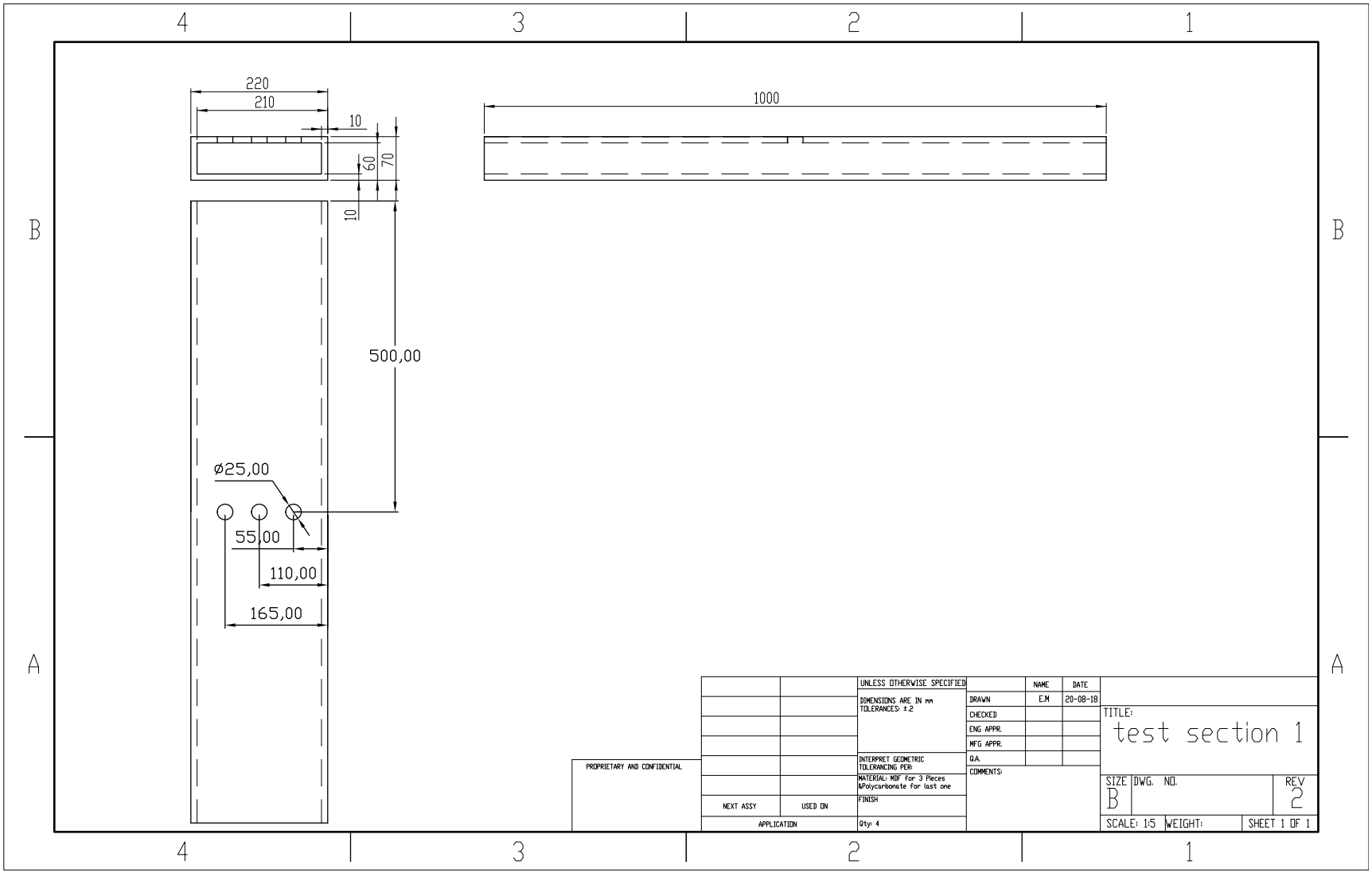

Figure 4: Air channel gauge section

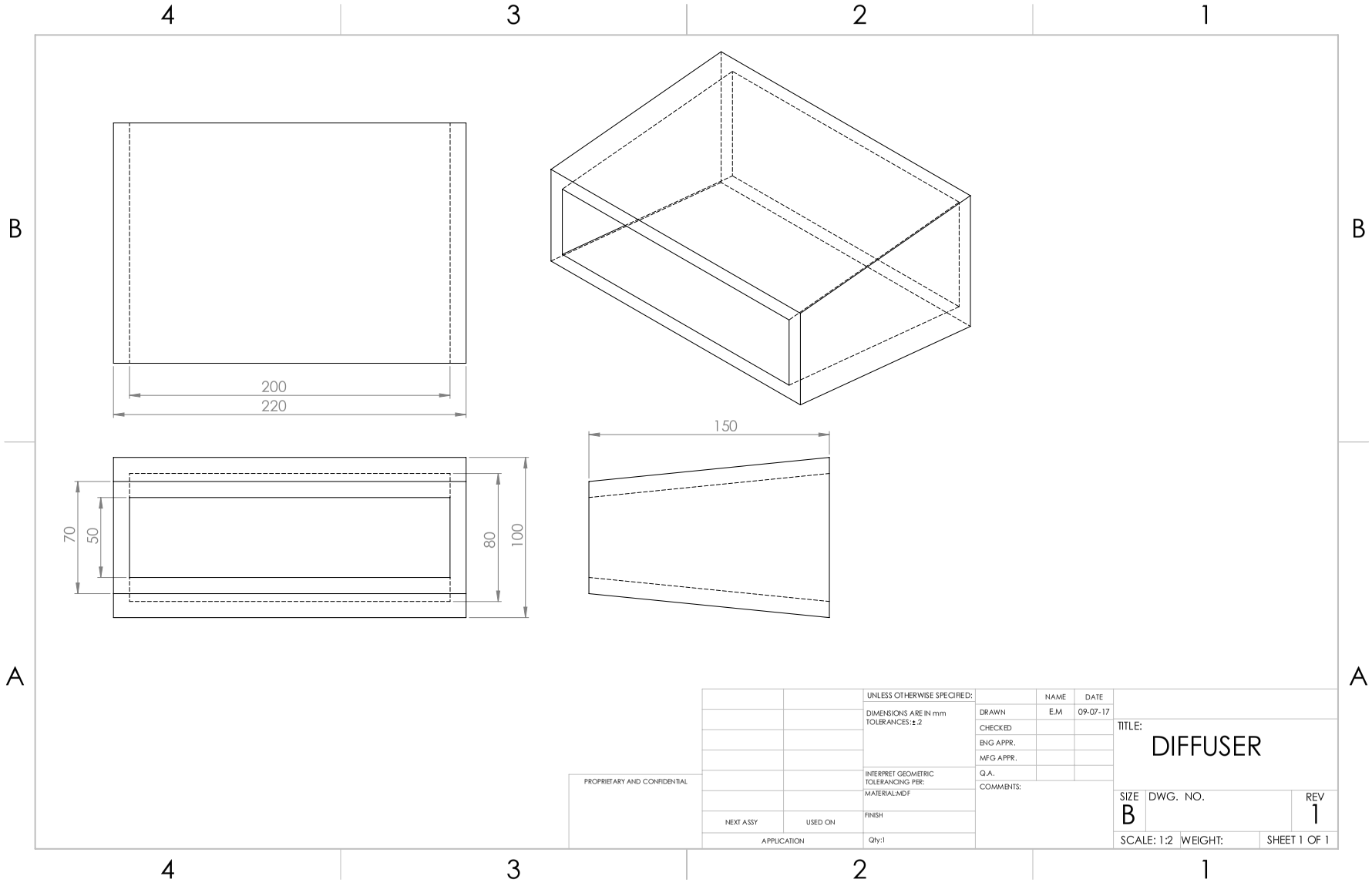

Figure 5: Air channel diffuser

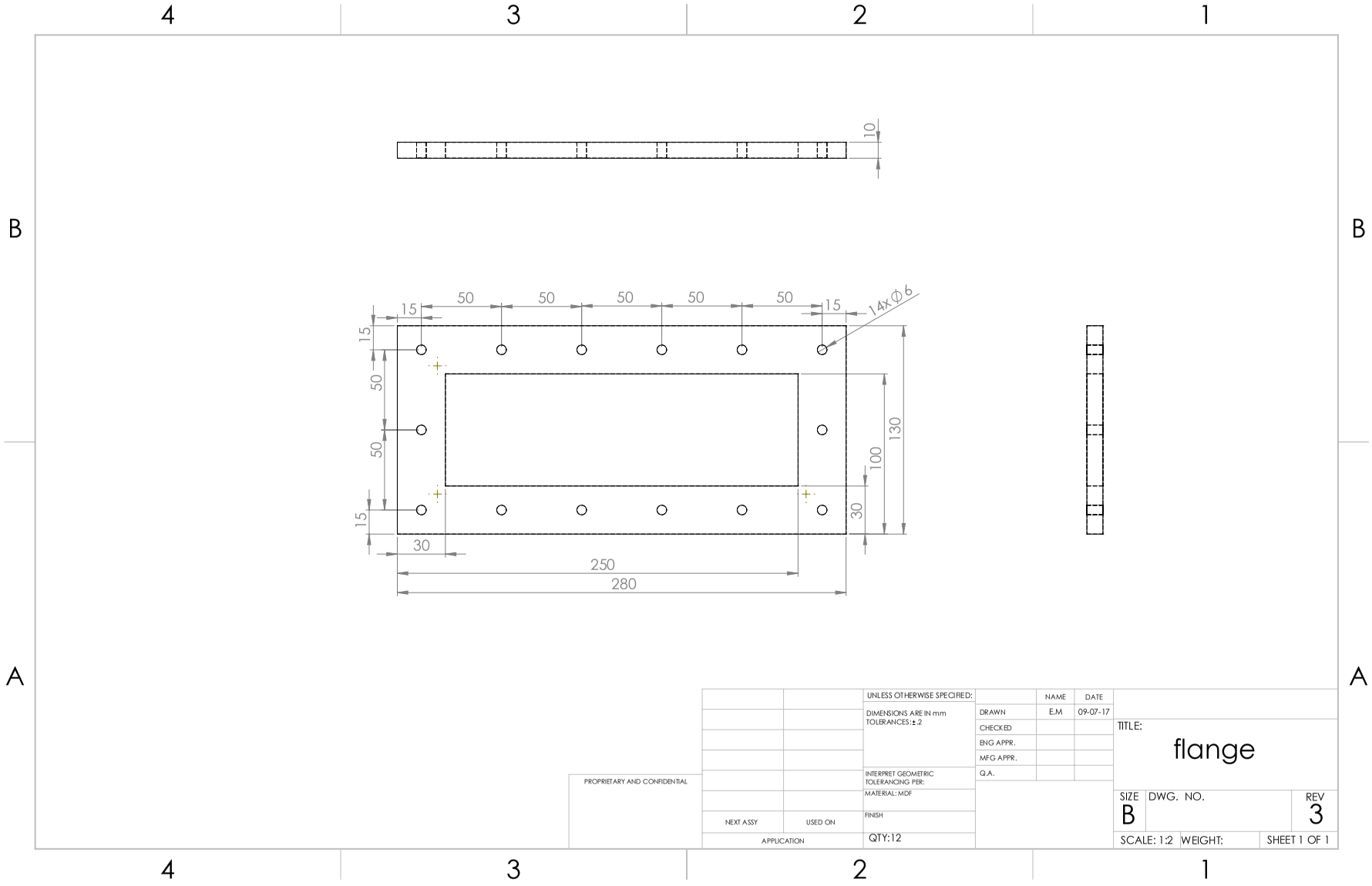

Figure 6: Air channel flange

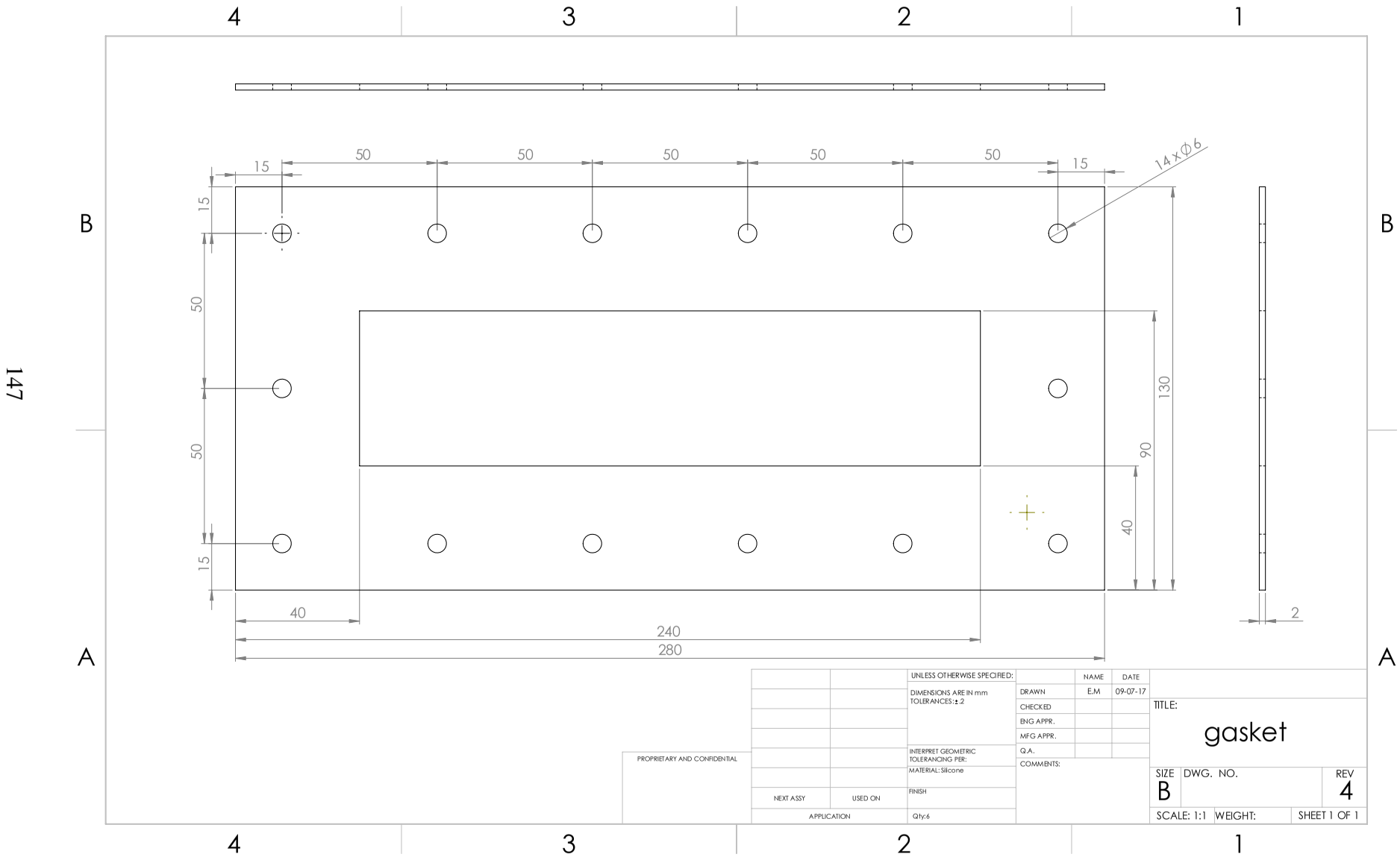

Figure 7: Air channel gasket

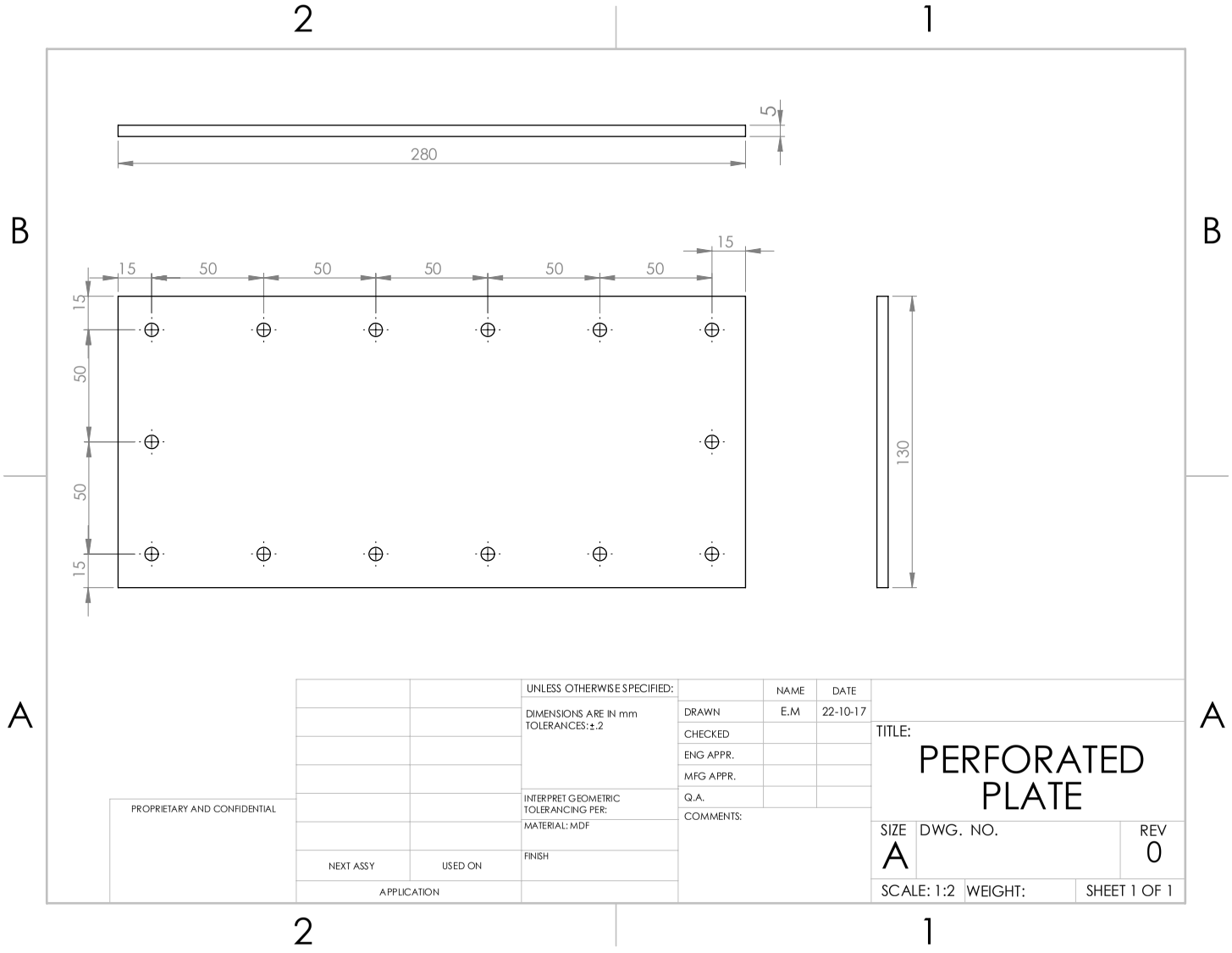

Figure 8: Air channel straightener

Authorship

Paper "A Study on the Flow Field and Internal Circulation of a Single Moving Droplet", 20th Australasian Fluid Mechanics Conference, Perth, Australia, 5-8 December 2016.
Authors and full affiliations:

	Conception and design	**Acquisition of data and method**	**Data conditioning and manipulation**	**Analysis and statistical method**	**Interpretation and discussion**	**Final approval**
Dr. Andrew King	×	×	×	×		
I acknowledge that these represent my contribution to the above research output. Signed:						
Dr. Ramesh Narayanaswamy	×				×	×
I acknowledge that these represent my contribution to the above research output. Signed:						

Paper "A Study of the Phase Change in Three Phase Environment", 21st Australasian Fluid Mechanics Conference, Adelaide, Australia, 10-13 December 2018.
Authors and full affiliations:

	Conception and design	**Acquisition of data and method**	**Data conditioning and manipulation**	**Analysis and statistical method**	**Interpretation and discussion**	**Final approval**
Dr. Ramesh Narayanaswamy	×			×		
I acknowledge that these represent my contribution to the above research output. Signed:						
Dr. Andrew King	×	×			×	
I acknowledge that these represent my contribution to the above research output. Signed:						

Figure 9: Authorship contribution